Università degli Studi di Ferrara

DOCTORAL COURSE IN

"Scienze dell'Ingegneria"

Cycle XXXIV

COORDINATOR: Prof. Stefano Trillo

Location Awareness in 5G and B5G Ecosystems: Characterization, Design, and Experimentation

Scientific/Disciplinary Sector ING-INF/03

Candidate	**Supervisor**
Dott. Flavio Morselli	Prof. Andrea Conti
(Signature)	*(Signature)*

Years 2018/2022

Sommario

La conoscenza della posizione (location awareness) di dispositivi, persone, oggetti e veicoli è un elemento fondamentale per una moltitudine di servizi e casi d'uso nelle reti di quinta generazione, 5th generation (5G), e future -beyond 5G (B5G)- inclusi quelli relativi all'automazione, alla logistica, agli ambienti intelligenti, e all'Industria 4.0. I requisiti relativi alle prestazioni necessarie per abilitare tali casi d'uso, sono però difficili da soddisfare. Si rende quindi necessaria la progettazione di nuovi algoritmi di localizzazione, basati su tecniche di machine learning, in grado di imparare dall'ambiente e di sfruttare appieno le informazioni fornite dalla rete. In aggiunta, l'integrazione di sistemi radar, in particolare le reti di sensori radar, con le reti cellulari di prossima generazione è un elemento fondamentale per espandere ancora di più i servizi abilitati e contemporaneamente migliorare la qualità della comunicazione e l'efficienza nella gestione delle risorse. A tal fine è necessario derivare modelli accurati dei disturbi introdotti dal canale wireless e progettare nuovi algoritmi in grado di fornire informazioni di contesto, come ad esempio, il numero di persone in una determinata area. Gli obiettivi principali di questa tesi sono:

(i) la progettazione di algoritmi basati su machine learning per la localizzazione in reti 5G e B5G; e

(ii) la caratterizzazione dei disturbi nelle reti wireless di sensori radar e la progettazione di algoritmi per fornire informazioni di contesto.

In particolare, questa dissertazione presenta la progettazione di un algoritmo basato sul concetto di soft information (SI) in grado di sfruttare sia misure fornite dalla rete 5G, sia di fondere tali misure con osservazioni ottenute tramite altre tecnologie. Le prestazioni fornite da tale soluzione sono confrontate con quelle ottenute tramite l'utilizzo di metodi classici in scenari standardizzati dal 3rd Generation Partnership Project (3GPP), basandosi su simulazioni rigorose a livello di campione dei segnali mediante un simulatore 3GPP realizzato anch'esso durante l'attività di dottorato e nell'ambito di un progetto europeo H2020. I risultati mostrano un guadagno di prestazioni significativo dell'approccio proposto rispetto alle prestazioni riportate nei report tecnici del 3GPP. Per quanto concerne

le reti di sensori radar invece, la dissertazione dapprima presenta l'attività sulla caratterizzazione statistica del clutter basata su dati sperimentali. Tali dati sono ottenuti mediante una campagna sperimentale con una rete di sensori radar a banda ultralarga in un ambiente indoor. Infine, la dissertazione presenta l'attività di sviluppo di un algoritmo di conteggio di tipo crowd-centric basato su tecniche di machine learning. Le prestazioni di tale algoritmo sono poi confrontate con quelle di metodi state-of-the-art basandosi su misure sperimentali.

Abstract

Location awareness is a key enabler for a variety of verticals and use cases (UCs) in 5th generation (5G) and beyond 5G (B5G) networks, including those related to autonomy, logistic, smart environments, and Industry 4.0. However, fulfilling the key performance indicator (KPI) requirements for such UCs is challenging. This calls for new localization algorithms able to learn from the environment and to fully leverage the positional information provided by the network measurements. Moreover, the integration of next generation cellular networks with sensor radar networks (SRNs), will be fundamental to further enhance these new verticals, as well as to improve the communication performance and the network resource management. This calls for an accurate modeling of the wireless impairments and the design of algorithms able to provide physical analytics (e.g., number of person in a monitored area) in addition to location information. The main objectives of this thesis are:

1. design of machine learning based algorithms for localization in 5G and B5G networks; and

2. characterization of wireless impairments in SRNs, as well as the design of algorithms for extracting physical analytics via SRNs.

In particular, this thesis presents the design of soft information (SI)-based localization algorithms exploiting both radio access technology (RAT)-dependent (obtained from the 5G network) and RAT-independent (obtained via non-3rd Generation Partnership Project (3GPP) technologies) measurements. Performance using both SI and classical approaches are quantified in 3GPP standardized scenarios via rigorous simulations in full conformity with 3GPP technical specifications and reports. Results show that the proposed SI approach significantly outperforms the approaches reported in 3GPP technical reports. In addition, a statistical characterization of the clutter for SRNs employing ultra-wideband (UWB) signals is provided based on experimental measurements carried out in an indoor environment. Lastly, a crowd-centric counting algorithm based on machine learning techniques is proposed and compared with state-of-the-art approaches based on experimental measurements.

Contents

Abbreviations

3GPP 3rd Generation Partnership Project

5G 5th generation

ADT Anderson–Darling test

AE angle estimation

AP access point

AOA angle-of-arrival

AOD angle-of-departure

AWGN additive white Gaussian noise

B5G beyond 5G

BC binary clustering

CA-CFAR cell-average costant false alarm rate

CDF comulative density function

CEO counting error outage

CP cyclic prefix

DE distance estimate

DL-TDOA downlink time-difference-of-arrival

EAF exponential averaging filter

ECDF empirical comulative density function

EFIM equivalent Fisher information matrix

EM expectation-maximization

ER empty room

ERP effective radiated power

FR1 frequency range 1

FW Fisher–Wald

GM Gaussian mixture

GMM Gaussian mixture model

gNB next generation NodeBs

GNSS global navigation satellite systems

IFFT inverse fast Fourier transform

IID independent, identically distributed

IMU inertial measurement unit

IOO indoor open office

IoT Internet-of-Things

IS intelligent surface

KDE kernel density estimation

KPI key performance indicator

LBS location-based service

LBT Ljung–Box test

LOS line-of-sight

LS least squares

LTE long-term evolution

MAP maximum *a posteriori*

MIMO multiple-input multiple-output

ML maximum likelihood

MMSE minimum-mean-square-error

NLOS non line-of-sight

OFDM orthogonal frequency division multiplexing

PCA principal component analysis

PCI physical cell identity

PDF probability density function

POC path-overlap coefficient

PRS positioning reference signal

PSL positioning service level

PSK phase-shift keying

QPSK quadrature phase-shift keying

RAT radio access technology

RB resource block

RE resource element

RMSE root-mean-square error

RS reference signal

RSSI received signal strength indicator

RSTD relative signal time difference

RTT round trip time

RV random variable

SAI soft angle information

SC subcarrier

SCI soft context information

SDC single-delay canceller

SFI soft feature information

SI soft information

SNR signal-to-noise ratio

SR sensor radar

SRI soft range information

SRN sensor radar network

SVE single-value estimate

TDOA time-difference-of-arrival

TOA time-of-arrival

TOF time-of-flight

TR technical report

UC use case

UE user equipment

UMi urban microcell

UML unsupervised machine learning

UWB ultra-wideband

WT window treshold

Chapter 1

Introduction

Location awareness is a key enabler for 5th generation (5G) networks and is expected to be even more fundamental in future beyond 5G (B5G) networks [1–7]. The availability of nodes positional information enables a variety of novel use cases (UCs), including those related to autonomous vehicles [8–12], smart environments [13–17], and Internet-of-Things (IoT) [18–22]. Moreover, accurate location information can also be leveraged for smart resource management and interference coordination/engineering in wireless networks [23–29]. In particular, has recognized the importance of localization in the 5G standardization process [30–32]. Different key performance indicators (KPIs) requirements in terms of horizontal accuracy, vertical accuracy, latency, and availability have been identified and grouped into seven positioning service levels (PSLs) [32]. However, providing the localization accuracy required by such UCs is challenging, especially in harsh wireless propagation environments [33–38].

In order to improve the localization accuracy, 5G and B5G networks will leverage an ecosystem of different technologies able to provide heterogeneous measurements [39–42]. Current 5G networks support heterogeneous localization in order to take full advantage of the numerous sensors which are typically available in commercial devices (e.g., Wi-Fi, ultra-wideband (UWB), Bluetooth, global navigation satellite systems (GNSS), and inertial measurements units) [30, 31, 43, 44]. However, data fusion techniques typically require the knowledge of models to account for the relationship among the different types of observations [45–48]. These models may be difficult to obtain in complex environments and may lead to performance degradation if the environments are highly dynamic.

In order to enable these novel UCs it is necessary to design new localization algorithms which are able to: (i) fully exploit the location information inherent in these network measurements (power, time, and angle measurements) together with contextual data (digital maps, mobility models, and user profiles); (ii) cope with the impairments

introduced by the wireless environment; and (iii) enable efficient and seamless fusion of measurements gathered from different technologies. In this context, algorithms based on machine learning techniques, are prime candidate for providing accurate localization and are currently subject of research and standardization work [5, 49–53]. In particular, soft information (SI)-based localization is particularly suited for providing location-awareness in 5G and B5G networks [5, 42, 54, 55]. SI-based localization relies on statistical models learned from the environment to provide robust localization in challenging wireless environments and seamless fusion of different type of measurements.

The synergy between localization and communication is expected to play a central role in B5G networks, where the integrated sensing and communication paradigm is driving a fervent research world-wide and pre-standardization works [56–64]. In this context, sensor radar networks (SRNs), which provide location and context information relative to people and objects not equipped with a dedicate device, are fundamental [65–71]. Contrary to the active case, where the agents in unknown position actively participate in the localization process, SRNs rely on the backscattered signals reflected by the targets and the environment [65, 72–78]. The integration of SRNs with 5G and B5G networks is expected to further improve and enable new UCs envisioned by next generation of wireless networks [79–83]. However, accurate localization via SRN is particularly challenging in indoor environments characterized by multipath propagation, clutter, and signal obstructions (e.g., due to the presence of furniture and walls) [84–87]. Typically, measurements are usually heavily affected by such impairments, severely affecting detection reliability and localization accuracy [35, 37, 88]. Thanks to its fine delay resolution and the capability of resolving multipaths, UWB technology is particularly suited for tracking non-collaborative objects in indoor environments [89–98]. Furthermore, UWB has seen a renewed interest in recent years, with latest flagship devices from multiple manufacturers integrating UWB sensors to support short range communications and context-awareness applications. However, characterization of the wireless impairments, especially the clutter, is necessary to design and operate such networks [73, 74, 99–103]. In addition, the design of algorithms for providing physical analytics, e.g., number of non-collaborative target objects in a monitored area, is fundamental for supporting new applications related to crowd sensing and behavior analysis applications in future wireless networks [104–110].

Objectives and Dissemination

The main goals of this thesis are the design of machine learning based algorithms for active localization, the characterization of wireless impairments, and the design of algorithms for extracting physical analytics in 5G and B5G ecosystem. The key contributions of the

thesis can be summarized as follows:

- development of SI-based localization algorithms for 5G and B5G networks, which can be easily integrated with already standardized architecture and procedures;

- development of a 5G localization simulator capable of simulating 5G reference signal and measurements procedures in full conformity with 3rd Generation Partnership Project (3GPP) technical reports and specifications;

- quantification of the performance gains provided by SI-based approach in 3GPP standardized scenarios, leveraging both 5G specific measurements and non-3GPP technologies;

- statistical characterization based on experimental measurements of the clutter impairment in UWB SRNs operating in indoor environments; and

- design of crowd-centric counting algorithms based on machine learning techniques for UWB SRNs.

The remainder of the thesis is organized as in the following.

Chapter 2 provides a general description of active and passive localization networks. Classical measurements, localization, and tracking algorithms are discussed and serves for contextualize the research activity presented in this thesis.

Chapter 3 provides a review of classical single-value estimate (SVE)-based localization and SI-based localization. In particular, the extraction of the SI from networks measurement is detailed and discussed.

Chapter 4 reviews the localization procedures in 5G networks. A detailed discussion of the positioning reference signal (PRS) employed to perform downlink time-difference-of-arrival (DL-TDOA) measurements is provided as an example of dedicates reference signal.. In addition, classical algorithms for localization in cellular networks are presented.

Chapter 5 introduces the concept of SI for location awareness in 5G and B5G networks. Main features of SI and how this approach can be applied in the context of 5G and B5G networks are discussed. Two case study based on rigorous simulations of the reference signals and measurements procedure standardized for 5G networks are presented in two 3GPP standardized scenarios, namely urban microcell (UMi) and indoor open office (IOO) scenarios. Performance gains provided by SI approach are evaluated considering DL-TDOA measurements alone, and the fusion of DL-TDOA measurements with time-of-flight (TOF) measurements obtained using Wi-Fi technology.

Chapter 6 first presents a system model for SRNs employing UWB signals in indoor environment. Then, it provides a statistical characterization of the static clutter for UWB

SRNs operating in indoor environments, based on experimental data. Lastly, the design of an algorithm for extracting physical analytics is presented. In particular, a crowd-centric counting algorithm based on unsupervised machine learning techniques is proposed. The performance of the proposed algorithm is compared with state-of-the-art methods using experimental data.

The results presented in this thesis have been published in the proceedings of international conferences and premier journals as indicated in the author's publication list. Furthermore, part of the research activity has been conducted within an European research project, namely LOCUS (LOCalization and analytics on-demand embedded in the 5G ecosystem, for Ubiquitous vertical applicationS) [111], and an international project, namely nCOT (non-Collaborative Object Tracking).

Notation

Random variables are displayed in sans serif, upright fonts; their realizations in serif, italic fonts. Vectors and matrices are denoted by bold lowercase and uppercase letters, respectively. For example, a random variable and its realization are denoted by x and x; a random vector and its realization are denoted by $\mathbf{x}$ and $\boldsymbol{x}$; a random matrix and its realization are denoted by $\mathbf{X}$ and $\boldsymbol{X}$, respectively. Sets and random sets are denoted by upright sans serif and calligraphic font, respectively. For example, a random set and its realization are denoted by X and $\mathcal{X}$, respectively. The function $f_{\mathsf{x}}(\boldsymbol{x})$ and, for brevity when possible, $f(\boldsymbol{x})$ denote the probability density function (PDF) of a continuous random variable (RV) $\mathbf{x}$; $f_{\mathsf{x}|\mathsf{y}}(\boldsymbol{x}|\boldsymbol{y})$ and, for brevity when possible, $f(\boldsymbol{x}|\boldsymbol{y})$ denote the PDF of $\mathbf{x}$ conditional on $\mathbf{y} = \boldsymbol{y}$; $\varphi(\boldsymbol{x}; \boldsymbol{\mu}, \boldsymbol{\Sigma})$ denotes the PDF of a Gaussian RV $\mathbf{x}$ with mean $\boldsymbol{\mu}$ and covariance matrix $\boldsymbol{\Sigma}$; operator $\mathbb{E}\{\cdot\}$ denotes the expectation of the argument. The notation $\boldsymbol{A} \succcurlyeq \boldsymbol{B}$ denotes that the matrix $\boldsymbol{A} - \boldsymbol{B}$ is positive semi-definite; for a matrix $\boldsymbol{A}$ and a vector $\boldsymbol{a}$ the transpose is denoted by $\boldsymbol{A}^{\mathrm{T}}$ and $\boldsymbol{a}^{\mathrm{T}}$, respectively; $\mathrm{tr}(\boldsymbol{A})$ denotes the trace of the matrix $\boldsymbol{A}$. Operators $(\cdot)^{*}$ and $||\cdot||_{2}$ denote the complex conjugate operator and the 2-norm operator, respectively.

Chapter 2

Preliminaries on Localization

Wireless localization networks aim to estimate nodes' position based on the sensing of the environment. A first classification to distinguish between different wireless localization networks is based on the role of the node that wish to be localized. If the node actively participate in the localization process by exchanging measurements with other network nodes, we refer to the wireless localization network as an active localization network [1]. In this case, we refer to the nodes in unknown position and the nodes in known position as agents and anchors, respectively. Classical example of active localization networks are cellular networks, where the device actively exchange measurements with the base station in order to determine its position [38]. Conversely, if the node to be localized does not actively participate to the localization process, we refer to the wireless localization network as passive localization network. In this case, the nodes composing the network infer the target position (i.e., the nodes in unknown position) based on the reflection of the electromagnetic signals in the surrounding environment. Classical example of passive localization networks are SRNs, which can leverage dedicated signals or signals already present on air for other purposes (i.e., signals of opportunity) for performing localization and tracking [65].

In active localization networks, the agents are identified by an unique identification. Thus, no ambiguities are present when assessing the source of the measurements. Moreover, agents can cooperate between them by exchanging measurements in order to further improve the localization accuracy and perform distributed inference [112]. This is particularly important in 5G and B5G networks, where the device-to-device communications are supported for IoT UCs [113]. Fig. 2.1 depicts a pictorial representation of an active localization networks composed by two agents and four anchors. In addition to the measurements performed with the anchors, agents exchange measurements to refine their position estimates. On the other hand, in SRN the target is not directly involved in the
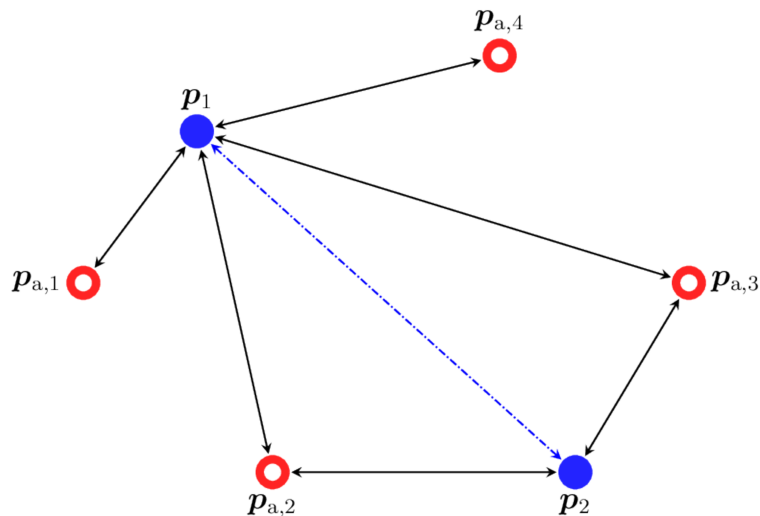
Figure 2.1: Example of active localization networks: wireless localization network with two agents and four anchors. Red empty circles represent the anchor positions and blue circles represent the agent positions. Solid black lines indicate the measurements exchange between the agents and anchors. Blue dash dotted line indicates the measurements exchange between different agents.

measurement process. In presence of multiple targets, data association techniques must be employed to cope with the uncertainties derived by the interdependence between the target locations and the measurements [70]. Fig. 2.2 depicts a passive localization networks in multistatic setting, i.e., where transmitter and receiver are not co-located. At the receiver, the received signals is given by the superposition of the components determined by reflections on the targets, as well as the background and obstacles present in the environment (i.e., clutter component) [88].

Typically, localization process in both active and passive networks can be divided in two distinct steps: i) a sensing phase where the measurements are carried out and exchanged between the network nodes and ii) a location inference phase where the nodes position is estimated based on the measurements obtained in the previous stage and prior knowledge if available. In addition, based on the same measurements used to perform location inference is it possible to extract context information not directly related to the nodes position. Physical analytics (e.g., number of targets, flow-mobility, and classifications) can be achieved exploiting such measurements [104].

2.1   Measurements for Localization

Three main types of measurement can be leveraged for the location inference phase[1]:

---

[1]Other type of measurements related to the wireless channel statistics (e.g., delay spread, channel impulse response, and excess delays) can also be employed to perform localization based on fingerprints methods.
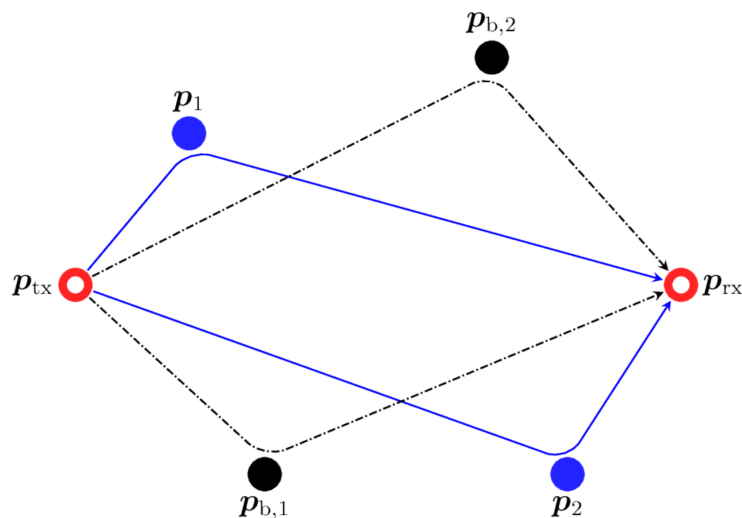
Figure 2.2: Example of passive localization networks: multistatic sensor radar network with one radar transmitter and one radar receiver. Red empty circles represent the transmitter and receiver positions, blue circles represent the target scatterers, and black circles represent the background scatterers (clutter generators). Dash dotted lines indicate component related to the background scatterers. Solid lines indicate the first path component related to the target.

1. Time-based measurements: this type of measurement are derived based on the TOF of the signals employed by the network. Time-based measurements are directly related to the distance between the networks nodes and can be used for multilateration. Typical examples of time-based measurements are time-of-arrival (TOA), time-difference-of-arrival (TDOA), and round trip time (RTT);

2. Angle-based measurements: direction of arrival or departure of the signals can be employed to infer the agent or target positions via triangulation. Typically, angle-based measurements exploit multiple antennas to modify the array radiation pattern and electronically steer the receiving or transmitting beams. Typical examples of angle-based measurements are angle-of-arrival (AOA) and angle-of-departure (AOD); and

3. Power-based measurements: similar to time-based measurements, power-based measurements are related to the distance between the network nodes. In particular, the distance between two nodes can be estimated given the transmitted power, the received power, and the attenuation loss determined by the wireless propagation. This type of measurements is usually employed in active localization networks and are based on received signal strength indicator (RSSI).

Typically, time-based measurements provide the best localization accuracy compared to the other two [114]. However, precise synchronization between network nodes, and in particular between anchors and sensor radar (SR) for active and passive localization net-

works, respectively, is required. Small time-synchronization errors may determine large error in the calculation of the distances [96]. Angle-based measurements offer a valid alternative to time-based measurements in terms of achievable localization accuracy, but suffer from several drawbacks. In particular, depending on the frequency band considered, antenna array used to estimate the AOA and AOD can be large and expensive, preventing the integration in consumer devices. Historically, angle-based measurements were used in conjunction with time-based measurements in passive localization networks. Nowadays, this trend is changing with the recent technological advances in electronic devices. This is particularly relevant in 5G and B5G networks, where xxthe use of millimeter wave spectrum allows the integration of antenna arrays composed by many radiation elements even in small devices.

All three types of measurements inherently carry positional information regarding the nodes relative position. Despite being used in both active and passive cases, different variation of such measurements are preferred for the specific type of network considered. In particular, active localization networks leverage the agents capability of exchanging messages with the other network nodes in order to greatly simplify the measurement and scheduling process. Thus, time-based measurements and power-based measurements are usually employed in active localization networks. On the other hand, SRNs typically exploits RTT measurements in both monostatic (i.e., transmitter and receiver are co-located) and multistatic settings (i.e., transmitter and receiver are not co-located) as time-based measurements, while they cannot rely on RSSI measurements for providing accurate localization. Due to the reflections on different materials and the challenging wireless propagation environments considered for SRN operations, accurate models describing the attenuation of the transmitted signal as a function of the distance are difficult to obtain. Even in active localization networks, power-based measurements provides worse accuracy compared to time- and angle-based measurements. However, power measurements are usually carried out for communication purposes and they can also be exploited to perform localization, greatly reducing the complexity of the networks nodes.

2.2   Localization and Tracking

Location inference algorithms can be divided into two categories. Localization algorithms which aim to estimates time-invariant quantities (i.e., the location of the agents or targets) and tracking algorithms which aims to estimates the evolution of the states of a time-varying system (i.e., coordinates, velocity, bearing of the agents or targets) based on noisy observations. Observations are related to the measurements discussed in previous

Section. In particular, observations may be the distance estimate (DE) obtained from time- or power-based measurements, angle estimation (AE) obtained from angle-based measurements, or a combination of both.

Localization can be achieved considering both a non-Bayesian or Bayesian approach [115]. In the former case, the unknown position of the agent or target $\boldsymbol{p}$ is considered as a unknown but deterministic parameter. A well-known estimator employed in the non-Bayesian formulation, is the maximum likelihood (ML) estimator. In particular, given an observation $\boldsymbol{v}$, the estimated position is obtained as

$$\hat{\boldsymbol{p}} = \underset{\boldsymbol{p} \in \mathcal{A}}{\operatorname{argmax}} \, f_{\mathbf{v}}(\boldsymbol{v}; \boldsymbol{p}) \tag{2.1}$$

where $f_{\mathbf{v}}(\boldsymbol{v}; \boldsymbol{p})$ is the likelihood function relating the position $\boldsymbol{p}$ to the observation $\boldsymbol{v}$ and $\mathcal{A}$ is the region where the agent or target may be located. If the likelihood function is Gaussian ML estimator simplifies to least squares (LS) estimators.

In Bayesian approach, the position of the agent or target $\mathbf{p}$ is modeled as a realization of a RV with known PDF $f_{\mathbf{p}}(\boldsymbol{p})$. In this case, any prior information can be easily incorporated and used to refine the position estimates via the a priori distribution of the position. Two estimators are typically employed in Bayesian approach, namely, maximum *a posteriori* (MAP) and minimum-mean-square-error (MMSE) estimators. MAP estimator determines the position estimate as

$$\hat{\boldsymbol{p}} = \underset{\boldsymbol{p} \in \mathcal{A}}{\operatorname{argmax}} \, f_{\mathbf{p}|\mathbf{v}}(\boldsymbol{p}|\boldsymbol{v}) \tag{2.2}$$

$$= \underset{\boldsymbol{p} \in \mathcal{A}}{\operatorname{argmax}} \, f_{\mathbf{v}|\mathbf{p}}(\boldsymbol{v}|\boldsymbol{p}) f_{\mathbf{p}}(\boldsymbol{p}) \tag{2.3}$$

where $f_{\mathbf{p}|\mathbf{v}}(\boldsymbol{p}|\boldsymbol{v})$ is the posterior PDF. On the other hand, position estimate via MMSE estimator is obtained as

$$\hat{\boldsymbol{p}} = \int_{\mathcal{A}} \boldsymbol{p} \, f_{\mathbf{p}|\mathbf{v}}(\boldsymbol{p}|\boldsymbol{v}) d\boldsymbol{p} \,. \tag{2.4}$$

Tracking problem can be formulated as a statistical filtering problem, where the evolution of a time-varying system must be estimated based on noisy observations [48]. A time-varying system can be formally described by two equations: i) the state evolution equation $h(\cdot)$ which describes the relation between the system states at two consecutive time instants t_{k-1} and t_k; and ii) the measurement equation $q(\cdot)$ which describe the relation between the observation and the system state at the same time instant t_k. For tracking, consider $\boldsymbol{p}_k$ the positional state of the agent or target. The two equations can
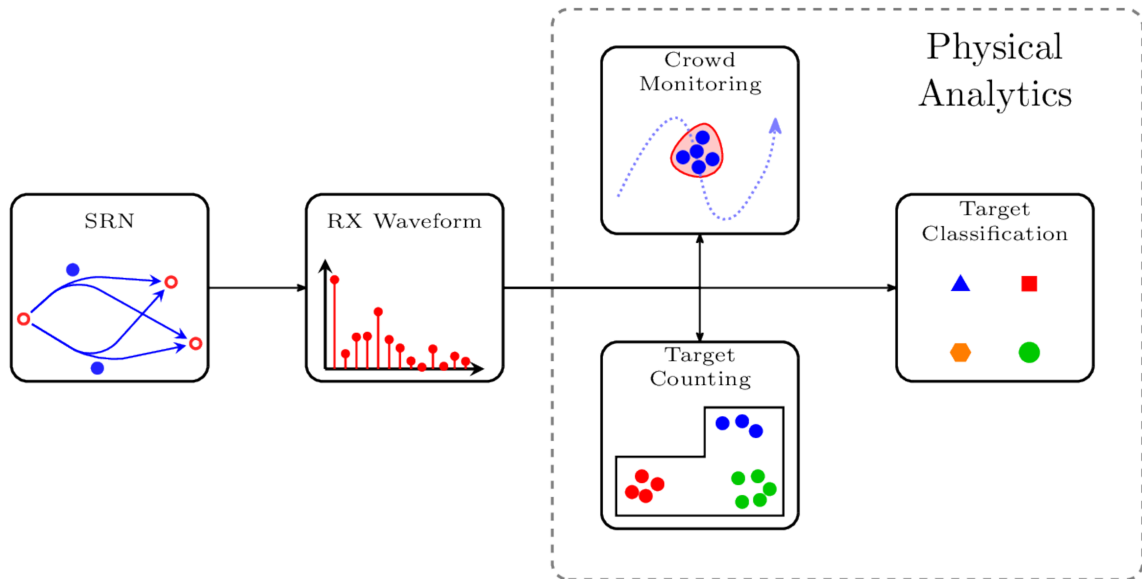
Figure 2.3: Extraction of analytics via SRNs: waveforms received from reflections as input for extracting analytics such as target counting, crowd monitoring, and target classification.

be written as

$$\boldsymbol{p}_k = h(\boldsymbol{p}_{k-1}, \boldsymbol{w}_k) \tag{2.5}$$

$$\boldsymbol{v}_k = q(\boldsymbol{p}_k, \boldsymbol{n}_k) \tag{2.6}$$

where $\boldsymbol{v}_k$ is the observation vector at time instant t_k, $\boldsymbol{w}_k$ is the process noise vector, and $\boldsymbol{n}_k$ is the observation noise vector. Statistical filter refers to the estimation process of the state $\hat{\boldsymbol{p}}_k$ from the all the past observations $\boldsymbol{v}_{(k:1)} = \{\boldsymbol{v}_1, \boldsymbol{v}_2, \ldots, \boldsymbol{v}_k\}$. This is accomplished via the evaluation of the posterior PDF given by

$$f(\boldsymbol{p}_k | \boldsymbol{v}_1, \boldsymbol{v}_2, \ldots, \boldsymbol{v}_k) = \frac{f(\boldsymbol{v}_k | \boldsymbol{p}_k) f(\boldsymbol{p}_k | \boldsymbol{v}_1, \boldsymbol{v}_2, \ldots, \boldsymbol{v}_{k-1})}{f(\boldsymbol{v}_k | \boldsymbol{v}_{k-1})} \, . \tag{2.7}$$

Depending on the functional form of the equations, the distributions of the process noise, and the distributions of the observation noise, different state estimators are employed (e.g., Kalman filter, unscendent Kalman filter, cubature Kalman filter, and particle filter) [116].

2.3   Physical Analytics via Sensor Radar Networks

Physical analytics describing the behavior of the network nodes is fundamental for providing context awareness in wireless networks. This is particularly relevant for SRN, where the backscattered signals provide richer information regarding the environment and the targets compared to the active counterpart. In particular, based on the measurements described for localization purposes is it possible to extract synthetic metrics describing the movements of large groups of targets or the number of targets in a monitored area without relying on the location estimates [104]. For instance, crowd-centric counting methods rely on features related to the energy as well as time-varying analysis of the received signals in order to count the number of targets without incurring in the computational complexity determined by the data association process. In addition, based on the reflected waveforms it is possible to discriminate between different targets (e.g., pedestrian versus vehicles) or infer the specific movement a human target is performing. Typically, this is accomplished evaluating the range-Doppler signature of different type of targets (e.g., range-Doppler signatures of vehicles show noticeable Doppler shifts near the frequencies corresponding to the rotation of the moving parts) via classical classification or machine learning-based techniques [117]. Fig. 2.3 depicts the conceptual scheme for extracting analytics via backscattered signals in SRNs.

Chapter 3

Machine Learning based Localization: SI Approach

Machine learning based localization has recently attracted significant attention from both academia and standardization bodies. In particular, 3GPP is currently evaluating the benefits of augmenting the 5G air-interface with features supporting machine learning based algorithms in order to enhance the d localization accuracy in different UCs scenarios, including those with harsh wireless propagation conditions. Instead of designing localization algorithms based on the exploitation of physical models or geometric theories, machine learning based techniques exploit the ever-increasing volumes of data and computational power to perform location inference in a data-driven manner. In this chapter we review SI-based localization [55], which exploits unsupervised machine learning (UML) techniques to statistically characterize the relation between the observed quantities and the device positional features, and we highlight the main differences compared to classical localization algorithms based on SVE.

3.1 SVE-based Localization

Classical localization methods for active localization networks can be categorized as a SVE-based method. In general, SVE-based localization methods divide the localization process in two stages: (i) a single-value estimation stage in which SVEs of distances, angles, or other position- dependent quantities are measured; and (ii) a localization stage in which prior knowledge and SVEs serve as inputs to a localization algorithm for position inference. This two stages procedure can be formalized as follow; define a measurement $\boldsymbol{y}_i$ obtained by the exchange with the i-th anchor as a collection of measurements obtained by different types of sensors, and where $i \in \mathcal{N}_{\mathrm{BS}} = \{1, 2, \ldots, N_{\mathrm{BS}}\}$. For example, the

measurement vector $\boldsymbol{y}_i$ can include the entire set of waveform samples, time-based, angle-based, and power-based metrics, or any combination of them. These measurements are related to a feature vector $\boldsymbol{\theta}$[1] which is a function of the agent positional state and in particular its position $\boldsymbol{p}$.[2] In the first stage of SVE-based localization methods, the measurements $\{\boldsymbol{y}_i\}_{i \in \mathcal{N}_{\mathrm{BS}}}$ are processed in order to obtain SVEs of the feature vector, i.e., $\{\hat{\boldsymbol{\theta}}_i\}_{i \in \mathcal{N}_{\mathrm{BS}}}$, such as DE or AE [118–121]. In the second stage, the estimates $\{\hat{\boldsymbol{\theta}}_i\}_{i \in \mathcal{N}_{\mathrm{BS}}}$ are used as input to the localization algorithm to obtain an estimate of the agent position $\hat{\boldsymbol{p}}$.[3] Localization accuracy and reliability of conventional SVE-based localization depends heavily on the quality of the estimates $\{\hat{\boldsymbol{\theta}}_i\}_{i \in \mathcal{N}_{\mathrm{BS}}}$, which degrades in harsh propagation environments due to biases in SVEs caused by impairments such as multipath propagation and non line-of-sight (NLOS) conditions [96, 122].

SVE-based localization presents two main advantages. The first stage of the localization process can be accomplished by independent procedures for each measurement vector $\boldsymbol{y}_i$, resulting in robust techniques (e.g., different processing techniques based on the line-of-sight (LOS) or NLOS conditions of the links). In addition, SVE approach bear a lower complexity of the location inference stage compared to machine learning based approaches. On the other hand, SVE-based localization inherently discards part of the positional information contained in the sensing measurements, due to the hard-decision on the SVE. Localization accuracy of SVE-based localization can be improved via refined SVEs, taking into account environmental information, or by discarding measurements particularly affected by the wireless impairments [66, 74, 123–125]. In particular, physical feature extracted from sensing measurements can discriminate measurements that are representative of the agent position or no. In cases where sensing measurements are not representative, they can be discarded and the corresponding SVEs are not used in the location inference. Other solutions which aims at detecting NLOS propagation conditions and then mitigate the errors on feature estimates can also be employed [36, 126–130].

3.2   SI-based Localization

In [55], researchers have proposed and developed a method based on SI to overcome the limitations of SVE-based localization. The SI encapsulates the ensemble of all positional information of the agents and it is composed of soft feature information (SFI) and soft context information (SCI): SFI is the ensemble of positional information associated with

---

[1]For brevity, the dependency of $\boldsymbol{\theta}$ from the agent positional state is omitted in the following.

[2]The positional state, other than the position of the agent, may include the velocity vector, acceleration vector, orientation, and angular velocity. In this work we are only interested in the position $\boldsymbol{p}$.

[3]Observations $\boldsymbol{v}$ discussed in the previous chapter is a vector collecting all the SVEs $\hat{\boldsymbol{\theta}}_i$ obtained from the measurements $\boldsymbol{y}_i$ with $i \in \mathcal{N}_{\mathrm{BS}}$.
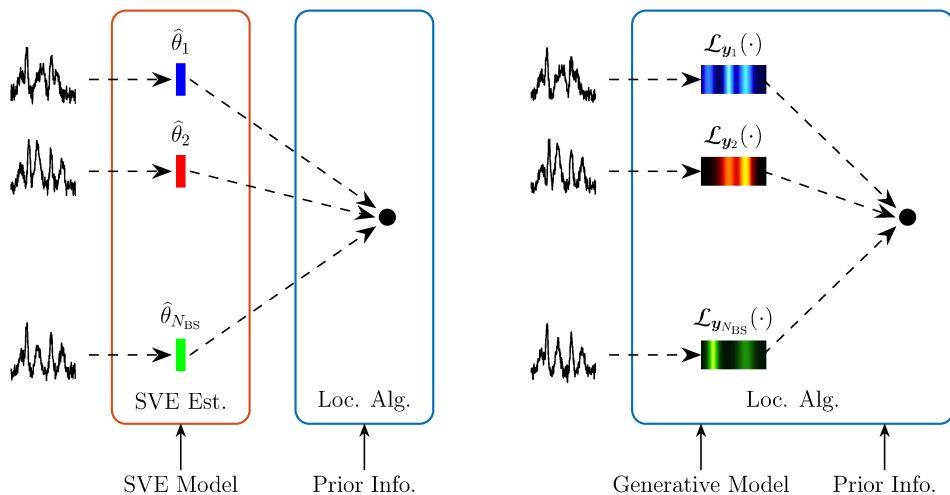
Figure 3.1: Localization techniques based on SVE (left) and on SI (right).

measurements; and SCI is the ensemble of environmental information associated with contextual data. SI-based localization infers agent positions by exploiting both SFI and SCI (see Fig. 3.1 for a comparison between and SVE-based and SI-based localization). In particular, SCI may describe prior knowledge in the form of digital maps, dynamic models, and agent profiles [86, 131–133]. For example, the SCI provided by a map can be incorporated as a prior distribution of the position (e.g., certain positions in the map are very unlikely) or as a conditional distribution of the position at the current time step , given the position at the previous time step (e.g., mobility in a corridor is more likely along the corridor direction then in a perpendicular direction). SCI provided by a dynamic model can be incorporated as a conditional distribution of the positional state at consecutive time steps (e.g., consecutive positions close to each other are highly likely for an agent with low speed). SCI provided by an agent profile can be taken into account as a distribution of different components determining the positional state (e.g., misalignments of velocity vector and the direction are highly unlikely if the agent is a car). The SCI provides additional information on positional states, thus improving the performance of both soft-decision localization and classical hard-decision localization.

In the following we will focus only on the SFI and how SI-based localization can be applied in the context of the wireless networks discussed in this thesis.[4] In particular, the exploitation and generation of SFI obtained by inter-node measurement, i.e., measurements involving an exchange between the agent and anchors, will be discussed. However, the methodology that will be presented can easily be extended to incorporate intra-measurements, i.e., measurements that do not involve the exchange between different nodes, such as inertial measurements from inertial measurement unit (IMU), and

---

[4]The exploitation of SCI and its generation is not directly related to the specific technology employed.

inter-node measurements between different agents.

3.2.1 Soft Feature Information

Formally, the SFI for a measurement $\boldsymbol{y}$ related to the feature $\boldsymbol{\theta}$ is given by

$$\mathcal{L}_{\boldsymbol{y}}(\boldsymbol{\theta}) \propto f_{\mathsf{y}|\boldsymbol{\theta}}(\boldsymbol{y}|\boldsymbol{\theta}) \tag{3.1a}$$

$$\mathcal{L}_{\boldsymbol{y}}(\boldsymbol{\theta}) \propto f_{\mathsf{y}}(\boldsymbol{y};\boldsymbol{\theta}) \tag{3.1b}$$

where it has been displayed the Bayesian and non-Bayesian formulation. In the non-Bayesian formulation, the SFI is equivalent to the likelihood function of $\boldsymbol{\theta}$. Compared to its SVE $\hat{\boldsymbol{\theta}}$, the SFI $\mathcal{L}_{\boldsymbol{y}}(\boldsymbol{\theta})$ provides richer information by accounting probabilistically for all possible values of $\boldsymbol{\theta}$, thus enabling soft-decision localization instead of hard-decision. Depending on the specific measurements, different type of SFI are obtained. For range-related measurements, the corresponding SFI, namely soft range information (SRI), can be written as $\mathcal{L}_{\boldsymbol{y}}(d)$. Similarly, it is defined the soft angle information (SAI) $\mathcal{L}_{\boldsymbol{y}}(\alpha)$ for angle-related measurements.

In addition to provide richer information compared to SVE, the statistical characterization of the relation between the measurements and feature, allows for efficient data fusion. In particular, sensing measurements gathered with different types of sensor can be fused by multiplying their corresponding SFI, as long as the measurements are conditionally independent given the agent position. If such condition is satisfied, given a set of measurements $\mathcal{Y} = \{\boldsymbol{y}^{(j)}\}_{j=1}^{N_{\mathrm{F}}}$ related to the feature set $\Theta = \{\boldsymbol{\theta}^{(j)}\}_{j=1}^{N_{\mathrm{F}}}$ where $\boldsymbol{y}^{(j)}$ is related to $\boldsymbol{\theta}^{(j)}$, the SFI is given by

$$\mathcal{L}_{\mathcal{Y}}(\Theta) = \prod_{j=1}^{N_{\mathrm{F}}} \mathcal{L}_{\boldsymbol{y}^{(j)}}(\boldsymbol{\theta}^{(j)}) \,. \tag{3.2}$$

For example, consider the fusion of range-related and angle-related measurements. In this settings, given the measurement $\boldsymbol{y}^{(1)}$ related to the range d and the measurement $\boldsymbol{y}^{(2)}$ related to the angle α, the resulting SFI obtained by the fusion of SRI and SAI can be written as

$$\mathcal{L}_{\boldsymbol{y}^{(1)},\boldsymbol{y}^{(2)}}(d,\alpha) = \mathcal{L}_{\boldsymbol{y}^{(1)}}(d)\mathcal{L}_{\boldsymbol{y}^{(2)}}(\alpha) \,. \tag{3.3}$$

SFI can be used both in a Bayesian or non-Bayesian settings to infer the agent position $\boldsymbol{p}$. In particular, if the position is considered as an unknown but deterministic parameter

to be estimated, the ML estimates $\hat{\boldsymbol{p}}$ is obtained as

$$
\begin{aligned}
\hat{\boldsymbol{p}} &= \operatorname*{argmax}_{\boldsymbol{p}} f(\{\boldsymbol{y}_i\}_{i\in\mathcal{N}_{\mathrm{BS}}}; \boldsymbol{p}) \\
&= \operatorname*{argmax}_{\boldsymbol{p}} \prod_{i\in\mathcal{N}_{\mathrm{BS}}} \mathcal{L}_{\boldsymbol{y}_i}(\boldsymbol{\theta}_i).
\end{aligned}
\tag{3.4}
$$

If the SFIs are Gaussian, the ML estimate is equivalent to the LS or weighted LS in the case the distribution having the same or different variance, respectively. Alternatively, by modeling the agent position as a RV the estimate can be obtained from the posterior distribution. In particular, MMSE and MAP estimates are obtained as

$$
\hat{\boldsymbol{p}} = \int \boldsymbol{p} f(\boldsymbol{p}|\{\boldsymbol{y}_i\}_{i\in\mathcal{N}_{\mathrm{BS}}})d\boldsymbol{p}
\tag{3.5a}
$$

$$
\hat{\boldsymbol{p}} = \operatorname*{argmax}_{\boldsymbol{p}} f(\boldsymbol{p}|\{\boldsymbol{y}_i\}_{i\in\mathcal{N}_{\mathrm{BS}}})
\tag{3.5b}
$$

respectively. The posterior distribution is given by

$$
f(\boldsymbol{p}|\{\boldsymbol{y}_i\}_{i\in\mathcal{N}_{\mathrm{BS}}}) \propto \prod_{i\in\mathcal{N}_{\mathrm{BS}}} \mathcal{L}_{\boldsymbol{y}_i}(\boldsymbol{\theta}_i).
\tag{3.6}
$$

If the prior distribution of $\mathbf{p}$ is constant the ML and MAP estimates coincide.

3.2.2   Soft Feature Information Generation

SFI can be determined using a Bayesian formulation, and in particular leveraging the joint probability distribution of the measurement vector $\boldsymbol{y}$ and feature vector $\boldsymbol{\theta}$, referred to as generative model. Depending on the absence or presence of prior information on the feature vector $\boldsymbol{\theta}$, the SFI is determined by

$$
\mathcal{L}_{\boldsymbol{y}}(\boldsymbol{\theta}) \propto f_{\mathbf{y},\boldsymbol{\theta}}(\boldsymbol{y}, \boldsymbol{\theta})
\tag{3.7a}
$$

$$
\mathcal{L}_{\boldsymbol{y}}(\boldsymbol{\theta}) \propto \frac{1}{f_{\boldsymbol{\theta}}(\boldsymbol{\theta})} f_{\mathbf{y},\boldsymbol{\theta}}(\boldsymbol{y}, \boldsymbol{\theta})
\tag{3.7b}
$$

respectively. Thus, the task of determining the SFI reduces to the determination of the generative model relating the measurements to the agent positional feature. In complex scenarios, this is typically accomplished by employing UML techniques applied on measurements and positional feature data acquired in the scenario of interest. In particular, a two phases algorithm is used to estimate the generative model based on density estimation techniques. The algorithm works as follow:

i) off-line phase where a generative model estimate is obtained from the measurements and positional feature data; and

ii) on-line phase where the generative model estimate is used to determine the SFI associated to each new measurement.

The generative model determined by the algorithm is suited for the environment where the on-line phase takes place, i.e., where the localization systems will operate. However, a generative model learned in a specific environment can be used in different environments, as long as the different environments are similar in terms of propagation characteristics for inter-node measurements.

Inferring the generative model can be difficult for measurement vectors with high dimensionality, e.g., waveform samples with fine time resolution. Therefore, dimensionality reduction techniques can be employed to facilitate the learning process and reduce the algorithm complexity. In particular, the measurement vector $\boldsymbol{y} \in \mathbb{R}^M$ can be mapped through the function $\psi(\cdot)$ to a lower dimension space, i.e., $\psi(\boldsymbol{y}) \in \mathbb{R}^{M'}$ where $M' << M$. Typically, UML techniques are used to perform dimensionality reduction, such as principal component analysis, Laplacian eigenmap, or approximation via neural networks. SVE can also be seen as a type of dimensionality reduction, where the samples of the received waveform are considered as measurement vector and the mapping is given by $\psi(\boldsymbol{y}) = \hat{\boldsymbol{\theta}}$. In general, any quantity which can be calculated from the received waveform and it can be related to the positional feature, e.g., maximum value, power, excess delay, kurtosis of the received waveform, or combination of them, can be interpreted as a dimensionality reduction.

In the following will be presented a widely used density estimation technique based on the Gaussian mixture model (GMM) used to determine the generative model [134]. For notational convenience, consider the vector $\boldsymbol{x} = [\boldsymbol{y}^{\mathrm{T}}, \boldsymbol{\theta}^{\mathrm{T}}]^{\mathrm{T}}$ or $\boldsymbol{x} = [\psi(\boldsymbol{y})^{\mathrm{T}}, \boldsymbol{\theta}^{\mathrm{T}}]^{\mathrm{T}}$ if dimensionality reduction techniques are employed. In this case, the generative model to be estimated is $f(\boldsymbol{x}) = f(\boldsymbol{y}, \boldsymbol{\theta})$. Prior to the density estimation process, it is beneficial to pre-process the data in order to scale and normalize the different variables. In particular, data sphering is linear transformation that maps the original data into a set with zero-mean and identity covariance matrix. Given the set of original data $\{\boldsymbol{x}_l\}_{l \in \mathcal{N}_{\mathrm{T}}}$ with $\mathcal{N}_{\mathrm{T}} = \{1, 2, \ldots, N_{\mathrm{T}}\}$, where N_{T} is the number of training data and the measurement and positional feature data are $\boldsymbol{y}_l$ and $\boldsymbol{\theta}_l$, respectively, the processed data after sphering are

$$\boldsymbol{z}_l = \boldsymbol{\Lambda}^{-\frac{1}{2}} \boldsymbol{U}^{\mathrm{T}} (\boldsymbol{x}_l - \bar{\boldsymbol{x}}) \tag{3.8}$$

where $\bar{\boldsymbol{x}}$ is the empirical mean of the original data, and $\boldsymbol{U} \boldsymbol{\Lambda} \boldsymbol{U}^{\mathrm{T}}$ is the spectral decomposi-

tion of the empirical covariance matrix of the original data $\{\boldsymbol{x}_l\}_{l\in\mathcal{N}_\mathrm{T}}$.[5] Then, the estimated density of the non-sphered data $\hat{f}_\mathsf{x}(\boldsymbol{x})$ can be easily obtained from the estimated density $\hat{f}_\mathsf{z}(\boldsymbol{z})$ as follow

$$
\begin{aligned}
\hat{f}_\mathsf{x}(\boldsymbol{x}) &= |\det(\boldsymbol{\Lambda}^{-\frac{1}{2}}\boldsymbol{U}^\mathrm{T})|\hat{f}_\mathsf{z}(\boldsymbol{z}) \\
&= |\det(\boldsymbol{\Lambda}^{-\frac{1}{2}}\boldsymbol{U}^\mathrm{T})|\hat{f}_\mathsf{z}(\boldsymbol{\Lambda}^{-\frac{1}{2}}\boldsymbol{U}^\mathrm{T}(\boldsymbol{x}_l - \bar{\boldsymbol{x}}))\,.
\end{aligned}
\tag{3.9}
$$

Suppose the sphered data $\{\boldsymbol{z}_l\}_{l\in\mathcal{N}_\mathrm{T}}$ as realizations of independent, identically distributed (IID) RVs following a Gaussian mixture (GM) distribution given by

$$
\tilde{f}(\boldsymbol{z};\mathcal{P}) = \sum_{k=1}^{N_\mathrm{GM}} \pi_k \varphi(\boldsymbol{z};\boldsymbol{\mu}_k,\boldsymbol{\Sigma}_k)
\tag{3.10}
$$

where the weights $\pi_k \in \mathbb{R}^+$ for $k = 1, 2, \ldots, N_\mathrm{GM}$, $\sum_{k=1}^{N_\mathrm{GM}} \pi_i = 1$ and the set of parameters $\mathcal{P} = \{\pi_1, \boldsymbol{\mu}_1, \boldsymbol{\Sigma}_1, \pi_2, \boldsymbol{\mu}_2, \boldsymbol{\Sigma}_2, \ldots, \pi_{N_\mathrm{GM}}, \boldsymbol{\mu}_{N_\mathrm{GM}}, \boldsymbol{\Sigma}_{N_\mathrm{GM}}\}$ along with the number of Gaussian components N_GM define the distribution. Then, the problem of obtaining the estimate $\hat{f}(\boldsymbol{z})$ is equivalent to the problem of determining the optimum set of parameters $\hat{\mathcal{P}}$ which can describe the sphered data $\{\boldsymbol{z}_j\}_{l\in\mathcal{N}_\mathrm{T}}$, i.e., $\hat{f}(\boldsymbol{z}) = \tilde{f}(\boldsymbol{z};\hat{\mathcal{P}})$. This problem can be solved applying a ML approach, and in particular, given the IID assumption, the log-likelihood function can be written as

$$
\ln\left\{\tilde{f}(\{\boldsymbol{z}_l\}_{l\in\mathcal{N}_\mathrm{T}};\mathcal{P})\right\} = \sum_{l=1}^{N_\mathrm{T}} \ln\left\{\sum_{k=1}^{N_\mathrm{GM}} \pi_k \varphi(\boldsymbol{z}_l;\boldsymbol{\mu}_k,\boldsymbol{\Sigma}_k)\right\}
\tag{3.11}
$$

and the optimal set of parameters $\hat{\mathcal{P}}$ in ML sense is obtained maximizing (3.11), i.e.,

$$
\hat{\mathcal{P}} = \underset{\mathcal{P}}{\operatorname{argmax}} \ln f(\{\boldsymbol{z}_l\}_{l\in\mathcal{N}_\mathrm{T}};\mathcal{P})\,.
\tag{3.12}
$$

No closed-form solution can be obtained for (3.12) and iterative algorithms are employed to determine an approximate ML solution. Among the available algorithms typically used to solve (3.12), we briefly present the expectation-maximization (EM) algorithm which works as follow [134]:

1. initialize the set parameter $\mathcal{P}$ by performing clustering on the data $\{\boldsymbol{z}_l\}_{l\in\mathcal{N}_\mathrm{T}}$ (e.g., via k-means algorithm [135]), with the number of cluster equal to the number of components in the GM N_GM. The parameters π_k, $\boldsymbol{\mu}_k$, and $\boldsymbol{\Sigma}_k$ are calculated as the fraction of data $\boldsymbol{z}_l$ assigned to the k-th cluster, the empirical mean and empirical

---

[5]$\boldsymbol{\Lambda}$ is a diagonal matrix where the diagonal elements are given by the eigenvalues of the empirical covariance matrix, and the columns of $\boldsymbol{U}$ are given by the corresponding eigenvectors.

covariance of the data $\boldsymbol{z}_l$ assigned to the k-th cluster, respectively.

2. starting from the current values of the parameters, calculate the following quantities

$$\gamma_{l,k} = \pi_k \frac{\varphi(\boldsymbol{z}_l; \boldsymbol{\mu}_k, \boldsymbol{\Sigma}_k)}{\tilde{f}(\boldsymbol{z}_l; \mathcal{P})} \tag{3.13a}$$

$$\Gamma_k = \sum_{j=1}^{N_\mathrm{T}} \gamma_{l,k} \,. \tag{3.13b}$$

3. update the weights, mean vectors and covariance matrices as follow

$$\pi_k^\mathrm{new} = \frac{\Gamma_k}{N_\mathrm{T}} \tag{3.14a}$$

$$\boldsymbol{\mu}_k^\mathrm{new} = \frac{1}{\Gamma_k} \sum_{l=1}^{N_\mathrm{T}} \gamma_{l,k} \boldsymbol{z}_l \tag{3.14b}$$

$$\boldsymbol{\Sigma}_k^\mathrm{new} = \frac{1}{\Gamma_k} \sum_{l=1}^{N_\mathrm{T}} \gamma_{l,k} (\boldsymbol{z}_l - \boldsymbol{\mu}_k^\mathrm{new})(\boldsymbol{z}_l - \boldsymbol{\mu}_k^\mathrm{new})^\mathrm{T} \,. \tag{3.14c}$$

4. evaluate the log-likelihood function (3.11) with the new parameters (3.14) and check for convergence of either the log-likelihood or the parameters. If convergence is not achieved, repeat from point 2.

EM algorithm is widely employed due to its simplicity and flexibility and it can be proved that at each iteration the log-likelihood function value is increased. However it is not guaranteed that it will converge to the global maximum of the function. Moreover, the convergence rate strongly depends on the initialization parameters. Multiple runs of the EM can be done with different initialization parameter, and consider the solution with the highest log-likelihood value.

Density estimation via GMM produces a parsimonious generative model characterized by a small number of parameters π_i, $\boldsymbol{\mu}_i$, and $\boldsymbol{\Sigma}_i$ for $i = 1, 2, \ldots, N_\mathrm{GM}$ where the only free parameter is the number of components in the GM N_GM. However, generative models with a fixed number of parameters may not be suitable to capture complex relation between the measurement and feature vectors.

Chapter 4

Localization in 5G Networks

Location awareness [1, 2, 114] is critical in many vertical applications enabled by 5G networks, including autonomy [9–11, 136], crowdsensing [13, 15, 137, 138], smart environments [18, 20, 139, 140], and Internet-of-Things [69, 141–143]. Extracting accurate location information is considered an important feature in 5G network and represents a fundamental component of the 3GPP standardization process. Moreover, user equipments (UEs) location information has become a valuable asset for network operation, enabling operators to perform smart-network management based on the location information of their customer users [23–25, 144]. In this chapter, the localization aspects of current 5G networks are presented and discussed. In particular, KPI requirements, reference signals, and measurements procedures for localization based on DL-TDOA are detailed.

4.1 Localization Requirements

The standardization for location-based services (LBSs) in 5G and B5G networks is based on various use case scenarios and network operating conditions. The service level requirements for the use cases are specified in terms of KPIs that are related to the localization of user equipments (UEs). The main KPIs defined by 3GPP are horizontal and vertical accuracy, availability, and latency. Other important KPIs are related to the power consumption and energy needed for localization, and the scalability with the number of UEs.

The 3GPP specification [32] describes seven positioning service levels (PSLs) as summarized in Tab. 4.1. Such requirements are given in terms of absolute (A) position of a UE or of relative (R) position between two UEs or between one UE and another 5G network node; and in terms of horizontal (H) and vertical (V) accuracy. The table also reports the service availability and the latency associated with each level. Requirements are

Table 4.1: Service level requirements, also referred to as PSLs (first column), for 5G localization according to the 3GPP TS 22.261 [32].

PSL	A/R	Accuracy		Availability	Latency	Environment and Velocity	
		H	V			Positioning Service Area	Enhanced Positioning Service Area
1	A	10 m	3 m	95%	1 s	Indoor (30 km/h); Outdoor (rural and urban; 250 km/h)	Indoor (30 km/h)
2	A	3 m	3 m	99%	1 s	Outdoor (rural and urban; trains 500 km/h; others 250 km/h)	Outdoor (dense urban; 60 km/h; roads 250 km/h; railways 500 km/h); Indoor (30 km/h)
3	A	1 m	2 m	99%	1 s	Outdoor (rural and urban; trains 500 km/h; others 250 km/h)	Outdoor (dense urban 60 km/h; roads 250 km/h; railways 500 km/h); Indoor (30 km/h)
4	A	1 m	2 m	99.9%	15 ms	NA	Indoor (30 km/h)
5	A	0.3 m	2 m	99%	1 s	Outdoor (rural 250 km/h)	Outdoor (dense urban 60 km/h; roads and railways 250 km/h); Indoor (30 km/h)
6	A	0.3 m	2 m	99.9%	10 ms	NA	Outdoor (dense urban 60 km/h); Indoor (30 km/h)
7	R	0.2 m	0.2 m	99%	1 s	Indoor and outdoor (rural, urban, dense urban) 30 km/h; the relative positioning is between UEs or other positioning nodes within 10 m distance from each other	

specified for a general positioning service area or an enhanced positioning service area for different maximum speeds.Notice that most of the foreseen services require high accuracy (horizontal and vertical precision below a meter over 99% of instantiations) and, some of them, low latency (location updates every few tens of milliseconds) even in complex wireless environments. These requirements can be fulfilled by exploiting multimodal network capabilities, where both radio access technology (RAT)-dependent and RAT-independent measurements are jointly used for inferring UE positional states.

4.2   Localization Measurements

The 3GPP standard has specified, since earlier releases, the signals dedicated to localization or those that can be exploited for localization, including the PRS in down-link and the sounding reference signal in up-link. Related measurements that carry positional information are the down-link and up-link time-difference-of-arrival (TDOA), the AOA, and the angle-of-departure (AOD). Other types of measurements related to UE positional states can also be considered, particularly in private networks. Therefore, examples of measure-
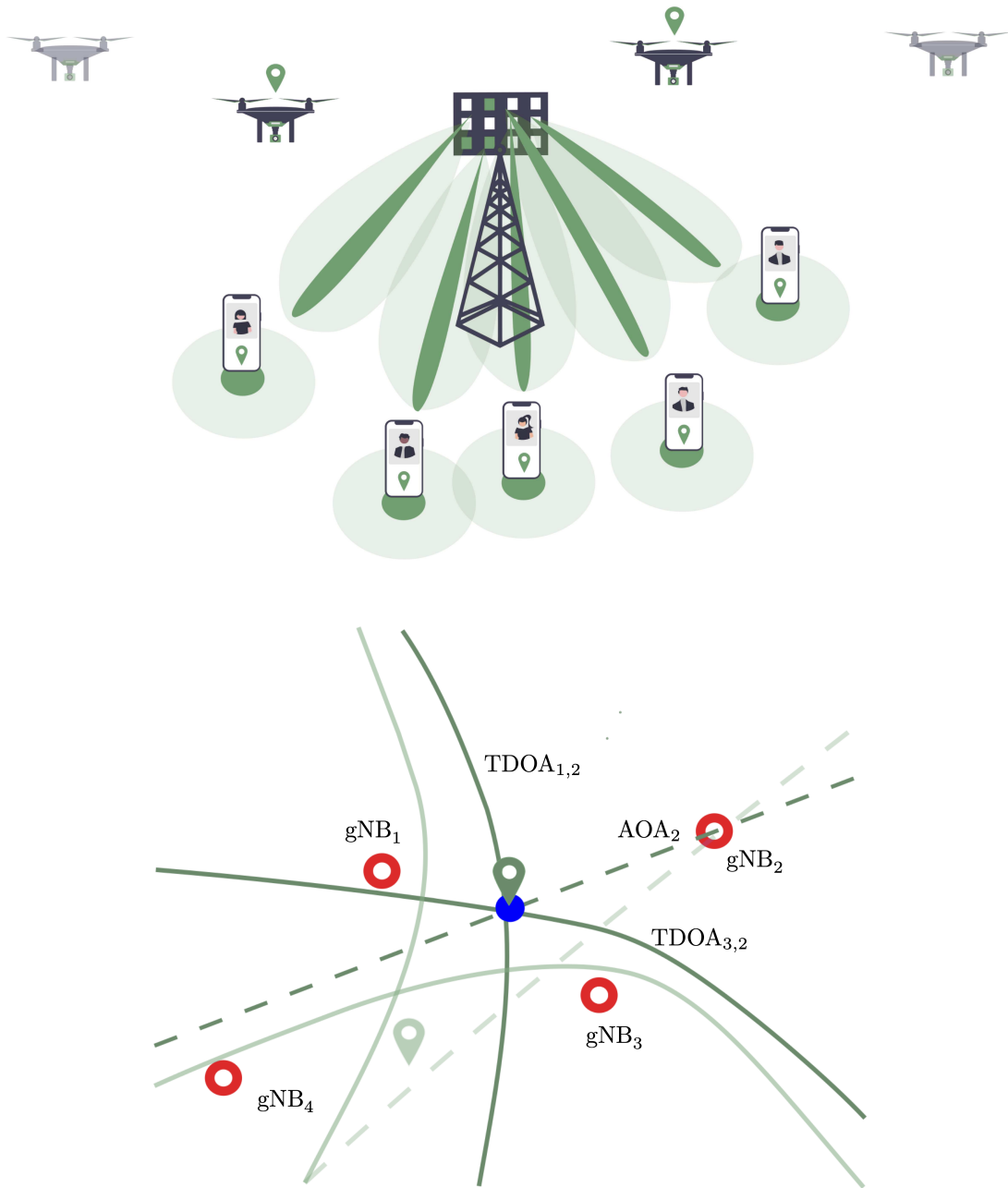
Figure 4.1: Example of accurate positional information exploited for network management; a next generation NodeBs (gNB), employing pencil beams based on estimated UE position, communicates with five users. The lower/higher uncertainty in the estimated UE position is depicted using dark/light green ellipses.

ments for location awareness include (i) inter-node measurements, commonly obtained by radio measurement units; and (ii) intra-node measurements, commonly obtained by inertial measurement units. The environmental information associated with a UE can also be used as prior information to improve the localization accuracy. Examples of environmental information include digital maps, dynamic models, and UE profiles. The accuracy of location awareness is strongly affected by the quality of measurements and by the

knowledge of the environment. Fig. 4.1 illustrates an example of position estimation with accurate and inaccurate measurements for LBSs and shows how network management can exploit higher localization accuracy, specifically for pencil beamforming [145]. Two beamwidths are considered, where a smaller/larger beamwidth (dark/light green beams) is used in case of lower/higher uncertainty. Positional information can also be used to guide mobile gNB nodes exemplified by drones. In the bottom part of the figure, an example is shown for estimated UE position with lower/higher uncertainty (dark/light green) obtained with two TDOA measurements and one AOA measurement in the presence of four gNBs (empty red circles) and a single UE (blue circle).

The following sections provides an overview of the 5G localization solutions based on DL-TDOA measurements. Localization methods based on DL-TDOA measurements are the most mature and well-established solutions. In particular, the PRS and the specific measurement associated are detailed. Algorithms used for inferring DL-TDOA measurements and localization algorithms commonly employed will also be presented.

4.3   Positioning Reference Signal

5G networks employ as default modulation orthogonal frequency division multiplexing (OFDM) with cyclic prefix (CP) addition in order to achieve robustness with respect to the wireless channel impairments. Compared to previous generation, the subcarrier (SC) spacing, namely numerology, is a parameter which can be chosen depending on the available channel bandwidth. Given a numerology μ, a resource grid of $N_{\text{grid}}^{\text{size},\mu} N_{\text{sc}}^{\text{RB}}$ SCs and $N_{\text{symb}}^{\text{subframe},\mu}$ OFDM symbols is defined, where the number of SCs per resource block (RB) is fixed to $N_{\text{sc}}^{\text{RB}} = 12$. The time-continuous signal representing the l-th OFDM symbol, $s_l^{(p,\mu)}(t)$, on the antenna port p given the numerology μ in a subframe, i.e., $l \in \{0, 1, \ldots, N_{\text{symb}}^{\text{subframe},\mu}\}$, is given by

$$s_l^{(p,\mu)}(t) = \sum_{k=0}^{N_{\text{grid}}^{\text{size},\mu} N_{\text{sc}}^{\text{RB}}-1} a_{k,l}^{(p,\mu)} g_{k,l}^{(\mu)}(t) \tag{4.1}$$

for $t \in [t_{\text{start},l}^{\mu}, t_{\text{start},l}^{\mu} + T_{\text{symb},l}^{\mu})$, where

$$g_{k,l}^{(\mu)}(t) = \exp\left\{2\pi\Delta f(k + k_0^{\mu} - N_{\text{grid}}^{\text{size},\mu} N_{\text{sc}}^{\text{RB}}/2)\times \right.$$
$$\left. \times (t - N_{\text{CP},l}^{\mu} T_{\text{C}} - t_{\text{start},l}^{\mu})\right\} \tag{4.2}$$

23

and k_0^μ is a SC offset depending on the resource grid and maximum numerology supported by the transmitter, $T_{\text{symb},l}^\mu = (N_{\text{u}}^\mu + N_{\text{CP},l}^\mu)T_{\text{C}}$, and $T_{\text{C}} = 0.508$ ns is the basic time unit in 5G [146]. The quantity N_{u}^μ is equal to

$$N_{\text{u}}^\mu = 2048\kappa \times 2^{-\mu} \tag{4.3}$$

where $\kappa = 64$ [146], and the quantity $N_{\text{CP},l}^\mu$ for normal CP follows the relation

$$N_{\text{CP},l}^\mu = \begin{cases} 144\kappa \times 2^{-\mu} + 16\kappa & \text{if } l = 0 \text{ or } l = 7 \times 2^\mu \\ 144\kappa \times 2^{-\mu} & \text{otherwise} \end{cases}. \tag{4.4}$$

The PRS was introduced in long-term evolution (LTE) Release 9 [147] and it has been updated for the 5G wireless networks expanding its flexibility in terms of frequency and time slot allocation. Similar to LTE, this reference signal is transmitted in low interference slots, i.e., slots where no data is transmitted. A cell-specific frequency shift dependent on the physical cell identity (PCI) is applied to the PRS pattern, which helps avoiding collisions between PRS transmission of neighbor cells. The sequence used to generate the PRS is a 31-long Gold sequence, where the seed is generated based on the PCI value . The 31-long Gold pseudo-random sequence is defined as

$$c[m] = (c_1[m + N_{\text{C}}] + c_2[m + N_{\text{C}}]) \mod 2 \tag{4.5}$$

where

$$c_1[m + 31] = (c_1[m + 3] + c_1[m]) \mod 2 \tag{4.6}$$

$$\begin{aligned} c_2[m + 31] =& (c_2[m + 3] + c_2[m + 2]+ \\ &+ c_2[m + 1] + c_2[m]) \mod 2 \,. \end{aligned} \tag{4.7}$$

In (4.5), $N_{\text{C}} = 1600$ and (4.6) is initialized such that $c_1[0] = 1$, $c_1[m] = 0$ for $m = 1, 2, \ldots, 30$. The second sequence given by (4.7) is initialized such that $c_{\text{init}}^{\text{PRS}} = \sum_{n=0}^{30} c_2[n]2^n$, where $c_{\text{init}}^{\text{PRS}}$ depend on the PCI. In particular, the seed $c_{\text{init}}^{\text{PRS}}$ of the sequence $c_2[m]$ is given by (4.8) at the top of the next page, where $n_{\text{ID,seq}}^{\text{PRS}} \in \{0, 1, \ldots, 4095\}$ is a transmission specific ID used to distinguish different PRS signals, $N_{\text{symb}}^{\text{slot}} = 14$ is the number of symbols per slot fixed by the standards, $n_{\text{s,f}}^\mu$ is the slot index within a frame given a specific numerology μ, and l is the symbol index given a generic start index l_{start}. The binary sequence in (4.5) is then modulated via quadrature phase-shift keying (QPSK)-modulation and mapped to resource elements (REs) over a specific time-frequency pattern as described in

$$c_{\text{init}}^{\text{PRS}} = \left(2^{22} \left\lfloor \frac{n_{\text{ID,seq}}^{\text{PRS}}}{1024} \right\rfloor + 2^{10} \left(N_{\text{symb}}^{\text{slot}} n_{\text{s,f}}^{\mu} + l + 1 \right) \left(2(n_{\text{ID,seq}}^{\text{PRS}} \mod 1024) + 1 \right) + \right.$$

$$\left. + \left(n_{\text{ID,seq}}^{\text{PRS}} \mod 1024 \right) \right) \mod 2^{31} \qquad (4.8)$$

detail in [146]. In particular, the sequence $c[m]$ is mapped to the symbols $s[m]$ following the equation

$$s[m] = \frac{1}{\sqrt{2}}(1 - 2c[m]) + \jmath \frac{1}{\sqrt{2}}(1 - 2c[m+1]). \qquad (4.9)$$

Given a specific antenna port p and numerology μ, the symbols $s[m]$ are then mapped to the REs $(l,k)_{p,\mu}$, i.e., the k-th SC of the l-th symbol, when (l,k) satisfies the following conditions

$$\begin{cases} k & = mK_{\text{comb}}^{\text{PRS}} + \left((k_{\text{offset}}^{\text{PRS}} + k') \mod K_{\text{comb}}^{\text{PRS}} \right) \\ l & = l_{\text{start}}^{\text{PRS}}, l_{\text{start}}^{\text{PRS}} + 1, \ldots, l_{\text{start}}^{\text{PRS}} + L_{\text{PRS}} - 1 \end{cases} \qquad (4.10)$$

where $m = 0, 1, \ldots$, $l_{\text{start}}^{\text{PRS}}$ is the index of the first PRS symbol within an allocated transmission slot, $L_{\text{PRS}} \in \{2, 4, 6, 12\}$ is the number of transmitted PRS symbols within a slot, $K_{\text{comb}}^{\text{PRS}} \in \{2, 4, 6, 12\}$ is the comb size, i.e., the frequency reuse factor, $k_{\text{offset}}^{\text{PRS}} = \{0, 1, \ldots, K_{\text{comb}}^{\text{PRS}}\}$ is a SC offset with respect to the first SC allocated for PRS transmission, and the quantity k' is an additional SC index offset which depends on the difference $l - l_{\text{start}}^{\text{PRS}}$.[1] Thus, the (l,k) RE given a PRS transmission can be written as

$$a_{k,l}^{(p,\mu)} = \begin{cases} \beta_{\text{PRS}} s[m] & \text{if } (l,k) \text{ satisfies (4.10)} \\ 0 & \text{otherwise} \end{cases} \qquad (4.11)$$

where β_{PRS} is a scale coefficient, $k = 0, 1, \ldots N_{\text{FFT}}^{\text{PRS}} - 1$, and $l = 0, 1, \ldots, N_{\text{symb}}^{\text{slot}}$. The quantity $N_{\text{FFT}}^{\text{PRS}}$ represents the number of SCs allocated for PRS transmission and it is defined as

$$N_{\text{FFT}}^{\text{PRS}} = N_{\text{sc}}^{\text{RB}} N_{\text{RB}}^{\text{PRS}} \qquad (4.12)$$

where $N_{\text{sc}}^{\text{RB}} = 12$ is the number of SC per RB and $N_{\text{RB}}^{\text{PRS}}$ the number of RB allocated

---

[1]The possible values of k' can be found in Tab. 7.4.1.7.3-1 at p. 112 in [146]

for the PRS. With respect ot the general formulation of a modulated 5G signal in (4.1), $N_{\text{FFT}}^{\text{PRS}} = N_{\text{grid}}^{\text{size},\mu} N_{\text{sc}}^{\text{RB}}$ while the other quantities are determined by the specific central frequency and channel used for transmitting the PRS.

In order to facilitate the PRS reception procedure, the time slots allocated for PRS transmission are organized in three different interrelated logical entities: (i) positioning frequency layers; (ii) PRS resource sets; and (iii) PRS resources. Each entity determines a subset of parameters defining the PRSand the three entities follows a hierarchic relationship: different PRS resources are grouped in a PRS resource set, and PRS resource sets are grouped in a positioning frequency layer. In particular, the PRS time signal is transmitted when the quantity $z(n_{\text{f}}, n_{\text{s,f}}^{\mu})$, which depends on the frame number n_{f} and slot number $n_{\text{s,f}}^{\mu}$, fulfills the following condition

$$z(n_{\text{f}}, n_{\text{s,f}}^{\mu}) \quad \text{mod } 2^{\mu} T_{\text{per}}^{\text{PRS}} \in \left\{ n T_{\text{gap}}^{\text{PRS}} \right\}_{n=0}^{T_{\text{rep}}^{\text{PRS}}-1} \tag{4.13}$$

where $T_{\text{per}}^{\text{PRS}} \in \{4, 5, 8, 10, 16, 20, 32, 40, 64, 80, 160, 320, 640,$
$1280, 2560, 5120, 10240\}$ is the PRS transmission periodicity, $T_{\text{gap}}^{\text{PRS}} \in \{1, 2, 4, 8, 16, 32\}$ is the time gap in slots between two instance of PRS resource belonging to the same set, $T_{\text{rep}}^{\text{PRS}} \in \{1, 2, 4, 6, 8, 16, 32\}$ is the number of repeated in a single instance of PRS resource set. The quantity $z(n_{\text{f}}, n_{\text{s,f}}^{\mu})$ is defined as

$$z(n_{\text{f}}, n_{\text{s,f}}^{\mu}) = N_{\text{slot}}^{\text{frame},\mu} n_{\text{f}} + n_{\text{s,f}}^{\mu} - T_{\text{offset}}^{\text{PRS}} - T_{\text{offset,res}}^{\text{PRS}} \tag{4.14}$$

where $T_{\text{offset}}^{\text{PRS}} \in \{0, 1, \ldots, T_{\text{per}}^{\text{PRS}} - 1\}$ is the slot offset relative to the PRS resource set, and $T_{\text{offset,res}}^{\text{PRS}}$ is the slot offset of the PRS resource in the PRS resource set. Additional conditions and constraints on the transmission of the PRS resource set and resource are present if muting patterns are provided. From [148], a PRS resource is defined by a resource list, listing all the PRS resource in the resource set, an unique PRS resource set ID used to identify the specific resource in the set, the seed used to generate the PRS sequence $n_{\text{ID,seq}}^{\text{PRS}}$, the initial frequency offset of the first PRS symbol $k_{\text{offset}}^{\text{PRS}}$, the resource slot offset with respect to the resource set slot offset, the starting symbols for the PRS withing the slot $l_{\text{start}}^{\text{PRS}}$, the number of symbols L_{PRS}, an indication for identify if other reference signals are superimposed with the PRS, and the RB block offset with respect to the zero SC index of the resource grid allocated. Each instantiation of a PRS resource is refereed as a PRS occasion. A PRS resource set is defined by a resource set ID, the time allocation parameters $T_{\text{per}}^{\text{PRS}}$, $T_{\text{rep}}^{\text{PRS}}$, $T_{\text{gap}}^{\text{PRS}}$ (configured only if $T_{\text{rep}}^{\text{PRS}} \neq 1$), a bit map representing a muting pattern for the transmission, $T_{\text{offset}}^{\text{PRS}}$, $T_{\text{offset,res}}^{\text{PRS}}$, the comb size $K_{\text{comb}}^{\text{PRS}}$, and the bandwidth allocated for the PRS defined in terms of RB, $N_{\text{RB}}^{\text{PRS}}$, starting from a
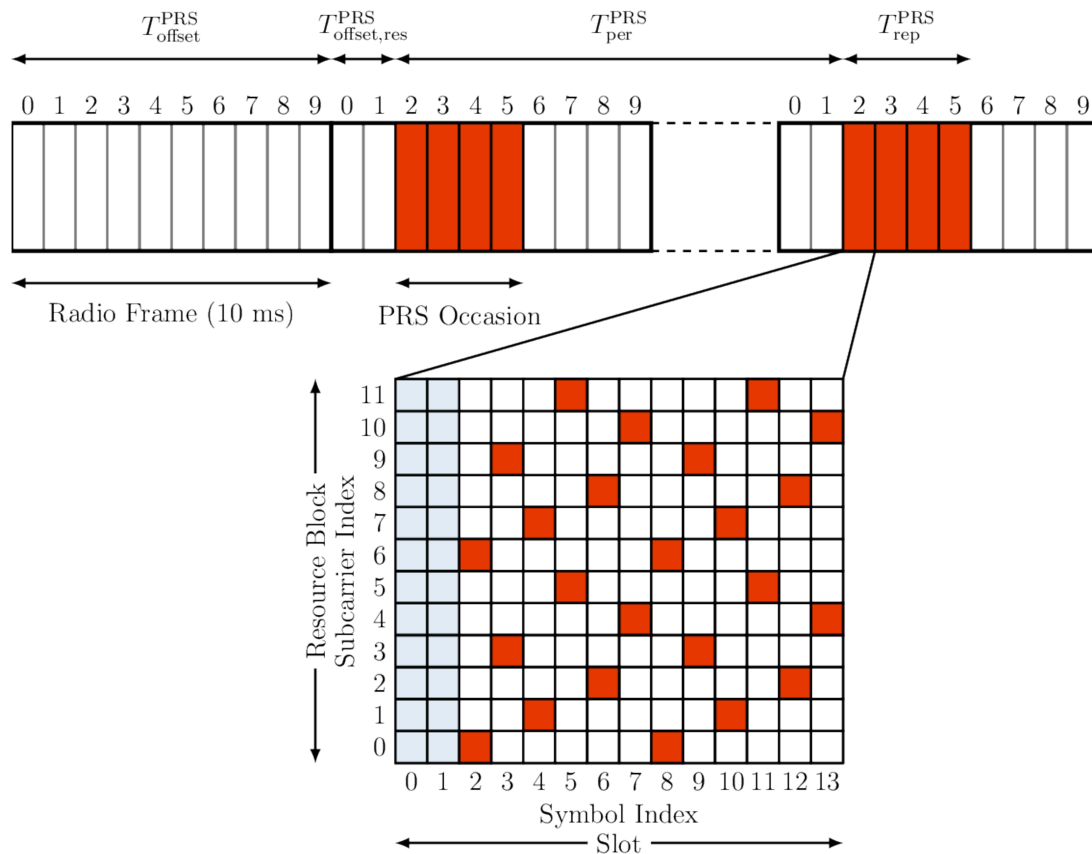
Figure 4.2: Example of PRS occasions considering the numerology $\mu = 0$, i.e., where one slot occupies an entire subframe. In the example $T_{\text{offset}}^{\text{PRS}} = 10$, $T_{\text{offset,res}}^{\text{PRS}} = 2$, $T_{\text{rep}}^{\text{PRS}} = 4$, and $T_{\text{gap}}^{\text{PRS}} = 0$. For the time-frequency allocation of the PRS in one RB, the parameter in the example are: $K_{\text{comb}}^{\text{PRS}} = 6$, $k_{\text{offset}}^{\text{PRS}} = 0$, $l_{\text{start}}^{\text{PRS}} = 2$, and $L_{\text{PRS}} = 12$.

minimum of 24 to a maximum of 272, with a granularity of 4. The positioning frequency layer defines the SC spacing of all the PRS resource sets belonging to the layer, the cyclic prefix used for the transmission, and the absolute frequency point for the resource grid allocated for the PRS transmission. In Fig. 4.2 are depicted multiple 5G radio frames with two PRS occasions. The time-frequency grid of the PRS signal is also depicted for a particular set of parameters. In Tab. 4.2 are reported the main quantities used through the section and their significance.

4.4   DL-TDOA Estimation

In order to determine DL-TDOA measurements, the reference gNB provides the UE with initial information specifying a time window where the PRSs from the different gNBs involved in the localization procedure should be received. The time window where the UE listen for the PRSs is determined by a first coarse position estimate obtained via proximity

methods such as enhanced cell ID. During the time window, the UE can estimate PRS TOA via various methods. Consider a specific realization of the PRS $r(t)$ received by the UE via multipath propagation, i.e.,

$$r(t) = \sum_{i=0}^{N_{\text{path}}} \psi^{(i)} s(t - \tau^{(i)}) + w(t) \tag{4.15}$$

where N_{path} denotes the number of multipath components, $\psi^{(i)}$ and $\tau^{(i)}$ denote the complex amplitude and delay of the i-th path, respectively, and $w(t)$ the thermal noise component. In order to obtain the PRS TOA, the UE aims to estimate the first path delay $\tau^{(0)}$. The majority of the methods employed to estimates $\tau^{(0)}$ rely on the calculation of the cross-correlation between the transmitted and received PRSs. Denote with $r[n] = r(nT_{\text{s}})$ the sampled version of the received signal $r(t)$, with sampling time T_{s}.[2] The cross-correlation $R_{r,s}[n]$ is defined as

$$R_{r,s}[n] = \sum_{j=0}^{N_{\text{samp}}^{\text{PRS}}-1} r[j] s^*[n - j] \tag{4.16}$$

for $n = 0, 1, \ldots, N_{\text{samp}}^{\text{PRS}}$, where $s[n] = s(nT_{\text{s}})$, $(\cdot)^*$ denotes the complex conjugate operator and $N_{\text{samp}}^{\text{PRS}}$ the number of PRS samples. In LOS condition, the delay of the first channel path can be reliably estimated searching for the strongest peak in the cross-correlation. However, in NLOS condition the first channel path (LOS component of the received signal) is usually very weak and the strongest peak in cross-correlation represents late replicas of the transmitted signal, reaching the UE via longest propagation paths, thus introducing a bias in the TOA estimate [34, 149]. In order to mitigate this detrimental effect, TOA can be estimated as the first peak of the modulo of the normalized cross-correlation which exceeds a certain threshold ξ, i.e.,

$$\hat{n} = \underset{n}{\arg\min} \left\{ \bar{R}_{r,s}[n] \geq \xi \right\} \tag{4.17}$$

where

$$\bar{R}_{r,s}[n] = \frac{|R_{r,s}[n]|}{\max\{|R_{r,s}[n]|\}} . \tag{4.18}$$

Then the estimated TOA is calculated as $\hat{\tau} = \hat{n}T_{\text{s}}$. The threshold value ξ greatly impacts the estimate accuracy: if ξ is setted too low the first path may be incorrectly estimated due

---

[2]The sampling time T_{s} is inversely proportional to the bandwidth of the PRS.

to the thermal noise affecting the received signal, while if ξ is setted too high late NLOS paths may be incorrectly estimated as the LOS path. Besides threshold-based methods, iterative methods aiming at estimate the channel impulse response and consequentially the LOS path, can be employed [150]. In each iteration, the strongest peak in $R_{r,s}[n]$ is identified and then its contribute removed. Formally, denote with $R_{r,s}^{(i)}[n]$ the cross-correlation in the i-th iteration. The cross-correlation at iteration $i+1$ is obtained as

$$R_{r,s}^{(i+1)}[n] = R_{r,s}^{(i)}[n] - R_{r,s}^{(i)}[n^{(i)}] R_{s,s}[n - n^{(i)}] \tag{4.19}$$

where $n^{(i)} = \arg\max_n \left\{ R_{r,s}^{(i)}[n] \right\}$ and $R_{s,s}[n]$ is the normalized auto-correlation of the transmitted signal $s(t)$. At the iteration 0, the algorithm is initialized such that $R_{r,s}^{(0)}[n] = R_{r,s}[n]$. The algorithms stops after a N_I number of iterations or when a specific criterion is met, such as the peak-to-average ratio falls below a certain threshold. Among the identified $N_I + 1$ delays, $\{n^{(0)}, n^{(1)}, \ldots, n^{(N_I)}\}$, the minimum is taken as estimated sample delay, i.e.,

$$\hat{n} = \min\{n^{(0)}, n^{(1)}, \ldots, n^{(N_I)}\} . \tag{4.20}$$

In order to increase the accuracy of the TOA estimates multiple PRS occasions can be employed. Cross-correlations obtained from different PRS occasions can be coherently accumulated in order to increase the signal-to-noise ratio (SNR), which leads to more accurate estimates. As a downside, increasing the signal integration level, also increases the latency of the localization systems. Moreover, depending on the UE velocity and the channel delay spread, coherent integration may not be feasible and instead non-coherent integration must be applied, greatly reducing the improvements of the SNR. Hence a trade-off is present in terms of accuracy and localization latency, which are both important key performance indicators for many use cases.

4.5   DL-TDOA-based Localization

In DL-TDOA-based localization, the UE measures the TOA of PRSs transmitted by multiple gNBs. Then, the UE computes the relative differences of the TOAs using the gNB with the best SNR as reference cell. Additional constraints are present in order to ensure a minimum level of accuracy for the TOA measurements: in order to perform TOA measurements with a specific gNB, the SNR must be greater than -13 dB. Among the cells which are eligible for TOA measurement, the reference cell is chosen such that the SNR is the highest, granted it is above -6 dB [151]. These relative signal time differences (RSTDs)

measurements are then quantized and reported to the network together with metrics quantifying the accuracy of these measurements. Based on known positions of gNBs and their relative time synchronization, it is possible for the network to estimate the UE position from the RSTD and accuracy metrics using multilateration. Therefore, the localization accuracy depends on the accuracy of the reported RSTDs.

In order to perform DL-TDOA-based localization, the UE subtracts the TOA obtained from the reference gNB from all the other TOAs in order to obtain the DL-TDOA measurements. Given N_{BS} gNBs the number of DL-TDOA measurements is $N_{\mathrm{BS}} - 1$. The measurements are then transmitted to the core network in order to be processed and used to locate the UE. For each DL-TDOA measurement, a metric representing the measurement accuracy is also transmitted. The use of DL-TDOA measurements instead of TOA measurements as input to the localization algorithms eliminates the need of synchronous time between the UE and the gNBs involved in the localization process. The only synchronization required is among the gNBs, where the time instant at which the different PRSs are transmitted by the gNBs is required. Accurate time synchronization between the gNB is more easily obtainable compared to obtaining a common time reference between the UE and all the gNBs.

Geometrically, given a pair of neighbor and reference gNBs, the DL-TDOAs measurement identifies a hyperboles where the UE might be located and the intersection of different hyperbolas from difference pairs of neighbor and reference gNBs indicates the UE position (see Fig. 4.3). Mathematically , the UE position can be obtained by solving a non-linear system of equations. Without loss of generality, consider the reference gNB as gNB 1 and indicate with

$$\hat{\tau}_{i,1} = \hat{\tau}_i - \hat{\tau}_1 \tag{4.21}$$

the DL-TDOA measurements obtained from the i-th neighbor gNB and the reference gNB 1, where $i = 2, 3, \ldots, N_{\mathrm{BS}}$, $\hat{\tau}_i$ is the TOA estimates relative to the i-th gNB and $i = 2, 3, \ldots, N_{\mathrm{BS}}$. In absence of measurements error, the UE position $\boldsymbol{p} \in \mathbb{R}^2$ could be obtained by solving

$$\begin{cases} c\hat{\tau}_{2,1} & = d_{2,1}(\boldsymbol{p}) \\ c\hat{\tau}_{3,1} & = d_{3,1}(\boldsymbol{p}) \\ \quad\quad \vdots \\ c\hat{\tau}_{N_{\mathrm{BS}},1} & = d_{N_{\mathrm{BS}},1}(\boldsymbol{p}) \end{cases} \tag{4.22}$$

where c is the signal propagation speed and

$$d_{i,j}(\boldsymbol{p}) = d_i(\boldsymbol{p}) - d_j(\boldsymbol{p})$$
$$= \left|\left|\boldsymbol{p} - \boldsymbol{p}_i^{\text{BS}}\right|\right|_2 - \left|\left|\boldsymbol{p} - \boldsymbol{p}_j^{\text{BS}}\right|\right|_2 . \qquad (4.23)$$

In (4.23), $\boldsymbol{p}_i^{\text{BS}}$ represents the coordinates of the i-th gNB and $||\cdot||_2$ represents the 2-norm operator. However, due to the uncertainties affecting the DL-TDOA measurements, an exact solution of (4.22) cannot be obtained and non-linear LS approaches are typically employed to infer the UE position. These LS approaches assume as measurement model

$$\hat{\mathbf{d}} = c\hat{\boldsymbol{\tau}}$$
$$= \boldsymbol{d}(\boldsymbol{p}) + \mathbf{w} \qquad (4.24)$$

where

$$\hat{\boldsymbol{\tau}} = [\hat{\tau}_{2,1}, \hat{\tau}_{3,1}, \ldots, \hat{\tau}_{N_{\text{BS}},1}]^{\text{T}} \qquad (4.25\text{a})$$
$$\boldsymbol{d}(\boldsymbol{p}) = [d_{2,1}(\boldsymbol{p}), d_{3,1}(\boldsymbol{p}), \ldots, d_{N_{\text{BS}},1}(\boldsymbol{p})]^{\text{T}} \qquad (4.25\text{b})$$
$$\mathbf{w} = [\mathsf{w}_{2,1}, \mathsf{w}_{2,1}, \ldots, \mathsf{w}_{N_{\text{BS}},1}]^{\text{T}} \qquad (4.25\text{c})$$

with $\mathbf{w}$ being a zero-mean additive white Gaussian noise (AWGN) vector with covariance matrix $\boldsymbol{\Sigma} = \mathbb{E}\left\{\mathbf{w}\mathbf{w}^{\text{T}}\right\}$. In this setting, given a realization of the measurement $\hat{\boldsymbol{d}}$, the UE estimated position is obtained as

$$\hat{\boldsymbol{p}} = \underset{\tilde{\boldsymbol{p}}}{\text{argmin}}\, \epsilon(\tilde{\boldsymbol{p}}) \qquad (4.26)$$

where the cost function $\epsilon(\tilde{\boldsymbol{p}})$ is given by

$$\epsilon(\tilde{\boldsymbol{p}}) = (\hat{\boldsymbol{d}} - \boldsymbol{d}(\tilde{\boldsymbol{p}}))^{\text{T}} \boldsymbol{\Sigma}^{-1}(\hat{\boldsymbol{d}} - \boldsymbol{d}(\tilde{\boldsymbol{p}})) . \qquad (4.27)$$

No closed form solution exists for the LS problem and many iterative approaches have been proposed for obtaining an approximate solution. Among those, we illustrate the Levenberg-Marquardt which is an gradient-based iterative method with good properties of fast convergence and robustness against inaccurate initialization points [152]. Denote with $\hat{\boldsymbol{p}}^{(i)}$ the solution at the iteration i, the solution at the step $i+1$ is obtained as

$$\hat{\boldsymbol{p}}^{(i+1)} = \hat{\boldsymbol{p}}^{(i)} + (\Phi(\hat{\boldsymbol{p}}^{(i)})^{\text{T}} \boldsymbol{\Sigma}^{-1} \Phi(\hat{\boldsymbol{p}}^{(i)}) + \lambda^{(i)} \boldsymbol{I}_2)^{-1} \times$$
$$\times (\Phi(\hat{\boldsymbol{p}}^{(i)})^{\text{T}} \boldsymbol{\Sigma}^{-1}(\hat{\boldsymbol{d}} - \boldsymbol{d}(\hat{\boldsymbol{p}}^{(i)}))) \qquad (4.28)$$
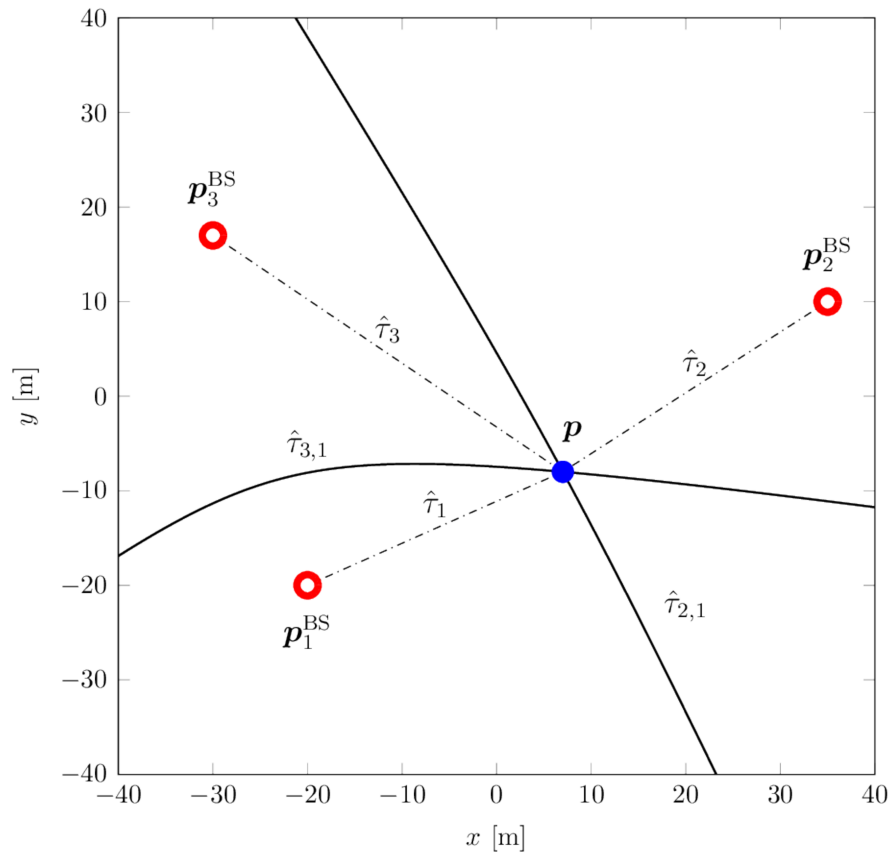
Figure 4.3: DL-TDOA based localization with $N_{\mathrm{BS}} = 3$ gNBs (red annolous) and one UE (filled blue circle). The reference gNB is indexed by $i = 1$.

where $\Phi(\boldsymbol{p}) = \nabla_{\boldsymbol{p}}^{\mathrm{T}} \otimes \boldsymbol{d}(\boldsymbol{p})$, $\nabla_{\boldsymbol{p}} = [\partial/\partial x, \partial/\partial y]^{\mathrm{T}}$, $\boldsymbol{A} \otimes \boldsymbol{B}$ represents the Kronecker product between the matrices $\boldsymbol{A}$ and $\boldsymbol{B}$, and $\lambda^{(i)}$ is a regularization parameter for matrix inversion. The algorithms stops when the distance between $\widehat{\boldsymbol{p}}^{(i+1)}$ and $\widehat{\boldsymbol{p}}^{(i)}$ falls below a given threshold.

Table 4.2: Main Quantities and their Significance.

Quantity	Significance
μ	numerology
p	antenna port index
k	SC index
l	symbol index
m	generic sequence index
n_{f}	frame index
$n_{\text{s,f}}^{\mu}$	slot index within a frame, given the numerology μ
$N_{\text{slot}}^{\text{frame},\mu}$	number of slots per frame, given the numerology μ
$N_{\text{symb}}^{\text{slot}}$	number of symbols per slot
$c_{\text{init}}^{\text{PRS}}$	seed used for initializing the PRS sequence
$n_{\text{ID,seq}}^{\text{PRS}}$	PRS sequence ID, used to calculate $c_{\text{init}}^{\text{PRS}}$
β_{PRS}	PRS scale coefficient
$K_{\text{comb}}^{\text{PRS}}$	PRS comb size
$k_{\text{offset}}^{\text{PRS}}$	SC offset for PRS transmission
k'	symbol dependent SC offset for PRS transmission
$l_{\text{start}}^{\text{PRS}}$	starting symbol index for PRS transmission within a slot
L_{PRS}	number of allocated symbols for PRS transmission within a slot
$T_{\text{per}}^{\text{PRS}}$	periodicity of the PRS resource in slot indexes
$T_{\text{rep}}^{\text{PRS}}$	repetition of the PRS resource for a single instance of the PRS resource set in slot indexes
$T_{\text{gap}}^{\text{PRS}}$	gap between the repetition PRS resource for a single instance of the PRS resource set in slot indexes
$T_{\text{offset,res}}^{\text{PRS}}$	slot offset with respect to the initial slot of the frame allocated for the PRS resource set
$T_{\text{offset}}^{\text{PRS}}$	slot offset with respect to $T_{\text{offset,res}}^{\text{PRS}}$ for the PRS resource
$N_{\text{RB}}^{\text{PRS}}$	number of RB allocated for the PRS transmission

Chapter 5

SI Approach for 5G and B5G Networks

The positional information of network nodes is inherently encapsulated in SI [55], which is related to various types of positional features (e.g., distance, angle, and proximity) extracted from measurements and of contextual data (e.g., dynamic model, digital map, and user profile) corresponding to the environment. It is therefore essential to develop localization techniques which are capable of accounting for all the SI present in a B5G ecosystem. Indeed, accurate location awareness depends on the capability to extract and exploit SI, both of which can be challenging in complex wireless environments.

Localization accuracy of SVE-based methods depends heavily on the quality of the SVEs, which deteriorates in complex wireless environments. In particular, the performance of conventional techniques degrades in wireless environments due to biases in SVEs caused by NLOS conditions and multipath propagation. This challenges both the reliability of LBSs and the efficiency of network management. To cope with impairments of wireless environment, conventional approaches have focused on improving the estimation of single values by modeling SVE errors [34], selecting measurements [37], and using hybrid models for data fusion [153]. To improve location awareness, the SI-based approach has been recently proposed [55]. It enables full exploitation of the positional information inherent in different types of measurements together with contextual data. The full exploitation of the positional information requires efficient fusion algorithms for measurements and data gathered from heterogeneous sensors, management strategies for networks consisting of nodes with stringent resource limitations, and communication strategies that can cope with the dimensionality of the SI. In order to improve the localization accuracy and reduce the communication overhead in 5G and B5G networks, it is vital to develop efficient methods for learning generative models that accurately characterize the wireless

environment and innovative methods for reducing the dimensionality of SI while capturing essential positional information.

5.1 Beyond 5G technologies

A new paradigm that is foreseen to play a key role in B5G networks is the integrated sensing and communication, i.e., the exploitation of the same signal for both sensing the environment and communicating information (e.g., radar and communication for autonomous vehicles). This calls for research on waveform design, interference mitigation, spectrum sharing, time sharing, and hardware reuse between sensing, localization, and communication. Joint sensing and communication can also be used in a passive radar setting for the detection and localization of device-free targets. Following an alternative solution, the signals used for sensing of UE or even device-free targets can be either explicitly designed and transmitted for this task or already present in the environment for other purposes (signals of opportunity) and these can include cellular signals. This setting leverages both base stations and access points as illuminators of opportunity, without deploying any dedicated wireless source, relying on any target device, and incurring additional costs. The signals propagate in the monitored environment and are reflected by both background objects (clutter) and target objects [65]. The sensing devices can be 5G standard devices or they might be augmented to monitor other technologies. Sensing and localization in this case can be performed by a network of receivers (specific sensors or UEs) that are deployed in a designated area to receive the signals emitted by base stations or by other sources of opportunity and reflected by the passive targets.

Recently, research efforts have been devoted to resiliency and robustness of localization systems in harsh electromagnetic environments affected by severe impairments such as multipath and NLOS conditions. In such environments, the use of intelligent surfaces (ISs) promises to mitigate these impairments by controlling the electromagnetic environment [154]. Therefore, ISs can be employed to create desirable wireless propagation conditions that improve the performance of localization systems in B5G networks. In addition, the use of terahertz bands is envisioned as a key wireless technology to satisfy the demand of extremely high throughput and can be utilized for localization in environments such as those of B5G for Industry 4.0 [155].

5.2 SI for Location Awareness

Localization aims to determine the positional states of network nodes. At a given time, the positional state of a node includes its position (absolute or relative coordinates) and other mobility-related quantities (e.g., velocity, acceleration, and orientation). Localization methods infer the positional states of the nodes based on inter-node and intra-node measurements, and on contextual data.

Location awareness is the knowledge of probabilistic information on possible UEs' positional states. Such information is described by the conditional posterior of the positional state, which can serve to (i) infer the positional state of each UE; and (ii) enable applications where probabilistic information of the positional state is sufficient. The location awareness for the UEs at different time instants can be obtained based on inter-node measurements with respect to both base stations and neighboring UEs (cooperation with other UEs via side links), intra-node measurements, and contextual data. Most location aware services, including those relying on 5G and B5G networks, require to infer sequences of positional states. The joint posterior distribution of positional states can be determined via a *prediction step* (using a dynamic model) followed by an *update step* (using an observation model and a new measurement).

Location awareness can be obtained from SI, which is composed of SFI and SCI as described in Chapter 3 [55]. SI-based approach provides a statistical characterization of the relation between position-related measurement and a positional feature. Therefore, even measurements affected by severe multipath or NLOS conditions can be used by SI-based localization since SI relies on probabilistic models which have already accounted for such situations. Compared to existing works which rely on predefined measurement models, such as those in the field of multi-sensor multi-target tracking [156], SI-based approaches do not require specific measurement models. This can be especially useful if the measurement models for the wireless environment are not available or if the data volume of the measurements prohibits the direct use of likelihood functions.

5.3 Distributed Implementation

In 5G and B5G networks, it is important to infer positional states in a distributed manner. In noncooperative scenarios, each UE can determine its own position, resulting in a distributed implementation. However, it is known that spatiotemporal cooperation can significantly improve localization accuracy. Unfortunately, a distributed implementation of cooperative methods is hindered by information coupling, i.e. the UE positional state inferences are highly interrelated. Therefore, the optimal implementation of cooperative

approaches requires a centralized implementation to determine the joint posterior distribution of all UEs.

Distributed techniques for cooperative localization in B5G networks are expected to rely on the approximation of marginal distributions. For instance, loopy belief propagation techniques approximate the marginal posterior of each agent by disregarding the cycles in the graph describing the network connectivity [157]. Such approximations can be obtained from graphs that describe the network connectivity after disregarding cycles. Hence, each node keeps track of its own positional estimate and uncertainty, and individual estimates and uncertainties are updated by means of message passing among different processing nodes.

5.4   Data Fusion in Heterogenous Networks

The development of 5G and B5G networks leverages an ecosystem comprised of heterogeneous technologies. Therefore, it is essential to exploit diverse types of measurements. The SI-based approach naturally and efficiently fuses heterogeneous measurements from multimodal sensors. Fusion of such measurements can be implemented by multiplying SFIs corresponding to different measurements, as long as the random measurement data are conditionally independent given the positional states [55].

The conditional independence of the observations adequately represents the behavior of actual measurements obtained by sensors that are spatially scattered or by sensors belonging to different technologies. Examples of multimodal measurements are those associated with different types of amplitude-, time-, and angle-related features from wireless technologies operating with different modulations and frequency bands [153].

5.5   Case Study

In this section will be presented how SI can be used in the context of 5G localization. In particular, given the already standardized architecture and protocols for 5G localization, we propose a simple way to exploit the strengths of SI-based approach without the need of a complete redesign. In order to accomplish this, we will discuss the application of SI on RAT-dependent measurements supported by the standard as per Release 16. In particular, we will focus on the generation of SRI based on DL-TDOA measurements.

Recall that the DL-TDOA measurements relative to the i-th gNB is given by (4.21) where gNB 1 is taken as reference. SRI can be obtained considering as measurement vector the single TDOA measurement, i.e., $\boldsymbol{y}_i = \hat{\tau}_{i,1}$, and as positional feature the distance
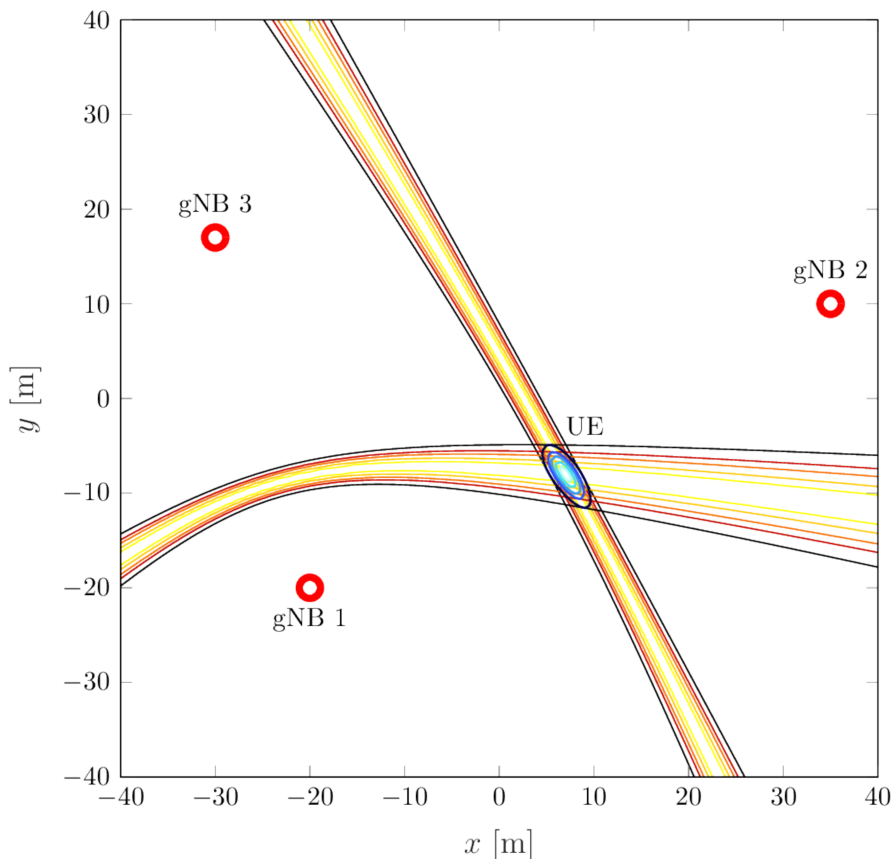
Figure 5.1: SRI based on DL-TDOA measurements $N_{\text{BS}} = 3$ gNBs (red annolous). The reference gNB is indexed by $i = 1$. Intensity of SRI is shown with a red-yellow colormap. The multiplication of the SRI provided by the two pairs of gNB is shown with a blue colormap.

difference, i.e., $\boldsymbol{\theta}_i = d_{i,1}(\boldsymbol{p})$, for $i = 2, 3, \ldots, N_{\text{BS}}$. With this assumptions, the SRI can be written as $\mathcal{L}_{\boldsymbol{y}_i}(\boldsymbol{\theta}_i) = \mathcal{L}_{\hat{\tau}_{i,1}}(d_{i,1}(\boldsymbol{p}))$. In Fig. 5.1 is depicted a pictorial representation of the SRI extracted from DL-TDOA measurements (relative to the gNBs 1 and 2, considering gNB 0 as reference). Intensity of SRI is shown with a red-yellow colormap. The total SFI obtained as multiplication of the SRI provided by the two pairs of gNB is shown with a blue colormap. The particular gNB used as reference does not affect the SRI as long as the statistical relation between $\hat{\tau}_{i,1}$ and $d_{i,1}$ does not depend on the specific pair of gNBs involved. With this setup, the use of SI-based techniques is completely transparent to the UE. At the UE side, the SI-based localization process is identical to the SVE-based, and all the processing, including the evaluation of the generative model and the search of the maximum, is carried out at the network side.

Given the heterogeneity and complexity of the environments where the localization functionalities of 5G wireless networks will be exploited, in order to achieve the best performance, the generative model used to determine the SRI should be inferred from real data acquired by a measurement campaign carried out in the area of interest. In particular,
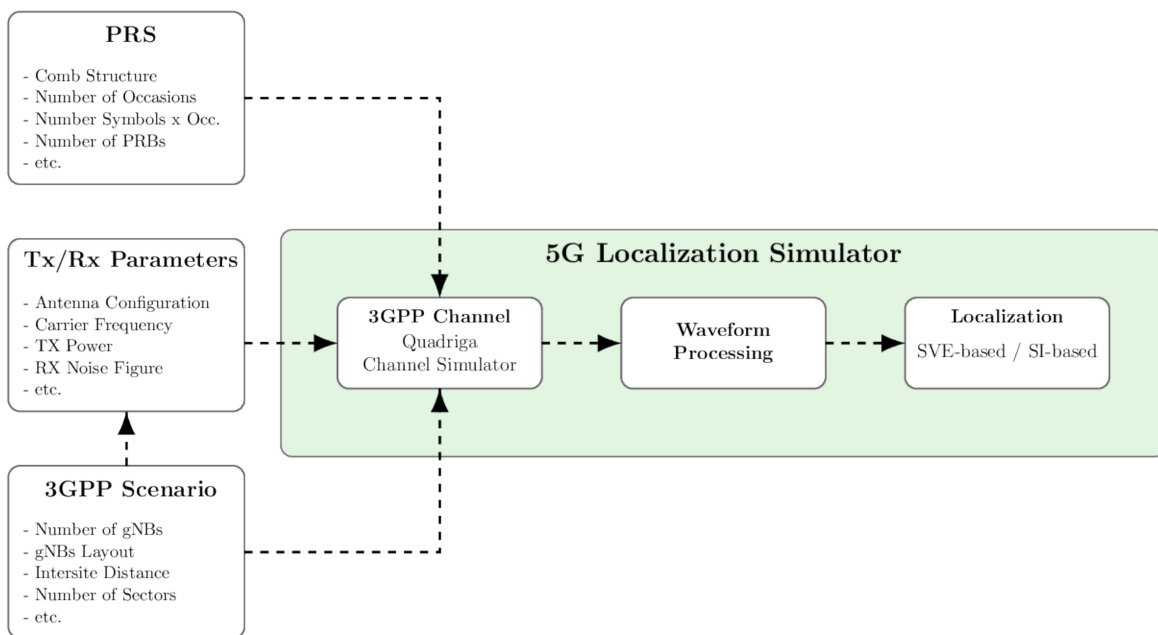
Figure 5.2: Diagram representing the general structure of the 5G localization simulator.

the training data $\{\boldsymbol{x}_l\}_{l \in \mathcal{N}_{\mathrm{T}}}$ are composed by $\boldsymbol{x}_l = [(\hat{\tau}_{i,1})_l, (d_{i,1}(\boldsymbol{p}))_l]^{\mathrm{T}}$, where dimensionality reduction techniques are not required.[1] Modeling the UE position as an unknown deterministic parameter, once an estimate of the the generative model $\hat{f}(\hat{\tau}_{i,1}; d_{i,1}(\boldsymbol{p}))$ is obtained, given a new set of DL-TDOA measurements $\{\hat{\tau}_{i,1}^{\mathrm{new}}\}_{i=2}^{N_{\mathrm{BS}}}$, the UE position can be inferred as

$$
\begin{aligned}
\hat{\boldsymbol{p}} &= \arg\max_{\boldsymbol{p}} \prod_{i=2}^{N_{\mathrm{BS}}} \mathcal{L}_{\hat{\tau}_{i,1}^{\mathrm{new}}}(d_{i,1}(\boldsymbol{p})) \\
&= \arg\max_{\boldsymbol{p}} \prod_{i=2}^{N_{\mathrm{BS}}} \hat{f}(\hat{\tau}_{i,1}^{\mathrm{new}}; d_{i,1}(\boldsymbol{p})).
\end{aligned} \tag{5.1}
$$

Similarly to the SVE-based localization technique presented in Chapter 4, (5.1) involves an exhaustive search of the maximum to infer the UE position. In order to avoid the increase in the computational burden and latency of the localization system, different strategies can be employed. Given a discretized version of the monitored area, the UE position can be inferred iteratively by performing the search of the maximum in progressively finer grids.

---

[1]Note that the gNB 1 is considered as reference gNB relative to the TDOA measurements and distance difference for all the training data. This is done with the only purpose to maintain a clear notation. Measurements with different reference gNB can be used to estimate the generative model.

Table 5.1: Main features of the 5G simulator.

Parameter	Value			
Scenario	IOO		UMi	
Carrier Frequency	2 GHz	4 GHz	2 GHz	4 GHz
SC Spacing	15 kHz	30 kHz	15 kHz	30 kHz
Bandwidth	50 MHz	100 MHz	50 MHz	100 MHz
Area	120 m × 50 m		500 m × 500 m	
Number of Sites	12		19	
Number of Sectors	1		3	
Intersite Distance	20 m		200 m	
gNB TX Power	24 dBm		44 dBm	
gNB N. Ant. El.	8 (2 polarizations, 4 per polarization)			
gNB Ant. El. Rad. Pattern	Technical Report 38.855 [30]			
gNB Ant. Height	3 m		10 m	
UE Ant. El. Rad. Pattern	Isotropic			
UE Ant. Height	1.5 m			
Channel Model	Technical Report 38.901 [158]			
Signal	PRS [146, 148]			

5.5.1   5G Localization Simulator

The results are obtained using the 5G localization simulator and developed for testing conventional SVE-based and SI-based algorithms. Fig. 5.2 reports a diagram representing the general structure of the simulator with its main components and parameters. The simulator developed follows closely the specifications reported in [30], the 3GPP technical report (TR) on 5G positioning. The simulator purpose is twofold: i) to provides baseline performance for the state-of-the-art algorithms currently employed in cellular localization systems; and ii) provides a standardized platform for testing advanced SI-based localization algorithms which have been developed.

The simulator is capable of demonstrating 5G localization systems operating in the following scenarios: i) UMi; and ii) IOO. In each scenario, different channel models, number of sites, spatial displacement of the site, inter-site distance, and number of sectors per site (i.e., number of gNB per site) are considered. The channel is compliant with [158]
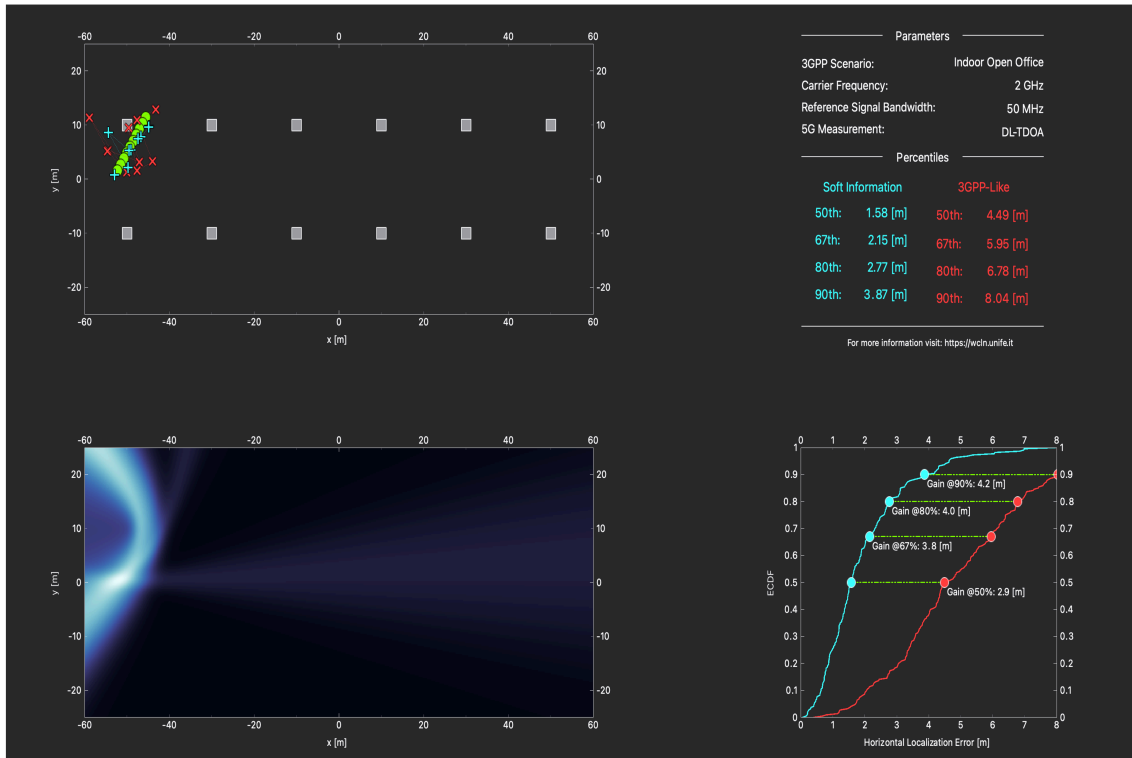
Figure 5.3: Screenshot of the graphic user interface showing localization via SVE and SI. In the picture, 5G localization based on DL-TDOA measurements is considered for IOO scenario.

and it is simulated using the Quadriga channel simulator [159, 160], which allows for spatially correlated large scale fading parameters. In Tab. 5.1 are summarized the major simulation parameters for the two standardized scenarios.

Regardless of the scenario considered, [30] specifies different carrier frequency and numerologies for 5G localization. In particular, for frequency range 1 (FR1), i.e., center frequency below 7.15 GHz [161], are considered as representative the carrier frequencies of 2 GHz and 4 GHz, with numerologies 0 and 1 (15 kHz and 30 kHz of subcarrier spacing), respectively. Given the scenario and carrier frequency, different antenna arrays for UEs and gNBs, receiver noise figure, and transmitted power are specified [30,146,148,161–163]. gNBs antenna array configurations are taken from [164], and perfect synchronization and ideal muting (i.e., no interference from neighbour gNBs) are considered for the simulations. The simulator is capable of simulating a 5G localization systems based on DL-TDOA measurements obtained exploiting the PRS in FR1. The PRS simulated is fully compliant with the specifications contained in [146,148] including allocation in the frequency domain (i.e., comb structure), number of RBs, number of symbols per occasions, and periodicity of the occasions, as described in Sec. 4.3.

41

Graphic user interface

In addition, a software based on the simulator outputs has been developed for showcasing the localization estimates obtained via both SVE-based and SI-based approaches. In particular, the software can be divided in three main components:

1. **5G Measurements Generator**: Measurement vectors are obtained via the simulator presented in Sec. 5.5.1. The simulator can simulate measurements relative to UEs random positions and UEs moving over random trajectories. This allows to obtain significative dataset for generative model training and validation, respectively. Then, the simulated measurements are processed by the localization engine.

2. **Localization Engine**: SI-based localization algorithms are implemented via a two steps procedure. First, in a training phase (offline) the generative model is estimated based on datasets composed of measurements and UEs positional features obtained from the 5G simulator. In the online phase, real-time SI-based localization is accomplished based on the generative model previously estimated and the positional features of UEs moving over random trajectories.

3. **Graphic Interface**: A graphic user interface which allows the user to experiment the effect on the localization algorithms using DL-TDOA measurements with different operating conditions. In particular it is possible to select:

   - scenario (UMi and IOO);
   - carrier frequency (2 GHz, and 4 GHz); and
   - PRS bandwidth (50 MHz and 100 MHz).

   The possible configurations reflects the 3GPP setting defined in the TRs for UMi and IOO scenarios. The graphic user interface shows the comparison between SI-based and SVE-based localization via trajectories plot and the empirical comulative density function (ECDF) for the horizontal localization error.

Fig. 5.3 shows a screenshot of the graphic user interface for 5G localization based on DL-TDOA measurements. In the graphic user interface, four main areas can be identified: i) the top-left box shows environment with the real UE position, estimated position via SVE-based approach, and estimated position via SI-based approach; ii) the top-right box reports the main simulation parameters and a summary of the performance of the two localization approaches; iii) the bottom-right box shows a graphic representation of the SI for the current location estimate; and iv) the bottom-left box reports the ECDF for the horizontal localization error for both localization approaches.

5.5.2 DL-TDOA Measurements

This section presents results on localization accuracy, in terms of the ECDF of the horizontal localization error, based on 3GPP standard. In particular, the performance obtained with the SI-based approach is compared with that reported in the 3GPP TR [30]. The position root-mean-square error (RMSE) is also presented for different generative models of the SI and cardinalities of the trial data.

Two 5G standardized scenarios are considered, namely UMi and IOO. The UMi scenario exhibits a lower probability of LOS links and a higher delay spread, while the IOO scenario is characterized by higher probability of LOS links and lower delay spread. In both cases, we account for the spatial consistency of the wireless channel. For the UMi scenario, a 550 meters by 550 meters area is considered with 19 sites; each site includes three gNBs, each covering an angular sector of 120 degrees and emitting at a power level of 43 dBm. For the IOO scenario, a 120 meters by 50 meters area is considered with twelve single-sector gNBs emitting at a power level of 24 dBm. For both scenarios, the UEs are randomly deployed within the monitored area and the noise figure at the receiver side is of 5 dB. Fig. 5.4 shows LOS maps and gNBs spatial displacement for the UMi (top) and IOO (bottom) standardized scenarios. In particular, the figure shows instantiations of UE positions in which a UE would be in LOS with zero (white), one (blue), two (green), and at least three (orange) gNBs. Fig. 5.5 shows the empirical probability of the number of gNBs and sites in LOS given a uniformly randomly deployed UE for the IOO and UMi scenarios, respectively.

TDOA measurements obtained from the PRS are considered with two combinations of bandwidth and carrier frequency: (i) 50 MHz bandwidth at 2 GHz, namely Type I simulation setting; and (ii) 100 MHz bandwidth at 4 GHz, namely Type II simulation setting. According to [30], the gNBs are synchronized. The channel instantiations are generated using the QuaDRiGa channel simulator, which supports 3GPP standardized channel models and accounts for spatially-correlated large and small scale fading [158].

The generative model for SI is based on Fisher–Wald settings, considering a GMM with three mixtures, i.e., $N_{\text{GM}} = 3$ in (3.10). The UE location is inferred by maximizing such a GMM. The off-line and on-line phases employ a 10-fold cross-validation technique for each of the standardized settings. In particular, 1000 instantiations of large and small scale fading are generated and, for each instantiation, 10 UEs are randomly deployed within the monitored area and position inference is performed. At each iteration of the cross-validation procedure, the TDOA-related measurements and positional feature obtained from 900 instantiations of the 10 UEs are used to train the generative model, while 100 instantiations of the 10 UEs are used for position inference. In the on-line phase, the
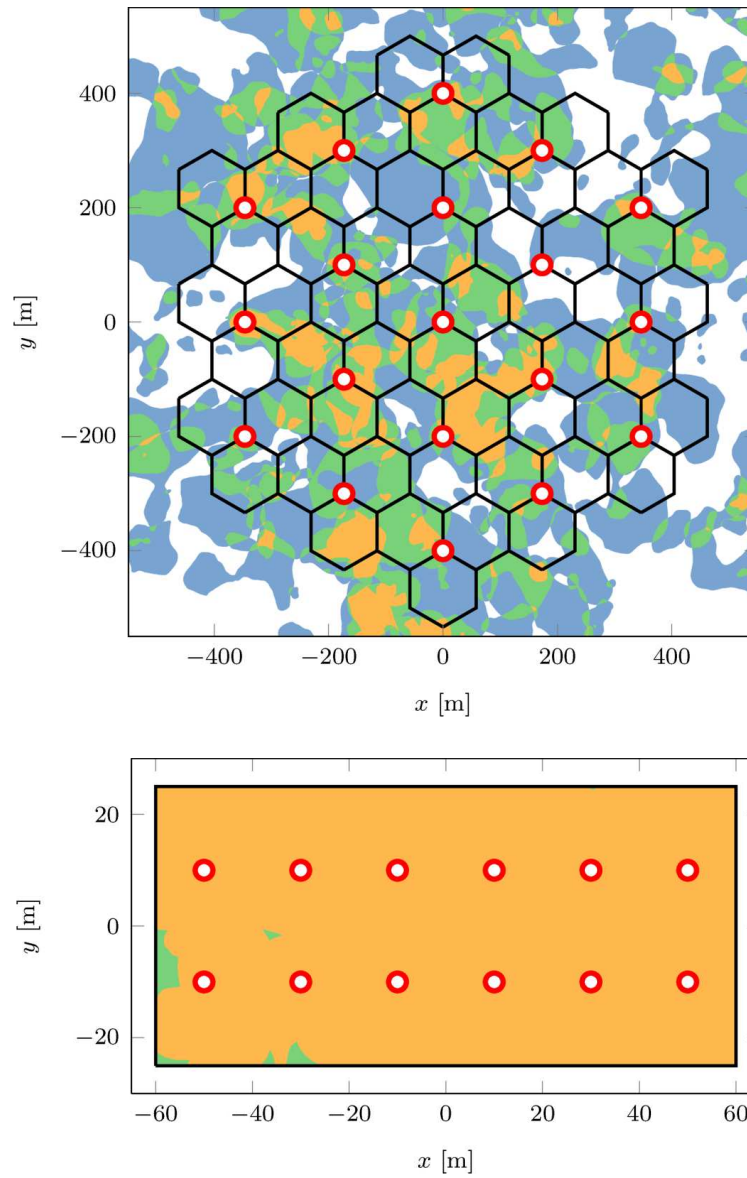
Figure 5.4: Example of LOS map for 3GPP urban micro (top) and indoor open office (bottom) scenarios where red circles represent the gNBs. White, blue, green, and orange areas correspond to positions with no gNBs, one gNB, two gNBs, and at least three gNBs in LOS, respectively.
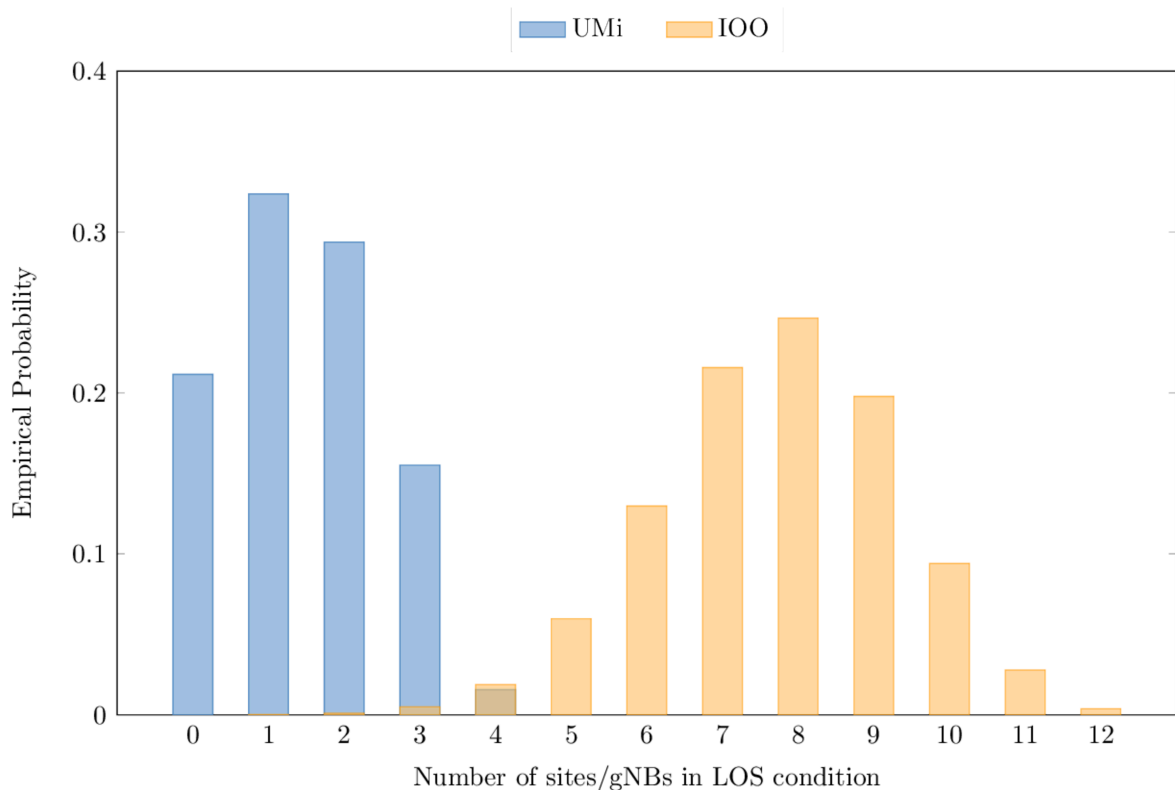
Figure 5.5: Empirical probability of the number of sites/gNBs in LOS given an instantiation of the UE position.

maximum of the GMM is obtained via an exhaustive search. A coarse position estimate is first obtained by searching over the entire area with a grid of 5 meters per step. A fine position estimate is then obtained by searching over a 30 meters by 30 meters area centered on the coarse estimate with a grid of 0.5 meters per step.

Fig. 5.6 shows the ECDF of the horizontal localization error for UMi scenarios with simulation settings Type I and Type II. Blue crosses and red asterisks represent the tabulated results from TR [30], used for comparison in Type I and Type II simulation settings, respectively. Blue dashed line with triangle markers and the red solid line with square markers represent the results for SI-based localization in Type I and Type II simulation settings, respectively. It can be observed that the SI-based approach provides significant performance improvements across all the percentiles compared to the results reported in [30]. In particular, for Type I simulation settings the SI-based approach improves the localization accuracy by approximatively 2 to 3 meters compared to the results reported in [30]. For the Type II simulation settings, the performance gain offered by the SI-based approach is even more remarkable; at the 90-th percentile, the SI-based approach improves the localization accuracy by approximatively 5 meters compared to the results in [30]. This can be attributed to the fact that an SI-based approach is more
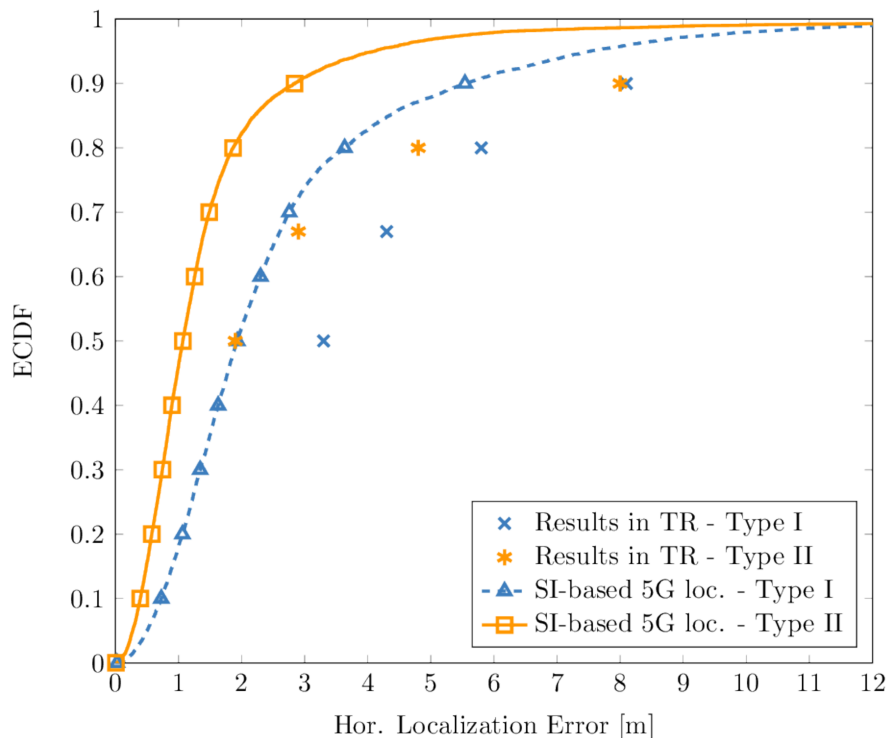
45

Figure 5.6: ECDF of the horizontal localization error for the 3GPP UMi scenario using PRS with 50 and 100 MHz bandwidths at 2 GHz and 4 GHz center frequencies, respectively. The performance of SI-based localization is compared with that reported in TR [30].

robust compared to a classical SVE-approach and, thus, is best suited for challenging wireless propagation environments.

Fig. 5.7 shows the ECDF of the horizontal localization error for IOO scenario with simulation settings Type I and Type II. Blue crosses and red asterisks represent the tabulated results from TR [30], used for comparison for Type I and Type II simulation settings, respectively. Blue dashed line with triangle markers and the red solid line with square markers represent the results for SI-based localization for Type I and Type II simulation settings, respectively. Similarly to the results obtained in the UMi scenario, it can be observed that SI-based approach provides significant performance improvements across all the percentiles compared to the results reported in [30]. In particular, for Type I simulation settings at the 90-th percentile the SI-based approach provides approximatively 6.5 meters of improvement in terms of horizontal localization accuracy compared to [30]. For Type II simulation setting, the performance offered by the SI-based approach is improved by approximatively 4 meters compared to the results in [30]. This can be attributed to the fact that SI-based approach can better exploit the positional information inherent in the measurements via generative models learned from the environment.

Fig. 5.8 shows the position RMSE as a function of the number of mixtures used in the generative model for all scenarios and settings. It can be observed that a mixture
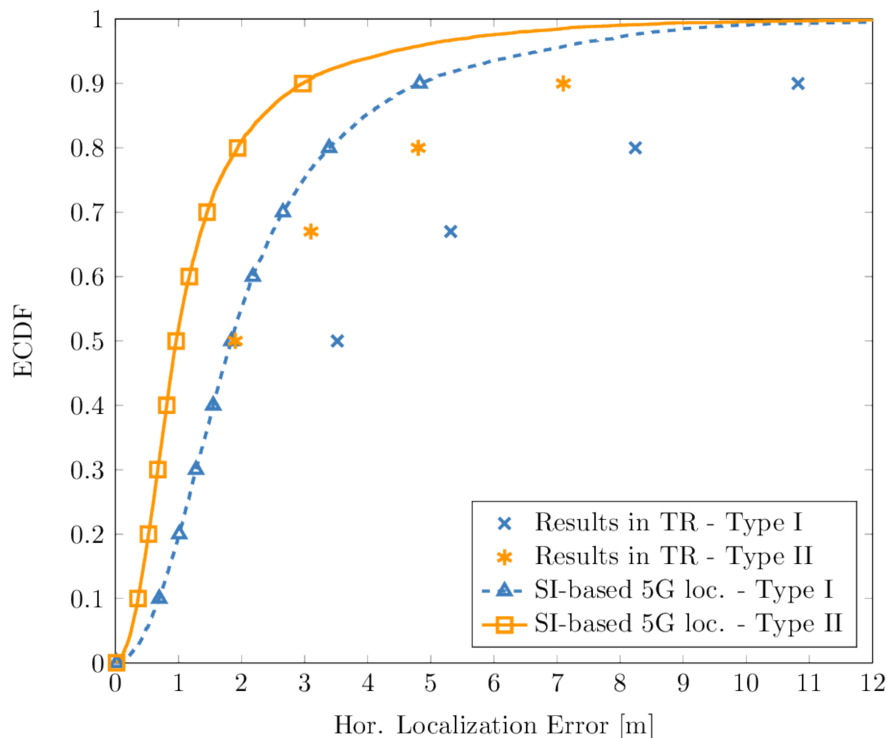
Figure 5.7: ECDF of the horizontal localization error for the 3GPP IOO scenario using PRS with 50 and 100 MHz bandwidths at 2 GHz and 4 GHz center frequencies, respectively. The performance of SI-based localization is compared with that reported in TR [30].

cardinality of three and two already provides a RMSE close to the best possible one for UMi and IOO scenarios, respectively. Tab. 5.2 shows the position RMSE for different numbers of UE measurements used at each iteration of the cross-validation procedure in training the generative model, for both UMi and IOO scenarios with Type I and Type II settings. It can be observed that RMSE already approaches its best possible value with 50 or 500 training measurements, depending on the considered scenario and setting. This shows that the SI-based approach can perform well even with a small number of training measurements.

The performance gain demonstrated in these results reveals that the SI-based approach is crucial for localization in 3GPP standardized scenarios. Such localization accuracy can be exploited for enabling LBSs and improving network management.

5.5.3 Data Fusion

This section will focus on SFI that can be extracted directly from RAT-dependent and RAT-independent observations. In particular, DL-TDOA measurements $\hat{\tau}_{i,1}$ and range estimates $\hat{r}$ based on Wi-Fi TOF measurements are considered.

For DL-TDOA measurements in 5G networks, the SFI is given by $\mathcal{L}_{\hat{\tau}_{i,1}}(d_{i,1}(\boldsymbol{p}))$ and it is
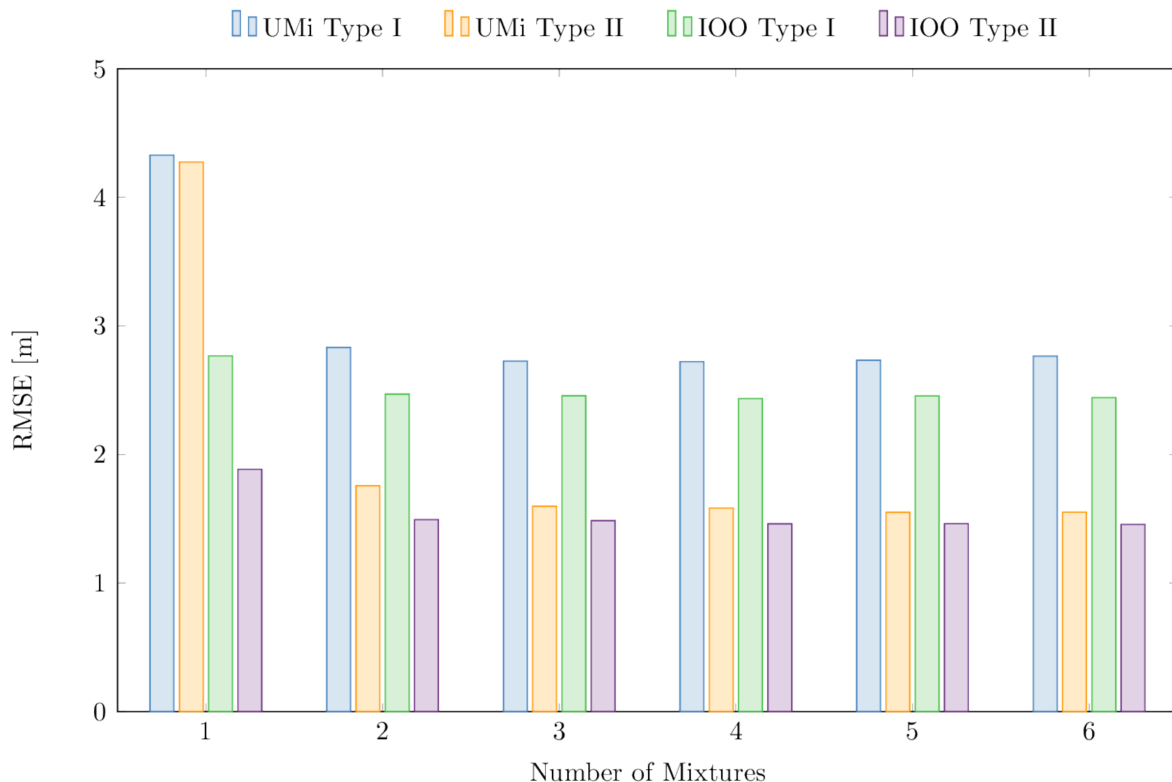
47

Figure 5.8: RMSE of the position estimate as a function of the number of mixtures in the GMM for 3GPP UMi and IOO scenarios using PRS with 50 and 100 MHz bandwidths at 2 GHz and 4 GHz center frequencies, respectively.

referred to as SRI [54,55] as the feature vector is related to the distance. Similarly, SRI for Wi-Fi range measurements is given by $\mathcal{L}_{\hat{r}}(d(\boldsymbol{p}))$, where $\hat{r}$ and $d(\boldsymbol{p})$ represent the estimated range and true distance between the UE and Wi-Fi access point (AP), respectively. The characterization of the relation between the measurement vector and feature vector via a probabilistic model provides a richer information compared to SVE and an efficient way to fuse heterogeneous measurements. In particular, as long as measurement vectors obtained from different technologies can be considered statistically independent given the UE position, thus the resulting SFI can be obtained via simple multiplication of individual SFIs.[2] For hybrid localization in 5G ecosystem, consider a 5G network composed of N_{BS} gNBs and a UE measuring DL-TDOAs as in (4.21). In addition to performing measurements with 5G gNBs, the UE is able to acquire TOF measurements from N_{AP} Wi-Fi APs deployed in the same monitored environment. Thus, the UE position can be

---

[2]RAT-dependent and RAT-independent observations can be reasonably assumed statistically independent given the UE position regardless of the specific technology.

Table 5.2: Position RMSE as a function of the number of UE measurements used in each training phase.

Number of UE training measurements	RMSE [m]			
	UMi Type I	UMi Type II	IOO Type I	IOO Type II
5	3.22	2.07	2.75	1.95
50	2.71	1.62	2.50	1.48
500	2.71	1.59	2.45	1.48
5000	2.72	1.61	2.46	1.48
9000	2.72	1.60	2.46	1.48

efficiently estimated via SI-based approach as

$$\hat{\boldsymbol{p}} = \arg\max_{\boldsymbol{p}} \left\{ \prod_{i=2}^{N_{\mathrm{BS}}} \mathcal{L}_{\hat{\tau}_{i,1}}(d_{i,1}(\boldsymbol{p})) \prod_{n=1}^{N_{\mathrm{AP}}} \mathcal{L}_{\hat{r}_n}(d_n(\boldsymbol{p})) \right\} . \tag{5.2}$$

In Fig. 5.9 is depicted a pictorial representation of the SRI extracted from DL-TDOA and TOF measurements. Intensity of SRI is shown with a red-yellow and green colormaps for DL-TDOA and TOF measurements, respectively. The total SFI obtained as multiplication of the two is shown with a blue colormap.

Consider an IOO area of 120 meters by 50 meters according to [30] in which a varying number of UEs are randomly located and where $N_{\mathrm{BS}} = 12$ 5G gNBs and $N_{\mathrm{AP}} = 6$ Wi-Fi APs are deployed as in Fig. 5.10. In such a scenario, results in terms of ECDF of the horizontal localization error for hybrid localization in 5G ecosystem are presented. In particular, the performance of SVE-based methods for individual 5G and Wi-Fi measurements, SI-based methods for individual 5G and Wi-Fi measurements, as well as results fusing of such measurements via SI framework, are compared.

For 5G network, DL-TDOA measurements obtained considering the same simulation assumption as in Sec. 5.5.2. On the other hand, Wi-Fi related measurements consist of range estimates for the distance between the UEs and the APs. The range estimates are obtained considering the true distance between the UE and AP plus a range estimation error. Such range estimation error is modeled according to the experimental results in [165] which are based on TOF measurements. The measurements are obtained using off-the-shelf components operating on a fixed channel of the 2.4 GHz ISM band and running a 802.11 b/g custom firmware. In particular, the measurements gathered in the scenario referred to as Testbed I in [165] are used to generate range errors for the AP-UEs distances. Testbed I in [165] presents similar characteristics in terms of dimensions and mix of line-of-sight and non line-of-sight conditions with the considered IOO scenario. The fitting
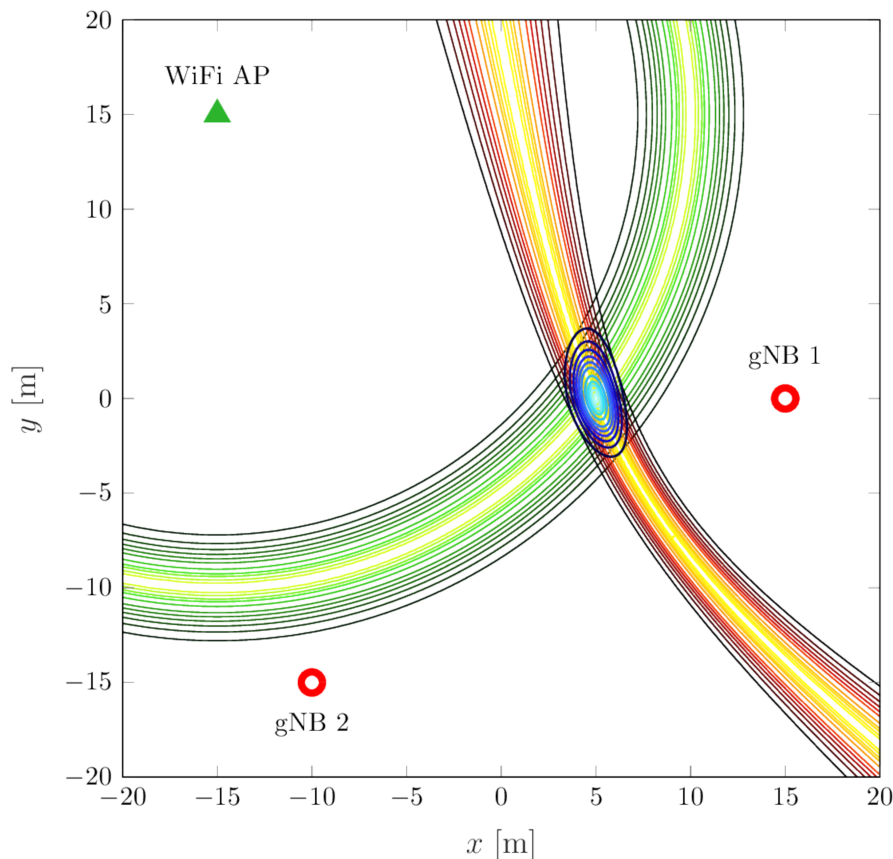
Figure 5.9: Fusion of the SRI based on DL-TDOA measurement. Intensity of SRI based on DL-TDOA measurement is shown with a red-yellow colormap. Intensity of SRI based on TOF measurement is shown with a green colormap. The total SFI obtained as multiplication of the SRI provided by DL-TDOA and TOF measurements is shown with a blue colormap.

distribution is chosen as a Gamma distribution with parameters $\alpha = 1.1$ and $\beta = 3.35$.[3] The ranging based on TOF measurements presents a median error of 2.4 meters and an 80-percentile error of 5.3 meters.

For SVE-based approach, LS algorithm is employed to infer the UE location based on 5G DL-TDOA measurements and Wi-Fi range measurements [152]. LS algorithm represents a good baseline to perform performance comparison as reported in 3GPP technical report [30]. For SI-based approach, the DL-TDOA measurements and distance differences are considered as measurement vector and feature vector for 5G technology, respectively, while range estimates based on TOF measurements and distances are considered as measurement and feature vector for Wi-Fi technology. A GMM as in (3.10) with $N_{\mathrm{GM}} = 5$ mixture components is used as generative model for both DL-TDOA and ranging measurements. The model is validated, i.e., GMM parameters are learned and the localization performance evaluated, via a 10-fold cross-validation procedure [166], over 1000 different

---

[3]A Gamma distribution with shape parameter α and scale parameter β for a random variable x is defined as $f(x; \alpha, \beta) = (\beta^\alpha \Gamma(\alpha))^{-1} x^{\alpha-1} \exp\{-x/\beta\}$, where $\Gamma(\cdot)$ is the Gamma function.
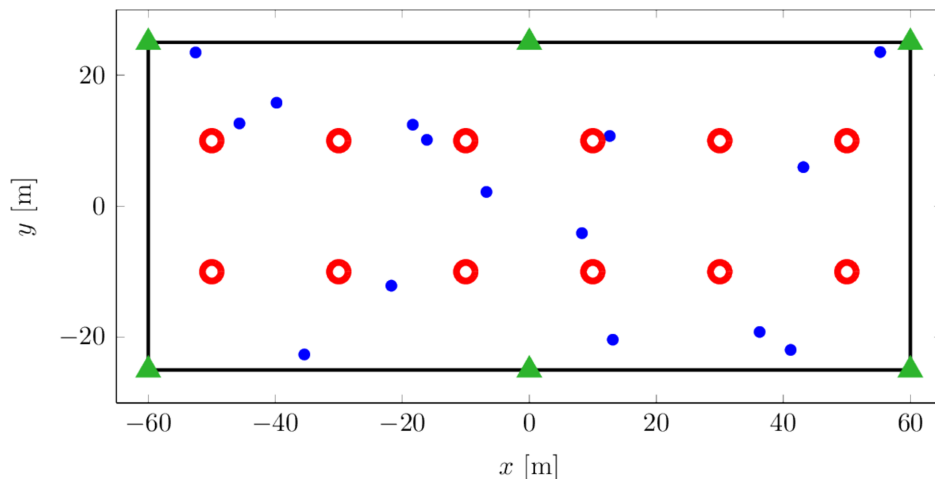
Figure 5.10: IOO scenario with gNBs (red annolous), Wi-Fi APs (green triangles), and a particular instantiation of the UEs (blue dots).

UEs and channel instantiations. For SI-based localization employing a single technology, UE location is inferred via (5.1), while hybrid localization is carried out via (5.2), where the maximum value is obtained via an exhaustive search over the monitored area with a step size of 0.05 meters.[4]

Fig. 5.12 shows the ECDF of the horizontal localization error for the different localization techniques considered in the case of 50 MHz PRS bandwidth at 2 GHz: 5G SVE-based localization; Wi-Fi SVE-based localization; 5G SI-based localization; Wi-Fi SI-based localization; and SI-based localization with data fusion between 5G and Wi-Fi measurements. It can be observed that SI-based localization offers a significant performance improvement with respect to SVE-based localization. In particular, at the 90-th percentile the SI-based approach shows an improvement of approximatively 6 meters and 2 meters compared to SVE-based approach for the individual 5G and Wi-Fi localization, respectively. It can also be observed that, the fusion of 5G DL-TDOA measurements and WI-Fi TOF measurements using the SI-based approach further improves the localization accuracy. In particular, at the 90-th percentile data fusion provides an improvement of approximatively 2 meters with respect to the single technology localizations. At the same percentile, the improvement offered by data fusion compared to 5G and Wi-Fi SVE-based localization is approximatively 8 meters and 4 meters, respectively.

Fig. 5.13 shows the ECDF of the horizontal localization error for the different localization techniques considered in the case of 100 MHz PRS bandwidth at 4 GHz: 5G SVE-based localization; Wi-Fi SVE-based localization; 5G SI-based localization; Wi-Fi

---

[4]A smaller step size would increase the localization accuracy at the cost of a higher latency and simulation time. Depending on the accuracy and latency constraints, the step size parameter can be optimized.
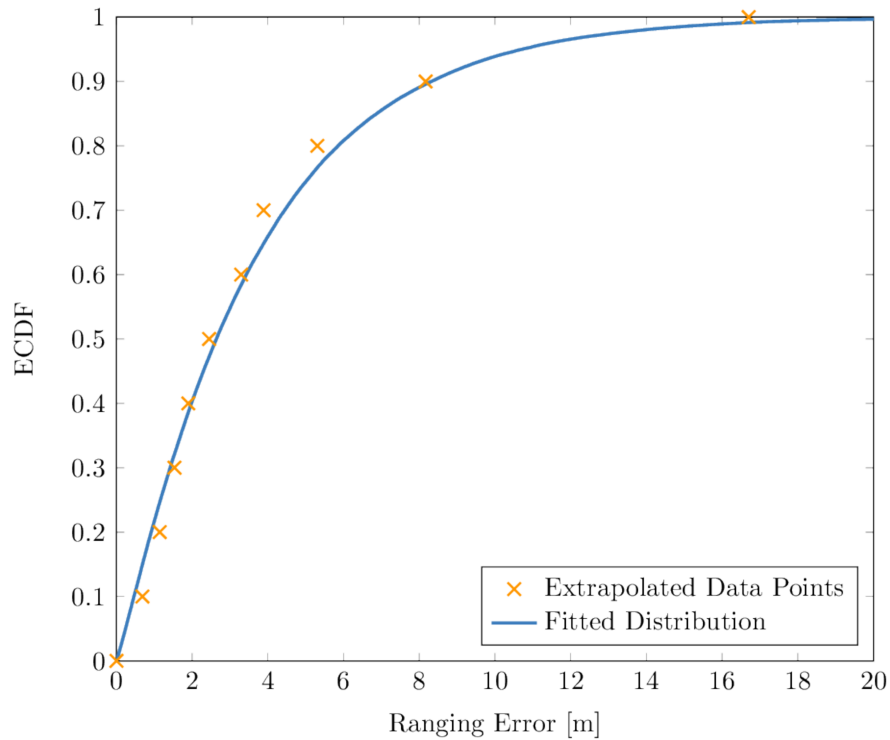
Figure 5.11: Ranging error model based on TOF measurements with Wi-Fi.

SI-based localization; and SI-based localization with data fusion between 5G and Wi-Fi measurements. It can be observed that, SI-based localization for 5G further improves the localization accuracy compared to SVE-based approach. At the 90-th percentiles, SI-based localization provides an improvement of approximatively 5 meters compared to the SVE-based approach. It can also be observed that the data fusion of 5G and Wi-Fi measurements still provides a performance improvement compared to the single technology case despite 5G SI-based localization performs significantly better compared to Wi-Fi SI-based localization. At the 90-th percentile, the improvement provided by the data fusion is approximatively 1 meter compared to individual 5G SI-based localization.

Figure 5.12: ECDF of the horizontal localization error for the different SVE-based and SI-based localization techniques considered in the case of 50 MHz PRS bandwidth at 2 GHz.
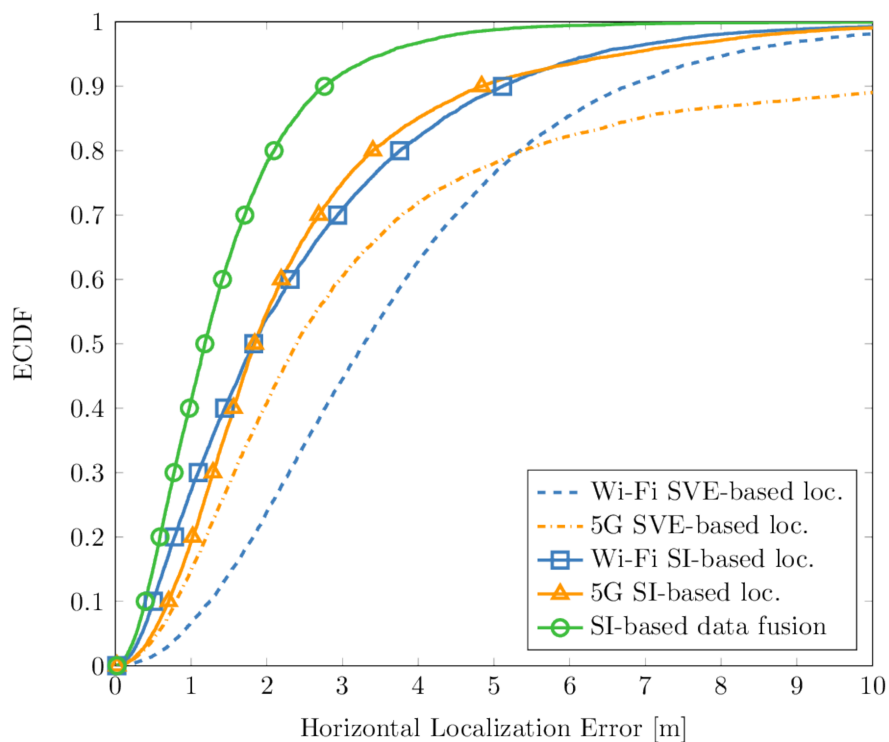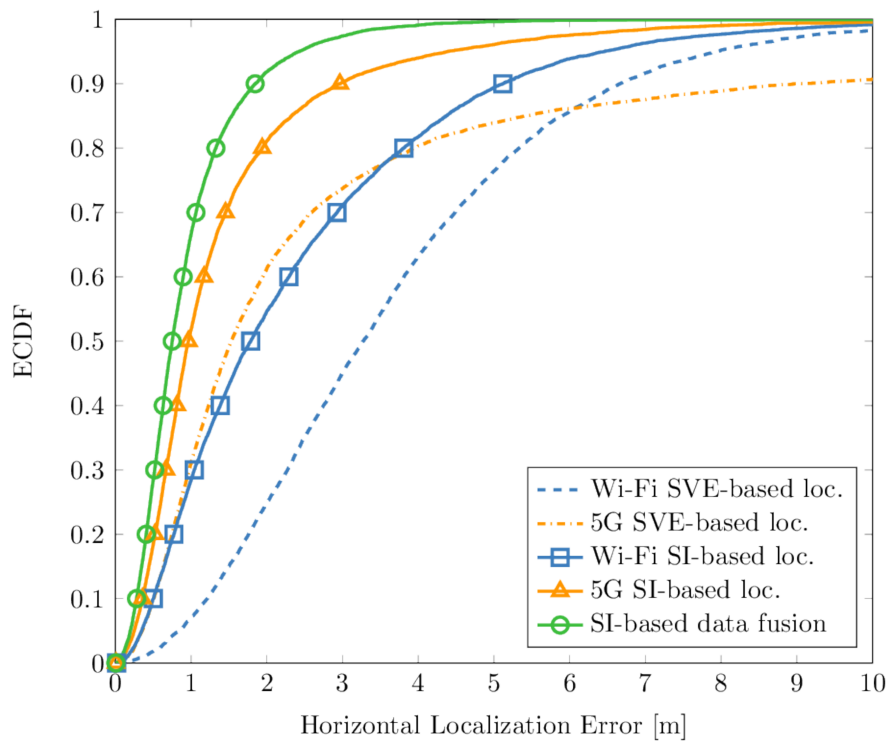

Figure 5.13: ECDF of the horizontal localization error for the different SVE-based and SI-based localization techniques considered in the case of 100 MHz PRS bandwidth at 4 GHz.

Chapter 6

Integration with Sensor Radar Networks

The integration of sensing capabilities in the communication network can be achieved by exploiting the signals already used for communication purposes as signal of opportunity or by integrating radar-based system into the already deployed infrastructure [167–170]. Both approaches poses significant design challenges in terms of shared resource management and coexistence. In this thesis we will focus on the second approach, where sensing is achieved via dedicated radar-based systems, i.e., SRNs. In particular, SRNs leveraging UWB signals are conveying a lot of interest for tracking device-free objects in indoor environments thanks to the ranging accuracy, multipath resolution, and penetration characteristics provided by UWB signals [34, 66, 95, 96, 171, 172]. The design of SRNs for efficient operation in challenging wireless environments requires: (i) derivation of performance limits and benchmarks [2, 88, 114, 173]; (ii) understanding of wireless impairments effects [35, 37, 66, 123, 174]; and (iii) development of algorithms for tracking non-collaborative objects and infer physical analytics [70, 74, 116, 122, 175]. In the following, first a system model for UWB SRNs is proposed, as well as common clutter removal techniques. Then, a statistical characterization of the residual clutter-plus-noise in indoor environments is presented based on experimental data. In addition, the design of a crowd-centric counting algorithm (i.e., an algorithm that does not rely on multi-target localization and data association) is presented and its performance compared with state-of-the-art methods based on real data.

6.1   System Model for SRNs

Consider a SRN in a monostatic or multistatic configuration (i.e., where the transmitters and the receivers are colocated or separated, respectively) with sensor using UWB impulse-radio technologies [89, 90]. The transmitter emits an UWB impulse $u(t)$ at time instant jT_f where $j \in \mathbb{Z}$ and T_f is the frame time. The impulse propagates in the environment and is backscattered by targets and other scatterers (static or dynamic) that are present in the monitored area. The receivers observe the backscattered echoes within a fixed observation time $T_\mathrm{o} \leq T_\mathrm{f}$ before the next impulse is transmitted. The received signal $\mathsf{r}(t)$ at the generic SR receiver can be written as the superposition of the backscattered impulses transmitted at time jT_f. Specifically, where $\mathsf{r}^{(j)}(t)$ is the signal received in the j-th frame, which is given by

$$\mathsf{r}^{(j)}(t) = \mathsf{s}^{(j)}(t) + \mathsf{c}^{(j)}(t) + \mathsf{w}^{(j)}(t) \tag{6.1}$$

for $t \in (jT_\mathrm{f}, jT_\mathrm{f} + T_\mathrm{o}]$ and 0 elsewhere. In (6.1), the process $\mathsf{s}^{(j)}(t)$ encapsulates the informative components for the localization process and contains the signal backscattered from the targets as well as the undesired multipath propagation involving reflections on the targets. Due to the targets' mobility, its statistical properties vary from frame to frame. The process $\mathsf{c}^{(j)}(t)$ represents the undesired clutter components due to dynamic and static scatterers whose statistical properties vary between frames due to the mobility of dynamic scatterers. Notice that the processes $\mathsf{s}^{(j)}(t)$ and $\mathsf{c}^{(j)}(t)$ are not independent. The targets' motion affects the signals backscattered from both static and dynamic scatterers, while the motion of the dynamic scatterers affects the targets' multipath. Last, the process $\mathsf{w}^{(j)}(t)$ is a zero-mean AWGN representing the thermal noise component whose statistical properties do not vary between frames.

Due to the fine resolution provided by the UWB signals, single scatterers cannot be considered point reflectors as in narrowband SRNs and should be treated as range-spread objects [176]. In this case, reflections are made up by infinitesimal contributes determined by the illuminated objects surface. Thus, targets and clutter process cannot be written as a finite sum of discrete components and in the j-th frame interval the components related to the targets backscatter is [177]

$$\mathsf{s}^{(j)}(t) = \int_0^{T_\mathrm{o}} u(t - \tau)\varsigma^{(j)}(\tau)d\tau \tag{6.2}$$

where $\varsigma^{(j)}(\tau)$ is a stochastic process representing the distributed reflections from the tar-

gets. Similarly, the components related to the clutter is

$$\mathsf{c}^{(j)}(t) = \int_0^{T_o} u(t - \tau)\kappa^{(j)}(\tau)d\tau \tag{6.3}$$

where $\kappa^{(j)}(\tau)$ is a stochastic processes representing the distributed reflections from the dynamic and static scatterers. In order to reduce the detrimental effects determined by AWGN, prior to the clutter mitigation techniques, successive frames can be coherently accumulated:

$$\mathsf{r}^{(j)}(t) = \frac{1}{N_I} \sum_{i=(j-1)N_I}^{j} \mathsf{r}^{(i)}(t) \tag{6.4}$$

6.2   Clutter Mitigation in SRNs

Various clutter mitigation filters are available in literature [65, 101, 178]. In particular, we will focus on the empty room (ER), exponential averaging filter (EAF), and single-delay canceller (SDC), all of which aim to the estimate the clutter response and subtract it from the received frames. In the case of ER, the filtered signal after clutter mitigation can be written as

$$\mathsf{x}^{(j)}(t) = \mathsf{r}^{(j)}(t) - \hat{c}(t) \tag{6.5}$$

where $\hat{c}(t) = \sum_{h=1}^{N_a} r^{(h)}(t)/N_a$ is an estimate of the response of the wireless environment in absence of targets, i.e., only clutter. This technique exhibits good performance in static environments and is suitable for implementation on low complexity devices. The main drawback is represented by the poor performance in quasi-static or dynamic environments and its non adaptive nature. The EAF overcomes some of the ER downsides by iteratively updating the environment response. The filtered signal is given by

$$\mathsf{x}^{(j)}(t) = \mathsf{r}^{(j)}(t) - \hat{\mathsf{c}}^{(j)}(t) \tag{6.6}$$

where the clutter response is updated frame by frame as $\hat{\mathsf{c}}^{(j)}(t) = \beta\hat{\mathsf{c}}^{(j-1)}(t) + (1-\beta)\mathsf{r}^{(j)}(t)$. The parameter $\beta \in (0, 1)$ weights the clutter signal at the previous frame and the current received frame to obtain the current clutter estimate. This mitigation filter rejects the static clutter while being robust to slow environmental changes. However, echoes originated by slow moving targets are also attenuated, potentially causing performance degradation. On the other hand, the SDC filter estimates the clutter response as the

previous received frame, i.e. $\hat{\mathsf{c}}^{(j)}(t) = \mathsf{r}^{(j-1)}(t)$, and the filtered signal can be written as

$$\mathsf{x}^{(j)}(t) = \mathsf{r}^{(j)}(t) - \mathsf{r}^{(j-1)}(t) \,. \tag{6.7}$$

The SDC is particularly suitable for high maneuvering targets and exhibits good performance even for dynamic environments, until the per-frame variability of the targets echoes is greater than the clutter one.

6.3 Clutter Characterization in SRNs

Accurate modeling of the wireless impairments affecting the SRNs' operations is essential to design SRNs capable of achieving satisfactory performance in terms of localization and tracking accuracy [55,65,179–181]. Among various wireless impairments, the clutter, i.e., the unwanted echoes generated by scatterers not meaningful for the target localization process, represents one of the major challenges [101]. The clutter, if not mitigated or properly taken into account, might lead to noticeable performance degradation [37]. In particular, an accurate characterization of the clutter is essential to establish performance benchmarks, develop robust mitigation filters, and design inference algorithms [2, 182–184].

However, clutter characterization is a difficult task due to the heterogeneous operation conditions encountered in real applications. The ability to distinguish between clutter and useful echoes (i.e., echoes that carry positional information about the targets) depends on the specific environment and application. For example, in synthetic-aperture radars the echoes determined by the background are essential to obtain an accurate image of the environment [176], while in surveillance radar they deteriorate the detection capability [72]. In general, the characteristics of the echoes depend on: (i) the environment (e.g., outdoor, sea, or indoor); (ii) SRN operation (e.g., monostatic vs. multistatic); and (iii) the signaling employed (e.g., continuous wave or impulsive).

The clutter can be modeled as a stochastic process, whose characteristics vary if observed prior or after clutter mitigation filtering. Several statistical models have been proposed in the literature to describe the clutter amplitude or power and its variability in terms of Doppler spectrum [185–189].

Despite clutter characterization has been largely studied for narrowband radars in a variety of frequency bands and operating conditions, no well-established counterparts exist for SRNs operating in indoor environments with wideband and UWB signals [89]. The performance analysis (e.g., the derivation of theoretical bounds) and the design of algorithms (e.g. coherent or noncoherent detectors for ranging) for UWB SRNs rely on

Figure 6.1: Pictorial representation of the clutter mitigation filter. Signals in input are defined in (6.1) and represent the components relative to the target, clutter, and thermal noise, respectively. Signals in output are defined in (6.9) and represent the component relative to the filtered target component and clutter-plus-noise, respectively.

the statistics of the clutter-plus-noise component after clutter mitigation filtering. In particular, the clutter-plus-noise distribution and its statistical properties in terms of stationarity and correlation greatly affect the design of the inference algorithms [33, 34, 96, 101].

6.3.1   Static Clutter

Consider a static environment with no targets. Then, the received signal in (6.1) simplifies to

$$\mathsf{r}^{(j)}(t) = \mathsf{c}^{(j)}(t) + \mathsf{w}^{(j)}(t) \tag{6.8}$$

where the only contributes are due to static clutter and AWGN, with $\mathsf{c}^{(j)}(t)$ being typically the predominant component. Due to the absence of moving targets or moving scatterers, the statistical properties of $\mathsf{c}^{(j)}(t)$ and therefore the ones of $\mathsf{r}^{(j)}(t)$ and $\mathsf{x}^{(j)}(t)$, do not depend on the particular frame index j. Regardless of the clutter mitigation filter employed, from (6.1) the filtered received signal can be rewritten as

$$\mathsf{x}^{(j)}(t) = \tilde{\mathsf{s}}^{(j)}(t) + \mathsf{n}^{(j)}(t) \tag{6.9}$$

where $\tilde{\mathsf{s}}^{(j)}(t)$ represents the filter output when the input is $\mathsf{s}^{(j)}(t)$ and $\mathsf{n}^{(j)}(t)$ represents the residual clutter-plus-noise, which is the filter output when the input is $\mathsf{c}^{(j)}(t) + \mathsf{w}^{(j)}(t)$ (see Fig. 6.1). A statistical characterization of $\mathsf{n}^{(j)}(t)$ is required to design algorithms for detecting $\tilde{\mathsf{s}}^{(j)}(t)$ or inferring parameters related to $\tilde{\mathsf{s}}^{(j)}(t)$. Furthermore, the theoretical analysis of such algorithms (e.g. derivation of the detection probability, false alarm probability, estimation error, and variance) depends on the underlying statistical model of the signals [33, 34, 177].

In general, a complete characterization of the process $\mathsf{n}^{(j)}(t)$ based on the filtered signal

Figure 6.2: Measurement campaign environment in the Department of Engineering at the University of Ferrara.

$x^{(j)}(t)$ is difficult due to the time-varying nature of the process and the interdependency between the clutter-plus-noise and targets processes. However, we can initially consider only the clutter determined by static scatterers (e.g., ground, walls, and furnitures) in the absence of targets. In such a scenario, the filtered signal in (6.9) simplifies to $x^{(j)}(t) = n^{(j)}(t)$, where only the residual clutter-plus-noise is observed at the filter's output. The statistical properties of $n^{(j)}(t)$ do not depend on the particular frame index j. Therefore, the process $x^{(j)}(t)$ can be considered as a time shift of an underlying process $x(t)$. A set of M sample functions $\{x^{(j)}(t)\}_{j \in \mathcal{M}}$ with frame index set $\mathcal{M} = \{1, 2, \ldots, M\}$ can be regarded as different realizations of the process $x(t)$. This allows to determine the statistical properties of $x(t)$ based on successive received frames $\{x^{(j)}(t)\}_{j \in \mathcal{M}}$.

Remark: The echoes due to the background and large static objects are typically greater in amplitude and exhibit a longer duration compared to the ones originated by moving scatterers. Moreover, the absence of dynamic scatterers allows to consider approximatively independent the processes $\tilde{s}^{(j)}(t)$ and $n^{(j)}(t)$, with the targets' motion determining only partial shadowing of the static reflectors. Therefore, the clutter characterization in a scenario with no targets and only static scatterers is crucial for addressing the clutter characterization problem.
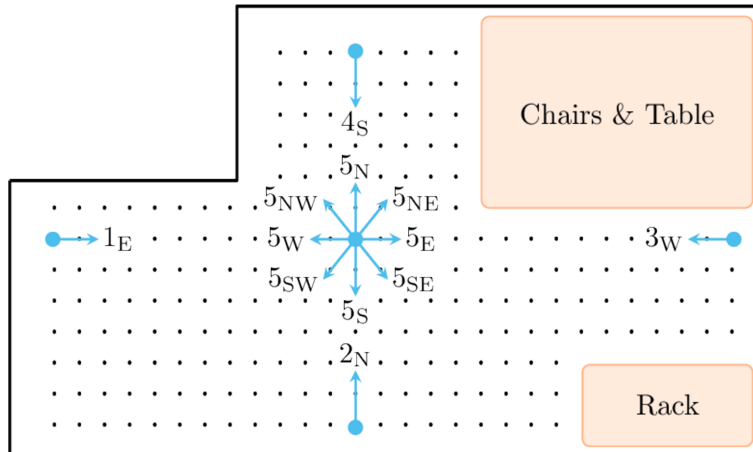
Figure 6.3: Map of the environment with the different SR spatial configurations. The spacing between the grid points is approximatively 0.3 m.

6.3.2 Measurement Campaign

The clutter characterization will be based on measurements obtained with a monostatic UWB SR in an indoor environment. Then, we define the discrete version of $\mathsf{x}(t)$ as $\mathsf{x}_i = \mathsf{x}(iT_\mathrm{s})$, where $i \in \mathcal{N} = \{1, 2, \ldots, N\}$, $\mathcal{N}$ is the discrete index set in which $N = \lfloor T_\mathrm{o}/T_\mathrm{s} \rfloor$ is total number of sample in an observation interval, and T_s is the sampling time. Denote with $x_i^{(j)}$ the i-th sample of the j-th realization $x^{(j)}(t)$, i.e. $x_i^{(j)} = x^{(j)}(iT_\mathrm{s})$. The statistical characterization is based on the samples set $\{x_i^{(j)}\}_{i \in \mathcal{N}}^{j \in \mathcal{M}}$.

The measurements were carried out within an area of approximatively 9 m × 4 m, where the presence of a table, chairs, panels, walls, and other objects leads to a large number of potential scatterers. A picture of the environment is given in Fig. 6.2. The SR employed is based on Novelda's X4M03 chip. The main parameters of the SR and of the measurement campaign are summarized in Tab. 6.1. A total of 12 different spatial configurations (position and orientation) were used, 4 with the SR facing the center of the room as in a possible displacement for the SRN operation, and 8 where the SR is placed at center of the area facing 8 different directions. The configurations are indexed by a number representing the position and a subscript representing the orientation (see Fig. 6.3). The measurements at different configurations are analyzed separately and composed of $M = 250$ frames and $N = 1245$ samples per frame. The frames cover a range of approximately 8 m.

6.3.3 Statistical Characterization

We now investigate the stationarity, correlation, and distribution of received signal samples $\mathsf{x}(t)$ after clutter mitigation filtering. On the one hand, stationarity and correlation

Table 6.1: SR and measurement campaign parameters.

Parameter (Symbol)	Value
SR pulse shape	Gaussian
SR carrier frequency	7.26 GHz
SR pulse bandwidth	1.4 GHz
SR energy per pulse	2.6 pJ
Repetition interval (T_{f})	40 ms
Observation time (T_{o})	43.4 ns
Sample time (T_{s})	42.8 ps
Number of configurations tested	12
Number of frames recorded per configuration (M)	250
Number of samples per frame (N)	1245

are properties of the process x_i, which depend on the discrete temporal index i. On the other hand, the process distribution is defined as the distribution of the RV $\mathsf{x}_{i^\star}$, where $i^\star$ is a fixed time index with $i^\star \in \mathcal{N}$. In our case, stationarity and correlation are evaluated from the samples $\{x_i^{(j)}\}_{i \in \mathcal{N}}$ for each frame indexed by j, while samples distribution is evaluated from the samples $\{x_i^{(j)}\}_{j \in \mathcal{M}}$ for each sample indexed i.

As a first qualitative test, we use visual plots of the first-order statistics (e.g., mean and variance) to evaluate the non-stationarity of the process by determining if such statistics depend on the sample index i. In particular, the sample mean is $\hat{\mu}_i = \sum_{j \in \mathcal{M}} x_i^{(j)}/M$, while the sample variance is $\hat{\sigma}_i^2 = \sum_{j \in \mathcal{M}} (x_i^{(j)} - \hat{\mu}_i)^2/(M-1)$. Indeed, if such dependency can be assessed by visual inspection, i.e., $\hat{\mu}_i \neq \hat{\mu}_k$ or $\hat{\sigma}_i^2 \neq \hat{\sigma}_k^2$ for $i \neq k$ and $i, k \in \mathcal{N}$, the process x_i can be assumed non-stationary. Otherwise, if such dependency cannot be identified, quantitative tests are necessary to asses the process stationarity.

As a second quantitative test, we use the LBT for evaluating the correlation of the process x_i. Assume x_i as stationary and denote the discrete autocorrelation function at time lag k (i.e., sample index difference) as ϱ_k. Formally, the Ljung–Box test (LBT) tests the hypotheses

$$\mathcal{H}_0: \quad \forall k \in \mathcal{N}_{\mathrm{L}}, \quad \varrho_k = 0 \tag{6.10a}$$

$$\mathcal{H}_1: \quad \exists k \in \mathcal{N}_{\mathrm{L}}, \quad \varrho_k \neq 0 \tag{6.10b}$$

where $\mathcal{N}_{\mathrm{L}} = \{1, 2, \ldots, N_{\mathrm{L}}\}$, and N_{L} is the maximum time lag tested. In our case, we can

apply the LBT for each frame index j on the samples $\{x_i^{(j)}\}_{i \in \mathcal{N}}$. Consider a frame index j and $\hat{\mu}_i = \hat{\mu} = 0$, then the ϱ_k can be estimated as $\hat{\varrho}_k^{(j)} = \hat{v}_k^{(j)}/\hat{v}_0^{(j)}$ where

$$\hat{v}_k^{(j)} = \frac{1}{N} \sum_{h=1}^{N-k} x_h^{(j)} x_{h+k}^{(j)} \tag{6.11}$$

is the estimate of the autocovariance function. The test statistic employed to reject the null hypothesis is based on the estimated autocorrelation function and is given by

$$q^{(j)} = N(N+2) \sum_{k \in \mathcal{N}_{\mathrm{L}}} \frac{(\hat{\varrho}_k^{(j)})^2}{N-k}. \tag{6.12}$$

If the test statistic $q^{(j)}$ exceeds a certain critical value λ_α, i.e. $q^{(j)} > \lambda_\alpha$, the hypothesis $\mathcal{H}_0$ is rejected with significance level α (i.e., the samples can be assumed correlated). Otherwise, the test fails to reject $\mathcal{H}_0$ and the samples are considered uncorrelated. Critical values for different significance levels α and sample sizes are available [190]. In the asymptotic regime ($N_{\mathrm{L}} \to +\infty$) the test statistic is distributed as a chi-square distribution with N_{L} degrees of freedom and the critical value λ_α is the $1 - \alpha$ quantile of the distribution.

Various statistical tests can be employed for determining if the samples are well-modeled by a Gaussian distribution. In our case, we want to test for each sample index i if the samples $\{x_i^{(j)}\}_{j \in \mathcal{M}}$ can be considered realizations of a Gaussian RV. Consider a fixed time index i, formally goodness-of-fit tests for Gaussian distributions verifies the hypothesis

$$\mathcal{H}_0 : \quad \{x_i^{(j)}\}_{j \in \mathcal{M}}, \quad f_{\mathsf{x}_i}(x) \in \mathcal{F}(x; \mu, \sigma^2) \tag{6.13a}$$

$$\mathcal{H}_1 : \quad \{x_i^{(j)}\}_{j \in \mathcal{M}}, \quad f_{\mathsf{x}_i}(x) \notin \mathcal{F}(x; \mu, \sigma^2) \tag{6.13b}$$

where $\mathcal{F}(x; \mu, \sigma^2)$ is a family of Gaussian distributions parametrized by mean μ and variance σ^2. Anderson–Darling test (ADT) is employed to test Gaussianity since it exhibits a small probability of incurring in type-II error compared to other tests and it is able to detect small departures from the Gaussian distribution in the tails of the empirical distribution [190]. The ADT quantifies the square difference between the ECDF defined as

$$\tilde{F}_{i,M}(x) = \frac{|\{x_i^{(j)}, j \in \mathcal{M} : x_i^{(j)} \le x\}|}{M} \tag{6.14}$$

and the hypothesized comulative density function (CDF) $F_{\mathsf{x}_i}(x)$. In case of known mean
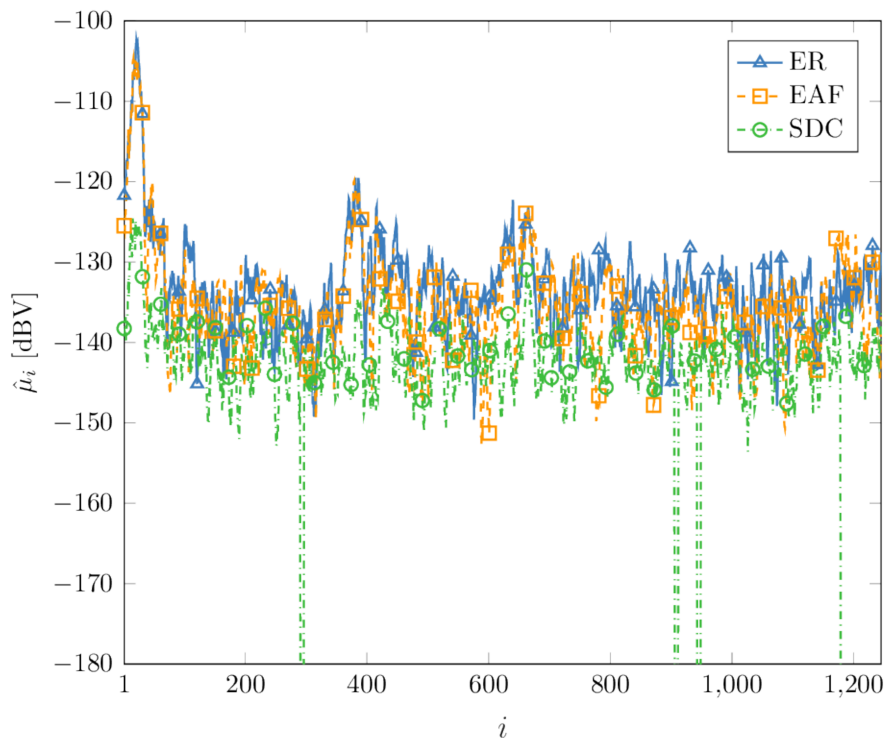
Figure 6.4: Sample mean for the configuration 5_E with the three different clutter mitigation filters employed: ER, EAF, and SDC.

and variance, the functional form of the test statistic is given by

$$a_i = M \int_{-\infty}^{+\infty} \frac{(\tilde{F}_{i,M}(x) - F_{\mathsf{x}_i}(x))^2}{F_{\mathsf{x}_i}(x)(1 - F_{\mathsf{x}_i}(x))} dF_{\mathsf{x}_i}(x) \tag{6.15}$$

where the term at the denominator $F_{\mathsf{x}_i}(x)(1 - F_{\mathsf{x}_i}(x))$ can be seen as a weighting function assigning more weight to the difference in the distribution tails. Operatively, exploiting the property that a RV composed with its true CDF is uniformly distributed, the test statistic a_i can be evaluated from the ordered samples $x_i^{(1)} \leq x_i^{(2)} \leq \ldots \leq x_i^{(M)}$ as

$$a_i = -M - \frac{1}{M} \sum_{j \in \mathcal{M}} \left[(2j - 1) \ln\left(z_i^{(j)}\right) + \ln\left(z_i^{(M+1-j)}\right) \right] \tag{6.16}$$

where $z_i^{(j)} = \tilde{F}_{i,M}(x_i^{(j)})$[1]. The hypothesis $\mathcal{H}_0$ is rejected at significance level α, i.e. the samples are not considered Gaussian distributed if $a_i > \lambda_\alpha$. Similarly to the LBT, λ_α has been tabulated for different sample sizes and significance level α [190]. Differently from the LBT, the asymptotic distribution of the test statistic has no closed form and the critical values have been obtained via Monte Carlo methods.

---

[1]If the mean and variance are estimated from the samples $\{x_i^{(j)}\}_{j \in \mathcal{M}}$, a correction factor needs to be multiplied to the test statistic.

6.3.4 Results

Consider the experimental setting described in Sec. 6.3.2. Given a specific spatial configuration of the SR, we define $R_C = N_C/M$ as the ratio between the number of frames that exhibit correlation N_C, assessed via LBT, and the total number of frame M in each configuration. Similarly, given a specific configuration we define $R_G = N_G/M$ as the ratio between the number of sample that can be considered Gaussian distributed N_G, assessed via ADT, and the total number of samples N in each configuration. Both LBT and ADT are conducted at significance level $\alpha = 0.05$, with $N_L = 20$ for the LBT. The weighting parameter for the EAF is $\beta = 0.8$.

Fig. 6.4 shows the sample mean for the configuration 5_E as a function of the sample index i for the different clutter mitigation filters considered. It can be observed that the mean estimate exhibits great variability from sample to sample. In particular, it can be identified a peak of approximatively -100 dB in the first 50 samples for all the mitigation filters. This can be attributed to the direct path between the transmitter and receiver antennas. Moreover, other two peaks of approximatively -120 dB and width of several samples can be identified at $i \approx 400$ and $i \approx 600$. These can be attributed to large scatterers, such as the table and the wall. At the same sample indices, similar peaks can be recognized in Fig. 6.5, where it is showed the sample variance for the same configuration as a function of the sample index i. Similar trends can be observed for the mean and the variance in the other configurations recorded, where peaks can be identified in correspondence of large scattered echoes. Furthermore, these peaks are present regardless of the mitigation filter considered. Notice that, the presence of such peaks violate the definition of stationarity and their width is attributable to the characteristics of the UWB signals. In fact, due to the fine spatial resolution provided by UWB signals, the mitigated echoes from static scatterers span multiple sample indices.

Tab. 6.2 shows R_C for the configurations considered and different clutter mitigation filters. It can be noticed that the percentage of frames exhibiting correlation exceeds the 80% for all the configurations and mitigation filters. It can also be noticed that the filtered samples obtained with the ER exhibit the larger percentage (greater than 90%) of correlated frames, while the lowest is obtained employing the SDC. This can be attributed to the fact that the ER filter does not affect the statistical properties of the input process, being the output process a simple location shift of the input process. On the other hand, the SDC mitigates the clutter and increases the power of the AWGN which is assumed uncorrelated.

Tab. 6.3 shows R_G for the configuration considered and different clutter mitigation filters. It can be noticed that the percentage of samples well modeled by a Gaussian
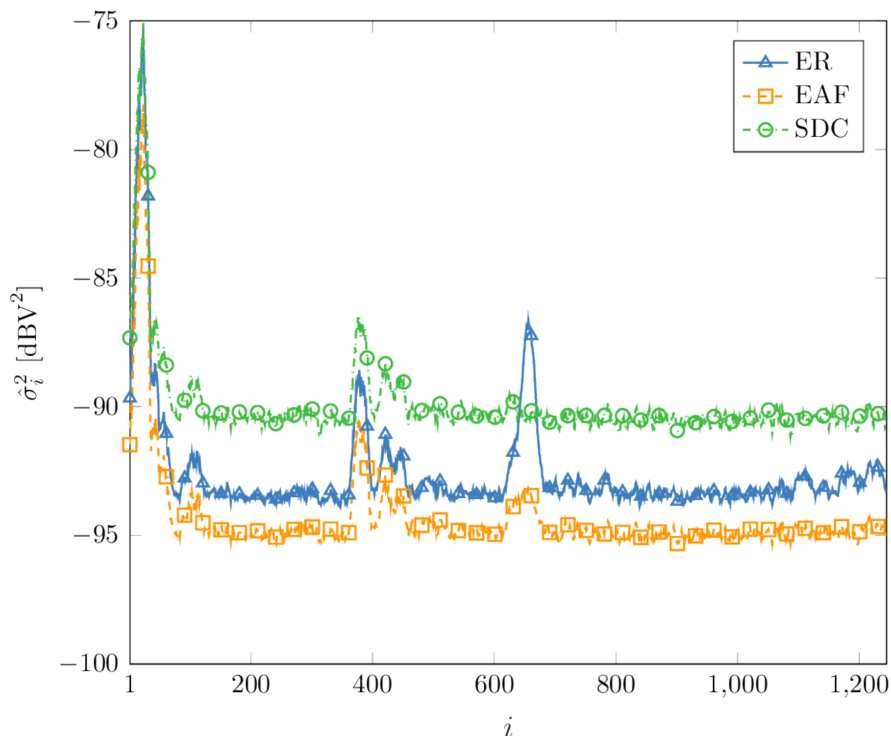
Figure 6.5: Sample variance for the configuration 5_E with the three different clutter mitigation filters employed: ER, EAF, and SDC.

distribution exceeds the 90% in the majority of the configurations. In particular, for EAF and SDC the R_G is almost 95% for all the configuration. In the case of ER, the values of R_G is slightly inferior, with R_G greater than 90% in all location, except for 2_N where $R_G \approx 82\%$. This can be attributed to minor variation of the environment between the formation of the ER response and the actual measurement.

Given the results, the process describing the sample amplitudes after clutter mitigation filtering can be considered Gaussian distributed. Moreover, this process can be assumed non-stationary in the first-order statistics and exhibits correlation. The non-stationarity can be attributed to the large number of potential scatterers in indoor environments and the characteristics of the UWB signals, in particular to their fine spatial resolution. These are important properties that must be taken into account for the derivation of performance benchmarks and the design of robust inference algorithms.

6.4   Crowd-Centric Counting via SRNs

In addition to localization and tracking, physical analytics which can be extracted directly from the received waveform are a key enabler for various application. In particular, counting the number of target in a monitored area is relevant for myriad of crowd sensing and behavior analysis applications [17, 21, 191, 192]. For counting tasks, radio-based

Table 6.2: Rate of correlated frames for different configurations and clutter mitigation filtering.

Configuration	Rate of Correlated Frames, R_{C}		
	ER	EAF	SDC
1_{E}	0.92	0.87	0.80
2_{N}	0.99	0.88	0.85
3_{W}	0.95	0.88	0.86
4_{S}	0.99	0.92	0.81
5_{E}	0.95	0.85	0.80
5_{NE}	0.94	0.86	0.83
5_{N}	0.99	0.88	0.84
5_{NW}	0.96	0.88	0.82
5_{W}	0.92	0.85	0.80
5_{SW}	0.96	0.88	0.85
5_{S}	0.95	0.87	0.81
5_{SE}	0.98	0.85	0.80

Table 6.3: Rate of Gaussian samples for different configurations and clutter mitigation filtering.

Configuration	Rate of Gaussian Samples, R_{G}		
	ER	EAF	SDC
1_{E}	0.94	0.96	0.96
2_{N}	0.82	0.94	0.96
3_{W}	0.91	0.94	0.96
4_{S}	0.95	0.96	0.96
5_{E}	0.93	0.95	0.96
5_{NE}	0.93	0.95	0.96
5_{N}	0.93	0.96	0.95
5_{NW}	0.92	0.95	0.95
5_{W}	0.94	0.95	0.96
5_{SW}	0.94	0.95	0.96
5_{S}	0.94	0.94	0.96
5_{SE}	0.91	0.96	0.95

systems are preferred to image-based systems [83, 193–195], especially when privacy, implementation costs, and obstructed line-of-sight represent important limitations. Among radio-based systems, device-free systems are often preferred to systems that rely on dedicated or personal devices [62, 196–199].

Device-free systems are based on networks of SRs that sense the wireless environment and detect targets from signal reflections (backscattering) [37, 55, 65, 74, 101, 149]. The presence of obstacles and other scatterers (e.g., furniture, walls, and windows) leads to clutter and multipath propagation, which have detrimental effects on the detection performance. These phenomena are particularly severe in indoor environments, where the number of scatterers is large [2, 34, 200].

Conventional approaches for device-free counting via SRs rely on multi-target localization or tracking [180, 201], where each SR estimates a set of metrics (e.g., ranges or angles) associated to a single detected target (namely, individual-centric approach). Typically, this approach has a complexity that grows exponentially with the number of targets due to data association. Individual-centric information and data association are unnecessary when the system is only interested in crowd-centric information (i.e., the number of targets). Therefore, there is a growing interest in conceiving methods that infer the number of targets without relying on localization (namely, crowd-centric approach). Existing models for relating the received waveforms to the number of targets depend on the specific environment and multipath conditions [79, 106, 107].

In [137], the number of targets is inferred directly from energy samples of the received waveform and relying on a statistical characterization of the wireless channel. However such statistical characterization may be unknown a priori. As a possible solution, learning techniques can be employed to directly estimate the generative model of the measurements via a training phase. Recently, unsupervised learning has been successfully applied to ranging for network localization [54, 55]. In soft range information, nodes' position is determined based on the information obtained though unsupervised machine learning techniques in the form of likelihood functions instead of single-value metrics (e.g., time-of-arrival, angle-of-arrival, and received signal strength). The use of unsupervised learning for device-free counting allows the system to skip the estimation of single-value metrics and exploit the whole received waveform to extract information about the number of targets. Moreover, the use of likelihood functions enables an efficient fusion of the information provided by each SR.
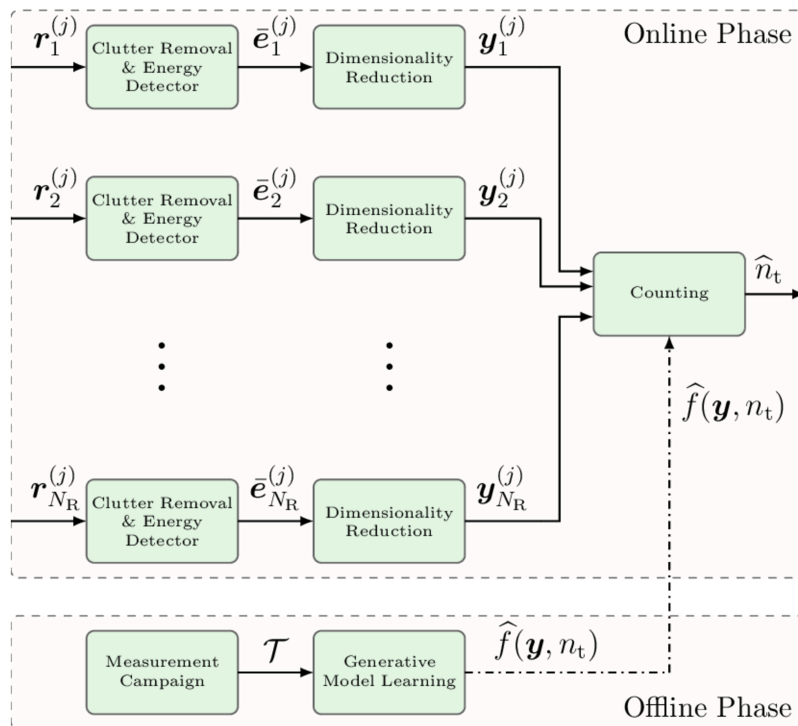
Figure 6.6: Scheme of crowd-centric counting via unsupervised learning.

6.4.1   Counting via Unsupervised Learning

Consider a network composed of N_{R} monostatic SRs in known positions, with index set $\mathcal{N}_{\mathrm{R}} = \{1, 2, \cdots, N_{\mathrm{R}}\}$. Each SR transmits an impulse signal $u(t)$ at each time instant jT_{f}, where $j \in \mathbb{Z}$ and T_{f} is the frame time. The signal propagates in the wireless environment where a random number n_{t} of targets. The signal is backscattered from the targets as well as from any object in the monitored area, leading to multiple echoes. For the generic SR the received signal $\mathsf{r}^{(j)}(t)$ in the j-th frame, i.e., $t \in (jT_{\mathrm{f}}, jT_{\mathrm{f}} + T_{\mathrm{o}}]$, is given by (6.1). Then, $\mathsf{r}^{(j)}(t)$ is processed frame-by-frame using a clutter removal filter. Consider the vector $\mathsf{r}^{(j)}$ of $n_{\mathrm{s}} = \lfloor T_{\mathrm{obs}}/T_{\mathrm{s}} \rfloor$ received signal samples obtained within the j-th frame, where T_{s} is the sampling time. The choice of the clutter removal filter depends on the clutter dynamics. We will consider the EAF introduced in Sec. 6.2, which is widely adopted when the clutter is static or varies slowly with the respect to the targets. The filter output for the j-th frame can be rewritten as

$$\tilde{\mathsf{r}}^{(j)} = \mathsf{r}^{(j)} - \frac{1}{N_{\mathrm{MA}}} \sum_{i=j-1-N_{\mathrm{MA}}}^{j-1} \mathsf{r}^{(i)} \tag{6.17}$$

where N_{MA} represents the number of frames used to estimate the clutter components. The estimate is updated every frame to capture the slow variations of the clutter. Such a

clutter removal filter prevents the counting of static targets. However, due the fine time resolution of UWB signals, a person standing in a static position is not a static target due to the respiration motions. This makes the EAF well suited for applications involving the count of persons such as affluence analytics and flow monitoring.

A number N_{int} of frames can be non-coherently accumulated at the output of an energy detector to reduce the noise effect. First, a vector $\mathbf{e}^{(j)}$ of $N_{\text{bin}} = \lfloor T_{\text{obs}}/T_{\text{d}} \rfloor$ energy bins is obtained through a quadrature integration and dump block, where T_{d} represents the dwell time and the k-th bin is given by

$$\mathsf{e}_k^{(j)} = \sum_{h=kN_{\text{d}}}^{(k+1)N_{\text{d}}} |\tilde{\mathsf{r}}_h^{(j)}|^2 \tag{6.18}$$

in which $N_{\text{d}} = \lfloor T_{\text{d}}/T_{\text{s}} \rfloor$ represents the number of samples in each energy bin, and $\tilde{\mathsf{r}}_h^{(j)}$ is the h-th element of $\tilde{\mathbf{r}}^{(j)}$. Then, the energy bin vectors from different frames are averaged as

$$\bar{\mathbf{e}}^{(j)} = \frac{1}{N_{\text{int}}} \sum_{i=(j-1)N_{\text{int}}}^{jN_{\text{int}}} \mathbf{e}^{(i)}. \tag{6.19}$$

Note that a new energy vector $\bar{\mathbf{e}}^{(j)}$ is obtained every N_{int} observation frames, i.e. at time $jN_{\text{int}}T_{\text{f}}$ with $j \in \mathbb{Z}$. Consider a fixed frame index j, denote with $\mathbf{r}_i$ and $\bar{\mathbf{e}}_i$ the vectors representing the received signal samples and the energy bins for the i-th SR, respectively. The counting system aims to infer the number of targets n_{t} from the observed data $\{\boldsymbol{y}_i\}_{i \in \mathcal{N}_{\text{R}}}$. The observed data may refer to the received signal samples $\mathbf{y}_i = \mathbf{r}_i$ and the estimate $\widehat{n}_{\text{t}}$ is updated frame by frame (i.e., at time jT_{o} with $j \in \mathbb{Z}$), or can refer to the energy vectors $\mathbf{y}_i = \bar{\mathbf{e}}_i$ and the estimate $\widehat{n}_{\text{t}}$ is updated every N_{int} frames (i.e., at time $jN_{\text{int}}T_{\text{f}}$ with $j \in \mathbb{Z}$).

In crowd-centric approaches, which do not rely on target positional information, the ML estimate of n_{t} is

$$\widehat{n}_{\text{t}} = \operatorname*{argmax}_{n_{\text{t}}} \prod_{i \in \mathcal{N}_{\text{R}}} f_{\mathbf{y}|n_{\text{t}}}(\boldsymbol{y}_i | n_{\text{t}}) \tag{6.20}$$

where the measurement sets are considered independent and identically distributed among the different SRs for a given n_{t}. The random vector $\mathbf{y}$ represents the measurement set associated to an unspecified SR.

We propose a technique for crowd-centric counting of device-free targets via unsupervised machine learning. First, a generative model (i.e., the joint PDF $f(\boldsymbol{y}, n_{\text{t}})$) is learned

during a training phase where a data set $\mathcal{T} = \{\boldsymbol{y}_l\}_{l \in \mathcal{N}_\mathrm{T}}$ of N_T measurements indexed by $\mathcal{N}_\mathrm{T}$ are collected. Then, $f(\boldsymbol{y}|n_\mathrm{t})$ can be obtained from $f(\boldsymbol{y}, n_\mathrm{t})$ with a priori knowledge $f(n_\mathrm{t})$. The dimensionality of the problem depends on the size of $\mathbf{y}$. In particular, the use of the received signal samples vector $\mathbf{y} = \mathbf{r}$ or of the energy vector $\mathbf{y} = \bar{\mathbf{e}}$ may lead to high computational complexity.[2] Therefore, dimensionality reduction is performed on $\bar{\mathbf{e}}$ by defining two descriptive features and principal component analysis (PCA) [202].

Consider $\mathbf{y} = [\max\{\bar{\mathbf{e}}\}, \mathsf{n}_\mathrm{p}, \psi(\bar{\mathbf{e}})]^\mathrm{T}$, where $\max\{\bar{\mathbf{e}}\}$ is the global maximum for the vector $\bar{\mathbf{e}}$, n_p is the number of local maxima, and $\psi(\bar{\mathbf{e}})$ is a $1 \times d$ vector, containing the first d principal components of the $n_\mathrm{bin} \times 1$ vector $\bar{\mathbf{e}}$, i.e.

$$\psi(\bar{\mathbf{e}}) = \frac{1}{\max\{\bar{\mathbf{e}}\}} \bar{\mathbf{e}}^\mathrm{T} \boldsymbol{V} \tag{6.21}$$

where $\boldsymbol{V}$ is a $n_\mathrm{bin} \times d$ matrix with columns given by the eigenvectors associated to the d largest eigenvalues of $\boldsymbol{\Sigma}$, which is the $n_\mathrm{bin} \times n_\mathrm{bin}$ sample covariance matrix of the vectors $\{\bar{e}_l / \max\{\bar{e}_l\}\}_{l \in \mathcal{N}_\mathrm{T}}$. The global maximum of the energy bin vector can be related to the presence of targets in the operating environment, while the number of peaks represents a first coarse approximation for the number of targets. Though the advantages of being easily obtainable, these two descriptive features do not encapsulate all the information carried by $\bar{\mathbf{e}}$. In contrast, PCA provides a concise representation of $\bar{\mathbf{e}}$ by projecting the data into a low-dimension linear subspace while ensuring the lowest mean-square error. The main drawback of the PCA approach is when highly nonlinear relation is present between the number of targets and $\bar{\mathbf{e}}$ as this dimensionality reduction technique fails to preserve the information carried by the measurements.

Learning the generative model for $\mathbf{y}$ is a density estimation problem with both continuous and discrete RVs. The jittering technique is employed to transform the discrete RVs into continuous RVs so classical density estimation techniques (that are suitable for continuous RVs only) can be employed [203,204]. Consider $\mathbf{x} = [\tilde{\mathbf{x}}, \check{\mathbf{x}}]^\mathrm{T}$ where $\tilde{\mathbf{x}} = [\max\{\bar{\mathbf{e}}\}, \psi(\bar{\mathbf{e}})]$ represents the continuous RVs; and $\check{\mathbf{x}} = [\mathsf{n}_\mathrm{p}, n_\mathrm{t}] + \boldsymbol{\gamma}$ represents the discrete RVs after adding the jitter $\boldsymbol{\gamma} \in \mathbb{R}^2$, i.e. a random vector representing a noise term. The new vector $\mathbf{x}$ of continuous RVs is such that

$$f_{\mathbf{y}, \mathsf{n}_\mathrm{t}}(\boldsymbol{y}, n_\mathrm{t}) = f_\mathbf{x}(\boldsymbol{x}) \tag{6.22}$$

holds $\forall \boldsymbol{\gamma}$, $f_{\boldsymbol{\gamma}}(\mathbf{0}) = 1$, $f_{\boldsymbol{\gamma}}(\boldsymbol{\gamma}) = 0 \; \forall \boldsymbol{\gamma} \in \{\mathbb{Z} \backslash \{0\}\}^2$.

A linear transformation, namely data sphering, is then applied to the jittered training

---

[2]Analogously to the measurement set $\mathbf{y}$, from now on the received signal vector $\mathbf{r}$ and the energy vector $\bar{\mathbf{e}}$ are associated to an unspecified SR.

data $\boldsymbol{x}_l$ so that the covariance matrix becomes the identity matrix [205]

$$\boldsymbol{z}_l = \boldsymbol{\Lambda}^{-\frac{1}{2}} \boldsymbol{A}^{\mathrm{T}} (\boldsymbol{x}_l - \bar{\boldsymbol{x}}) = [\tilde{\boldsymbol{z}}_l, \breve{\boldsymbol{z}}_l]^{\mathrm{T}} \tag{6.23}$$

where $\boldsymbol{\Lambda}$ is the diagonal matrix formed by the eigenvalues of the sample covariance matrix relative to $\{\boldsymbol{x}_l\}_{l \in \mathcal{N}_{\mathrm{T}}}$, $\boldsymbol{A}$ is the matrix formed by its corresponding eigenvectors, and $\bar{\boldsymbol{x}}$ is the sample mean vector from the training data.

The density estimation is carried out on the sphered training set $\{\boldsymbol{z}_l\}_{l \in \mathcal{N}_{\mathrm{T}}}$ and then the PDF in the original domain is obtained as $|\det(\boldsymbol{\Lambda}^{-\frac{1}{2}} \boldsymbol{A}^{\mathrm{T}})| f_{\mathsf{z}}(\boldsymbol{\Lambda}^{-\frac{1}{2}} \boldsymbol{A}^{\mathrm{T}}(\boldsymbol{x} - \bar{\boldsymbol{x}}))$. In particular, we consider two density estimation techniques based on the Fisher–Wald (FW) and the kernel density estimation (KDE) [54]. In the FW setting, the density function $f_{\mathsf{z}}(\boldsymbol{z})$ is approximated with a mixture of N_{GM} Gaussian distributions as

$$\widehat{f}(\boldsymbol{z}) = \sum_{i=1}^{N_{\mathrm{GM}}} \pi_i \varphi(\boldsymbol{z}; \boldsymbol{\mu}_i, \boldsymbol{\Sigma}_i) \tag{6.24}$$

where $\varphi(\cdot; \boldsymbol{\mu}_i, \boldsymbol{\Sigma}_i)$ is the Gaussian PDF; the weights π_i, the mean vectors $\boldsymbol{\mu}_i$, and the covariance matrices $\boldsymbol{\Sigma}_i$ are obtained through the minimization of the empirical risk in the FW setting [206]. The solution of the minimization problem is obtained via ML estimator or its approximation (e.g., the solution provided by the expectation-maximization algorithm).

In the KDE, the density function $f_{\mathsf{z}}(\boldsymbol{z})$ is approximated as

$$\widehat{f}(\boldsymbol{z}) = \frac{1}{N_{\mathrm{T}}} \sum_{l \in \mathcal{N}_{\mathrm{T}}} K(\tilde{\boldsymbol{z}} - \tilde{\boldsymbol{z}}_l; \tilde{\boldsymbol{H}}) K(\breve{\boldsymbol{z}} - \breve{\boldsymbol{z}}_l; \breve{\boldsymbol{H}}) \tag{6.25}$$

where $K(\tilde{\boldsymbol{z}}; \tilde{\boldsymbol{H}})$, $K(\breve{\boldsymbol{z}}; \breve{\boldsymbol{H}})$ are product kernels, parametrized by the matrices $\tilde{\boldsymbol{H}}$, $\breve{\boldsymbol{H}}$, called bandwidth matrices. We consider Gaussian kernels $K(\tilde{\boldsymbol{z}} - \tilde{\boldsymbol{z}}_l; \tilde{\boldsymbol{H}}) = \varphi(\tilde{\boldsymbol{z}}; \tilde{\boldsymbol{z}}_l, \tilde{\boldsymbol{H}})$, $K(\breve{\boldsymbol{z}} - \breve{\boldsymbol{z}}_l; \breve{\boldsymbol{H}}) = \varphi(\breve{\boldsymbol{z}}; \breve{\boldsymbol{z}}_l, \breve{\boldsymbol{H}})$. The bandwidth matrices are obtained through the normal reference rule [207].

6.4.2 Case Study

The proposed technique is validated via experimental results in terms of counting error outage (CEO) and counting RMSE. The CEO is defined as the probability that the counting error $|\widehat{n}_{\mathsf{t}} - \mathsf{n}_{\mathsf{t}}|$ is above a given target value $n^{\star}$

$$P_{\mathrm{ceo}}(n^{\star}) = \mathbb{P} \{ |\widehat{n}_{\mathsf{t}} - \mathsf{n}_{\mathsf{t}}| > n^{\star} \} \tag{6.26}$$

while the counting RMSE is defined as [3]

$$e_{\mathrm{rms}} = \sqrt{\mathbb{E}\left\{|\widehat{n}_{\mathrm{t}} - \mathsf{n}_{\mathrm{t}}|^2\right\}}. \tag{6.27}$$

The measurement campaign was carried out at the Department of Engineering, University of Ferrara (see Fig. 6.2). The size of the monitored area is 6×4 m^2 and the presence of a table, chairs, panels, walls, and other objects leads to a large number of potential scatterers (i.e., clutter and multipath). A network of $N_{\mathrm{R}} = 3$ SRs in monostatic configuration is emulated recording the measurements with a single SR in different locations. The measurements are then properly combined in the online stage. The SR is based on Novelda's UWB SR "X4M03" chip [208]. Tab. 6.4 summarizes the SR settings and the parameters values for the proposed technique. The number of targets (persons) n_{t} in the monitored area varies between 0 and $n_{\max} = 3$. For each value of $n_{\mathrm{t}} > 0$, $n_{\mathrm{c}} = 10$ possible spatial arrangements of the targets in the monitored area are considered (i.e., spatial configurations), with index set $\mathcal{N}_{\mathrm{c}} = \{1, 2, \ldots, n_{\mathrm{c}}\}$. Each configuration $\mathcal{P}_{n_{\mathrm{t}},j}$, with $j \in \mathcal{N}_{\mathrm{c}}$ corresponds to a different n_{t}-tuple of target positions, i.e. $\mathcal{P}_{n_{\mathrm{t}},j} = \{\boldsymbol{p}_{n,j}\}_{n\in\mathcal{N}_{\mathrm{t}}}$, where $\mathcal{N}_{\mathrm{t}} = \{1, 2, \ldots, n_{\mathrm{t}}\}$ is the index set relative to the targets, $\boldsymbol{p}_{n,j}$ is the position of the n-th target for the j-th configuration associated to n_{t}. For $n_{\mathrm{t}} = 0$, only $n_{\mathrm{c}} = 3$ configurations (i.e., measurements of the empty room at different time instants) are considered due to the absence of targets. Example configurations are depicted in Fig. 6.7. For each configuration $\mathcal{P}_{n_{\mathrm{t}},j}$, one thousand observation frames per SR are collected. After the clutter removal and energy detection, the number of energy vectors $\bar{\mathbf{e}}_i^{(j)}$ are 50 for each radar and each configuration (i.e., $j \in \{1, 2, \ldots, 50\}$).

The measurements are used as input of an iterative procedure to validate the proposed technique. At each run, the training (offline) and validation (online) phases are performed by picking a set of configurations $\mathcal{T}$ for training, and a set of configurations $\mathcal{V}$ for validating the generative model, following the leave-p-out cross-validation criteria [166].[4] This procedure ensures that the validation of the proposed technique is carried out on configurations relatively different from the ones used to learn the generative model.

Numerical results are provided for FW and KDE algorithms with ML estimation. The jitter $\boldsymbol{\gamma}$ is uniformly distributed over the interval $[-0.5, 0.5]^2$ in order to meet the constraints in (6.22). Results are compared with two multi-target detection algorithms,

---

[3]The CEO is approximated with the rate and the expectation in the RMSE is approximated with the sample mean due to the finite set of experimental data.

[4]In particular, $p = 4$ so the validation set $\mathcal{V}$ has cardinality $|\mathcal{V}| = 4$ and contains one configuration for each possible value of n_{t} at each iteration. The training set $\mathcal{T}$, with $|\mathcal{T}| = 29$, contains all the other configurations (i.e., $\mathcal{T} \cap \mathcal{V} = \emptyset$ with 27 configurations relative to the case $n_{\mathrm{t}} > 0$ and 2 relative to the case $n_{\mathrm{t}} = 0$).
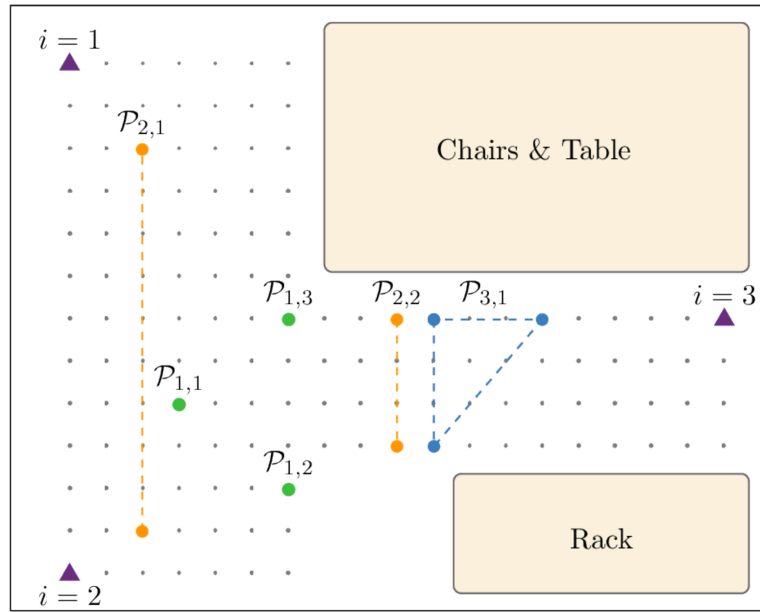
Figure 6.7: Map of the hall with the configurations $\mathcal{P}_{1,1}, \mathcal{P}_{1,2}, \mathcal{P}_{1,3}$ for $n_t = 1$, $\mathcal{P}_{2,1}, \mathcal{P}_{2,2}$ for $n_t = 2$, and $\mathcal{P}_{3,1}$ for $n_t = 3$. The violet triangles represent the SRs positions. The grid spacing is 0.3 m.
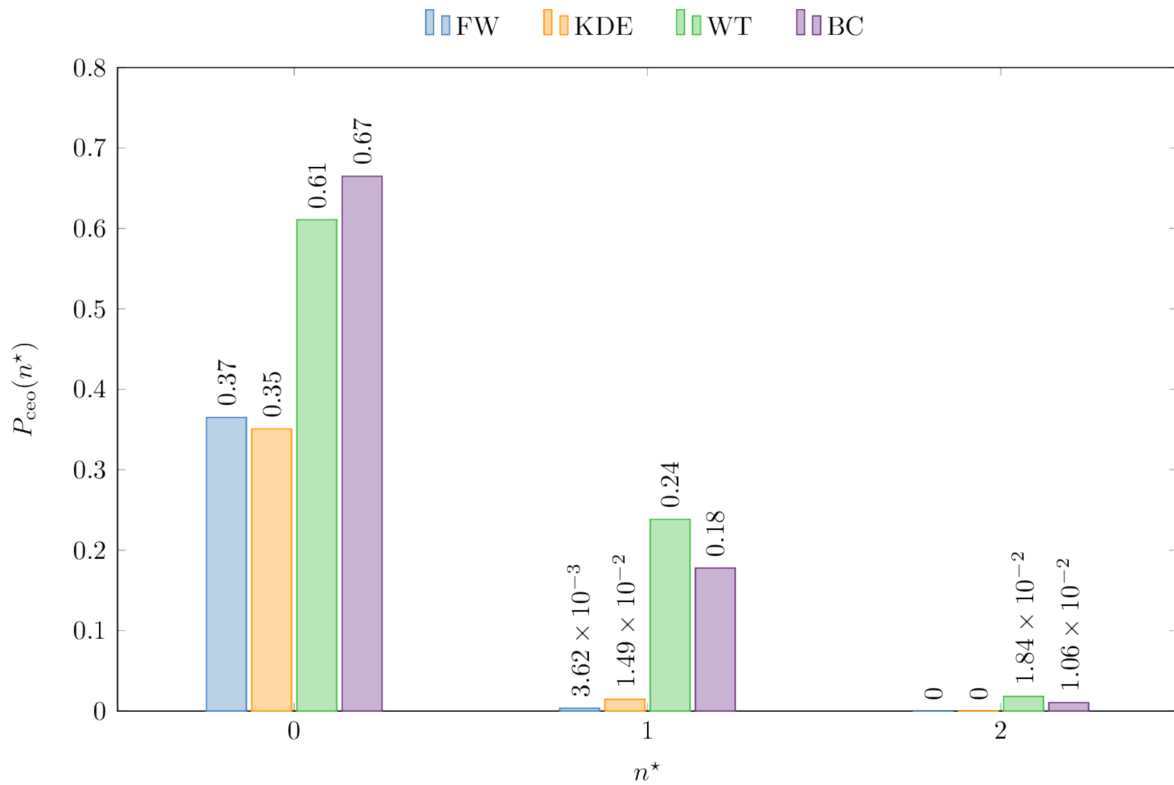

Figure 6.8: CEO as a function of the target counting error $n^\star$ for FW, KDE, window treshold (WT), and binary clustering (BC) algorithms.

namely window treshold (WT) [209] and BC [65], with CA-CFAR detection. The WT threshold value and the CA-CFAR window length are optimized such that the counting

73

Table 6.4: SR setting and signal processing parameters values.

Parameter (Symbol)	Value
SR carrier frequency	7.26 GHz
SR pulse bandwidth	1.4 GHz
SR energy per pulse	2.6 pJ
Repetition interval (T_{pr})	40 ms
Sample time (T_{s})	42.8 ps
Number of samples per frame (n_{s})	1079
Observation time (T_{obs})	43.4 ns
Window length EAF filter (N_{MA})	30
Dwell time (T_{d})	2 ns
Number of samples per energy bin (N_{d})	47
Length energy bin vector (N_{bin})	23
Number of energy bin vectors integrated (N_{int})	20
Number of principal components PCA (d)	9
Number of components in FW (N_{GM})	9

RMSE is minimized at each offline phase. The WT left and right guard lengths are 1 and 2 bins, respectively. The CA-CFAR guard length is 1 bin and the target false alarm probability is 0.01. The BC threshold distance is set to 0.45 m (approximatively one and an half of the distance associated to an energy bin). In the multi-target detection cases, each SR provides an estimate of the number of targets and the final estimate $\widehat{n}_{\mathrm{t}}$ is obtained as the mode of the estimates provided by each SR.

Fig. 6.8 shows the CEO as a function of the target counting error $n^{\star}$. It can be observed that the proposed algorithms outperform the multi-target detection algorithms. The error is zero in the 63% of the cases for both KDE and FW (the CEO is below 37% for $n^{\star} = 0$), whereas the error is zero only in the 39% of the cases for the WT (the CEO is below 61% for $n^{\star} = 0$) and 33% for the BC (the CEO is below 67% for $n^{\star} = 0$). This can be attributed to the fact that even though the clutter removal filter eliminates most of the contributes from static reflectors, the multipath generated after target backscattering remains unaltered at the filter output. This detrimental phenomena can be in part mitigated by the crowd-centric approach, while it severely affects the performance of multi-target detection algorithms. It can also be observed that the CEO is decreasing with $n^{\star}$ more rapidly for the proposed algorithms with respect to the multi-target detection ones. For example, the CEO goes from 0.35 with $n^{\star} = 0$ to 0.003 with $n^{\star} = 1$ for the FW, whereas it goes from 0.61 to 0.24 with $n^{\star} = 1$ for WT. Therefore, even in the presence of a counting error, its magnitude is smaller for the proposed algorithms.

Fig. 6.9 shows the CEO for FW and KDE as a function of the target counting error
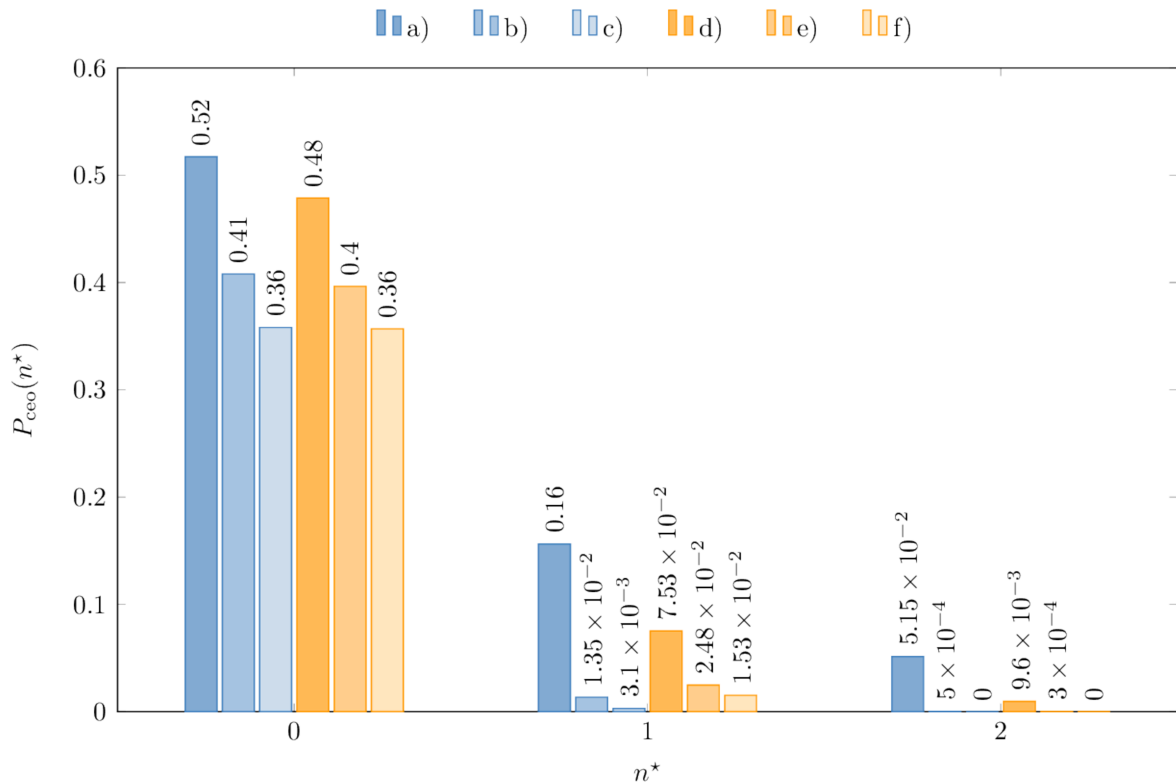
Figure 6.9: CEO as a function of $n^\star$ for FW and KDE algorithms: a) FW with $|\mathcal{T}| = 4$; b) FW with $|\mathcal{T}| = 17$; c) FW with $|\mathcal{T}| = 29$; d) KDE with $|\mathcal{T}| = 4$; e) KDE with $|\mathcal{T}| = 17$; and f) KDE with $|\mathcal{T}| = 29$.

$n^\star$ for different sizes of the set $\mathcal{T}$. The values are derived by averaging the performance over 200 randomly chosen validation sets $\mathcal{V}$ obtained from the iterative procedure. Given $\mathcal{V}$, the generative model is validated multiple times adding each time one configuration for each value of n_t to $\mathcal{T}$. It can be observed that the CEO decreases when the number of configurations available during the training phase increases. For $n^\star = 0$, the CEO decreases from about 51% to 35% for the FW and decreases from 47% to 35% for the KDE when the cardinality increases from $|\mathcal{T}| = 4$ to $|\mathcal{T}| = 29$. This represents an increase of about 12% for the probability of estimate the correct number of targets. Moreover, the decrement can be appreciated for all the values of $n^\star$. This can be attributed to the fact that we add to $\mathcal{T}$ one configuration for each value of n_t in each iteration, so the generative model is not biased toward any specif value of n_t.

Fig. 6.10 shows the counting RMSE as a function of the size of the training set $\mathcal{T}$ for FW and KDE algorithms. The values are obtained with the same procedure explained for Fig. 6.9. It can be observed that the performance improves when the number of configurations used in the training phase increases. Incrementing the cardinality, decreases the e_{rms} from 1.05 to 0.59 for the FW and from 0.83 to 0.62 for the KDE (the counting RMSE with $|\mathcal{T}| = 29$ is $e_{\mathrm{rms}} = 1.19$ for WT and $e_{\mathrm{rms}} = 1.13$ for BC). This can be
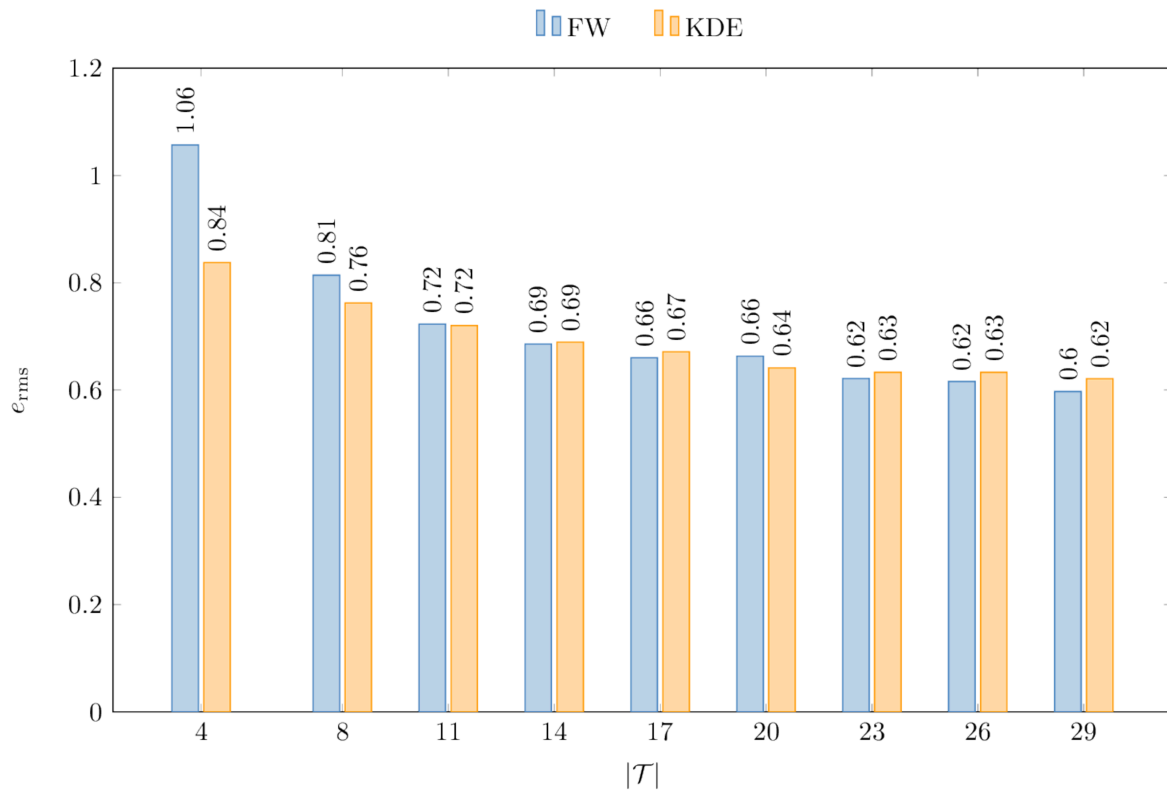
Figure 6.10: Counting RMSE as a function of $|\mathcal{T}|$ for FW and KDE algorithms.

attributed to the fact that the generative model becomes more accurate when the amount of data available during the learning process increases.

Chapter 7

Conclusion

This thesis presented the research activity on location awareness in 5th generation (5G) and beyond 5G (B5G) ecosystems, including the integration with sensor radar networks (SRNs). In particular, a soft information (SI)-based approach is developed for 5G networks considering both radio access technology (RAT)-dependent and RAT-independent measurements. A statistical characterization of clutter impairments based on experimental measurements is carried out for ultra-wideband (UWB) SRNs operating in indoor environments. Moreover, the design of algorithms for extracting physical analytics, i.e., number of person in a monitored area, based on the reflected signals in UWB SRNs is presented.

SI-based localization is developed for 5G networks without requiring any significant changes to the already standardized architecture and procedures. The proposed approach can be easily adapted to leverage any combination of measurements that will be available in B5G networks. Performance in terms of localization accuracy is evaluated for both SI-based and single-value estimate (SVE)-based approaches considering 5G downlink time-difference-of-arrival (DL-TDOA) measurements alone and the fusion of 5G DL-TDOA and WiFi time-of-flight (TOF) measurements. In particular, performance are evaluated via rigorous simulation of 5G reference signals, wireless environments, and procedures in full conformity with 3rd Generation Partnership Project (3GPP) standards. Results obtained in 3GPP standardized scenarios (i.e., urban microcell (UMi) and indoor open office (IOO) scenarios) show that SI-based approach significantly outperforms SVE-based approach.

The characterization of clutter impairments is presented for UWB SRNs operating in indoor environments. Based on experimental data, the statistical properties in terms of stationarity, correlation, and sample distribution of the are determined for static clutter. Such properties are evaluated using statistical tests and visual inspection of the

backscattered signals. It is shown that, the static clutter process can be considered as a non-stationary, correlated, Gaussian process.

The design of crowd-centric counting algorithm based on machine learning techniques, is also presented and validated via experimental data using a UWB SRN. In particular, based on a reduced representation of the received waveform samples, the number of target present in a monitored area is inferred without relaying on multi-target tracking and data association. Results show that the proposed crowd-centric approach significantly outperforms conventional algorithms.

This thesis (i) developed a machine learning approach for accurate localization in 5G and B5G networks and (ii) explored the integration of UWB SRNs for joint communication and sensing in B5G networks. The findings of this thesis show that techniques based on SI and integration of cellular networks and SRNs can effectively improve and enrich 5G and B5G ecosystems.

Bibliography

[1] M. Z. Win, A. Conti, S. Mazuelas, Y. Shen, W. M. Gifford, D. Dardari, and M. Chiani, "Network localization and navigation via cooperation," *IEEE Commun. Mag.*, vol. 49, no. 5, pp. 56–62, May 2011.

[2] M. Z. Win, Y. Shen, and W. Dai, "A theoretical foundation of network localization and navigation," *Proc. IEEE*, vol. 106, no. 7, pp. 1136–1165, Jul. 2018, special issue on *Foundations and Trends in Localization Technologies*.

[3] A. H. Sayed, A. Tarighat, and N. Khajehnouri, "Network-based wireless location: Challenges faced in developing techniques for accurate wireless location information," *IEEE Signal Process. Mag.*, vol. 22, no. 4, pp. 24–40, Jul. 2005.

[4] M. Z. Win, W. Dai, Y. Shen, G. Chrisikos, and H. V. Poor, "Network operation strategies for efficient localization and navigation," *Proc. IEEE*, vol. 106, no. 7, pp. 1224–1254, Jul. 2018, special issue on *Foundations and Trends in Localization Technologies*.

[5] A. Conti, F. Morselli, Z. Liu, S. Bartoletti, S. Mazuelas, W. C. Lindsey, and M. Z. Win, "Location awareness in beyond 5G networks," *IEEE Commun. Mag.*, vol. 59, no. 11, pp. 22–27, Nov. 2021.

[6] K. Witrisal, P. Meissner, E. Leitinger, Y. Shen, C. Gustafson, F. Tufvesson, K. Haneda, D. Dardari, A. F. Molisch, A. Conti, and M. Z. Win, "High-accuracy localization for assisted living," *IEEE Signal Process. Mag.*, vol. 33, no. 2, pp. 59–70, Mar. 2016.

[7] M. Z. Win, Z. Wang, Z. Liu, Y. Shen, and A. Conti, "Location awareness via intelligent surfaces: A path toward holographic NLN," *IEEE Trans. Veh. Technol.*, vol. 17, no. 2, pp. 37–45, Jun. 2022.

[8]   J. Thomas, J. Welde, G. Loianno, K. Daniilidis, and V. Kumar, "Autonomous flight for detection, localization, and tracking of moving targets with a small quadrotor," *IEEE Robot. Autom. Lett.*, vol. 2, no. 3, pp. 1762–1769, Jul. 2017.

[9]   D. Wu, D. Chatzigeorgiou, K. Youcef-Toumi, and R. Ben-Mansour, "Node localization in robotic sensor networks for pipeline inspection," *IEEE Trans. Ind. Informat.*, vol. 12, no. 2, pp. 809–819, Aug. 2016.

[10] R. Karlsson and F. Gustafsson, "The future of automotive localization algorithms: Available, reliable, and scalable localization: Anywhere and anytime," *IEEE Signal Process. Mag.*, vol. 34, no. 2, pp. 60–69, Mar. 2017.

[11] G. Zhan and W. Shi, "LOBOT: Low-cost, self-contained localization of small-sized ground robotic vehicles," *IEEE Trans. Parallel Distrib. Syst.*, vol. 24, no. 4, pp. 744–753, Apr. 2013.

[12] S. M. George *et al.*, "Distressnet: A wireless Ad Hoc and sensor network architecture for situation management in disaster response," *IEEE Commun. Mag.*, vol. 48, no. 3, pp. 128–136, Mar. 2010.

[13] X. Ying, S. Roy, and R. Poovendran, "Pricing mechanisms for crowd-sensed spatial-statistics-based radio mapping," *IEEE Trans. on Cogn. Commun. Netw.*, vol. 3, no. 2, pp. 242–254, Jun. 2017.

[14] R. K. Ganti, F. Ye, and H. Lei, "Mobile crowdsensing: Current state and future challenges," *IEEE Commun. Mag.*, vol. 49, no. 11, pp. 32–39, Nov. 2011.

[15] F. Zabini and A. Conti, "Inhomogeneous Poisson sampling of finite-energy signals with uncertainties in $\mathbb{R}^d$," *IEEE Trans. Signal Process.*, vol. 64, no. 18, pp. 4679–4694, Sep. 2016.

[16] G. Cardone, P. Bellavista, A. Corradi, C. Borcea, M. Talasila, and R. Curtmola, "Fostering participaction in smart cities: A geo-social crowdsensing platform," *IEEE Commun. Mag.*, vol. 51, no. 6, pp. 112–119, Jun. 2013.

[17] L. Evans, "Maps as deep: Reading the code of location-based social networks," *IEEE Technol. Soc. Mag.*, vol. 33, no. 1, pp. 73–80, Mar. 2014.

[18] A. Zanella, N. Bui, A. Castellani, L. Vangelista, and M. Zorzi, "Internet of things for smart cities," *IEEE Internet of Things J.*, vol. 1, no. 1, pp. 22–32, Feb. 2014.

[19] G. Pasolini, C. Buratti, L. Feltrin, F. Zabini, C. De Castro, R. Verdone, and O. Andrisano, "Smart city pilot projects using LoRa and IEEE 802.15.4 technologies," *MDPI Sensors*, vol. 18, no. 4, Apr. 2018.

[20] V. Moreno, M. A. Zamora, and A. F. Skarmeta, "A low-cost indoor localization system for energy sustainability in smart buildings," *IEEE Sensors J.*, vol. 16, no. 9, pp. 3246–3262, May 2016.

[21] S. D'oro, L. Galluccio, G. Morabito, and S. Palazzo, "Exploiting object group localization in the Internet of Things: Performance analysis," *IEEE Trans. Veh. Technol.*, vol. 64, no. 8, pp. 3645–3656, Aug. 2015.

[22] G. Pasolini, A. Guerra, F. Guidi, N. Decarli, and D. Dardari, "Crowd-based cognitive perception of the physical world: Towards the Internet of senses," *Sensors*, vol. 20, no. 9, p. 2437, 2020.

[23] H. Zaaraoui, Z. Altman, E. Altman, and T. Jimenez, "Forecast scheduling for mobile users," in *2016 IEEE 27th Annu Int. Symp. Personal, Indoor, and Mobile Radio Communications (PIMRC)*, 2016, pp. 1–6.

[24] H. Braham, S. B. Jemaa, G. Fort, E. Moulines, and B. Sayrac, "Fixed rank kriging for cellular coverage analysis," *IEEE Trans. Wireless Commun.*, vol. 66, no. 5, pp. 4212–4222, May 2017.

[25] ——, "Spatial prediction under location uncertainty in cellular networks," *IEEE Trans. Wireless Commun.*, vol. 15, no. 11, pp. 7633–7643, Nov. 2016.

[26] J. Lee, A. Conti, A. Rabbachin, and M. Z. Win, "Distributed network secrecy," *IEEE J. Sel. Areas Commun.*, vol. 31, no. 9, pp. 1889–1900, Sep. 2013.

[27] A. Rabbachin, A. Conti, and M. Z. Win, "Wireless network intrinsic secrecy," *IEEE/ACM Trans. Netw.*, vol. 23, no. 1, pp. 56–69, Feb. 2015.

[28] G. Chisci, H. ElSawy, A. Conti, M.-S. Alouini, and M. Z. Win, "Uncoordinated massive wireless networks: Spatiotemporal models and multiaccess strategies," *IEEE/ACM Trans. Netw.*, vol. 27, no. 3, pp. 918–931, Jun. 2019.

[29] T. Wang, Y. Shen, A. Conti, and M. Z. Win, "Network navigation with scheduling: Error evolution," *IEEE Trans. Inf. Theory*, vol. 63, no. 11, pp. 7509–7534, Nov. 2017.

[30] *Technical Specification Group Radio Access Network; Study on NR positioning support (Release 16)*, 3GPP™ Std. TR 38.855 V16.0.0 (2019-03), Mar. 2019, release 16.

[31] *Technical Specification Group Radio Access Network; Study on NR positioning enhancements (Release 17)*, 3rd Generation Partnership Project 3GPP™ TR 38.857 V17.0.0 (2021-03), Mar. 2021, release 17.

[32] *Technical Specification Group Services and System Aspects; Service requirements for the 5G system; Stage 1 (Release 18)*, 3rd Generation Partnership Project 3GPP™ TS 22.261 V18.2.0 (2021-03), Mar. 2021, release 18.

[33] S. Bartoletti, A. Conti, W. Dai, and M. Z. Win, "Threshold profiling for wideband ranging," *IEEE Signal Process. Lett.*, vol. 25, no. 6, pp. 873–877, Jun. 2018.

[34] S. Bartoletti, W. Dai, A. Conti, and M. Z. Win, "A mathematical model for wideband ranging," *IEEE J. Sel. Topics Signal Process.*, vol. 9, no. 2, pp. 216–228, Mar. 2015.

[35] S. Maranò, W. M. Gifford, H. Wymeersch, and M. Z. Win, "NLOS identification and mitigation for localization based on UWB experimental data," *IEEE J. Sel. Areas Commun.*, vol. 28, no. 7, pp. 1026–1035, Sep. 2010.

[36] S. Mazuelas, F. A. Lago, J. Blas, A. Bahillo, P. Fernandez, R. Lorenzo, and E. Abril, "Prior NLOS measurements correction for positioning in cellular wireless networks," *IEEE Trans. Vehicular Technology*, vol. 58, no. 5, pp. 2585–2591, Jun 2009.

[37] S. Bartoletti, A. Giorgetti, M. Z. Win, and A. Conti, "Blind selection of representative observations for sensor radar networks," *IEEE Trans. Veh. Technol.*, vol. 64, no. 4, pp. 1388–1400, Apr. 2015.

[38] S. Dwivedi and et al., "Positioning in 5G networks," *IEEE Commun. Mag.*, vol. 59, no. 11, pp. 38–44, 2021.

[39] K. W. Cheung, H.-C. So, W.-K. Ma, and Y.-T. Chan, "A constrained least squares approach to mobile positioning: Algorithms and optimality," *EURASIP J. Adv. in Signal Process.*, vol. 2006, pp. 1–23, 2006.

[40] C. Yang, Y. Huang, and X. Zhu, "Hybrid TDOA/AOA method for indoor positioning systems," in *The Institution of Engineering and Technology Seminar on Location Technologies*, 2007, pp. 1–5.

[41] A. Conti, D. Dardari, M. Guerra, L. Mucchi, and M. Z. Win, "Experimental characterization of diversity navigation," *IEEE Syst. J.*, vol. 8, no. 1, pp. 115–124, Mar. 2014.

[42] F. Morselli, S. Bartoletti, M. Z. Win, and A. Conti, "Localization in 5G ecosystem with Wi-Fi," in *2021 IEEE 22nd International Workshop on Signal Processing Advances in Wireless Communications (SPAWC)*, 2021, pp. 441–445.

[43] *Technical Specification Group Radio Access Network; LTE Positioning Protocol (LPP) (Release 16)*, 3rd Generation Partnership Project 3GPP™ TS 37.355 V16.6.0 (2021-09), Sep. 2021, release 16.

[44] *Technical Specification Group Radio Access Network; NG-RAN; NR Positioning Protocol A (NRPPa) (Release 16)*, 3rd Generation Partnership Project 3GPP™ TS 38.455 V16.6.0 (2021-10), Oct. 2021, release 16.

[45] T. Kleine-Ostmann and A. Bell, "A data fusion architecture for enhanced position estimation in wireless networks," *IEEE Commun. Lett.*, vol. 5, no. 8, pp. 343–345, Aug. 2001.

[46] M. McGuire, K. Plataniotis, and A. Venetsanopoulos, "Data fusion of power and time measurements for mobile terminal location," *IEEE Trans. Mobile Comput.*, vol. 4, no. 2, pp. 142–153, Mar. 2005.

[47] O. Kanhere and T. S. Rappaport, "Position location for futuristic cellular communications: 5G and beyond," *IEEE Commun. Mag.*, vol. 59, no. 1, pp. 70–75, Jan. 2021.

[48] R. Mahler, *Statistical Multisource-Multitarget Information Fusion.* Norwood, MA: Artech House, 2007.

[49] D. C. Mur, A. Gavras, M. Ghoraishi, H. Hrasnica, and A. Kaloxylos, "AI and ML – Enablers for beyond 5G networks," 5G PPP, White Paper, May 2021.

[50] G. A. W. Groups, "View on 5G architecture," 5G PPP, White Paper, Oct. 2021.

[51] *New SI: Study on Artificial Intelligence (AI)/Machine Learning (ML) for NR air interface*, Qualcomm Std. RP-213 560 (2021-12), Dec. 2021.

[52] F. Zafari, A. Gkelias, and K. K. Leung, "A survey of indoor localization systems and technologies," *IEEE Commun. Surveys Tuts.*, vol. 21, no. 3, pp. 2568–2599, Apr. 2019.

[53] S. Lopez-Tapia, R. Molina, and N. P. de la Blanca, "Deep CNNs for object detection using passive millimeter sensors," *IEEE Trans. Circuits Syst. Video Technol.*, vol. 29, no. 9, pp. 2580–2589, 2017.

[54] S. Mazuelas, A. Conti, J. C. Allen, and M. Z. Win, "Soft range information for network localization," *IEEE Trans. Signal Process.*, vol. 66, no. 12, pp. 3155–3168, Jun. 2018.

[55] A. Conti, S. Mazuelas, S. Bartoletti, W. C. Lindsey, and M. Z. Win, "Soft information for localization-of-things," *Proc. IEEE*, vol. 107, no. 11, pp. 2240–2264, Nov. 2019.

[56] G. Kwon, A. Conti, H. Park, and M. Z. Win, "Joint communication and localization in millimeter wave networks," *IEEE J. Sel. Topics Signal Process.*, vol. 15, no. 6, pp. 1439–1454, Nov. 2021.

[57] H. Tataria, M. Shafi, A. F. Molisch, M. Dohler, H. Sjöland, and F. Tufvesson, "6G wireless systems: Vision, requirements, challenges, insights, and opportunities," *Proc. IEEE*, vol. 109, no. 7, pp. 1166–1199, Jul. 2021.

[58] C. D'Andrea, S. Buzzi, and M. Lops, "Communications and radar coexistence in the massive MIMO regime: Uplink analysis," *IEEE Trans. Wireless Commun.*, vol. 19, no. 1, pp. 19–33, Jan. 2020.

[59] F. Liu, C. Masouros, A. P. Petropulu, H. Griffiths, and L. Hanzo, "Joint radar and communication design: Applications, state-of-the-art, and the road ahead," *IEEE Trans. Commun.*, vol. 68, no. 6, pp. 3834–3862, Feb. 2020.

[60] J. Qian, M. Lops, L. Zheng, X. Wang, and Z. He, "Joint system design for coexistence of MIMO radar and MIMO communication," *IEEE Trans. Signal Process.*, vol. 66, no. 13, pp. 3504–3519, Jul. 2018.

[61] B. Paul, A. R. Chiriyath, and D. W. Bliss, "Survey of RF communications and sensing convergence research," *IEEE Access*, vol. 5, pp. 252–270, 2017.

[62] E. Cianca, M. D. Sanctis, and S. D. Domenico, "Radios as Sensors," *IEEE Internet of Things J.*, vol. 4, no. 2, pp. 363–373, Apr. 2017.

[63] A. R. Chiriyath, B. Paul, and D. W. Bliss, "Radar-communications convergence: Coexistence, cooperation, and co-design," *IEEE Trans. on Cogn. Commun. Netw.*, vol. 3, no. 1, pp. 1–12, Mar. 2017.

[64] B. Li, A. P. Petropulu, and W. Trappe, "Optimum co-design for spectrum shar-ing between matrix completion based MIMO radars and a MIMO communication system," *IEEE Trans. Signal Process.*, vol. 64, no. 17, pp. 4562–4575, Sep. 2016.

[65] M. Chiani, A. Giorgetti, and E. Paolini, "Sensor radar for object tracking," *Proc. IEEE*, vol. 106, no. 6, pp. 1022–1041, Jun. 2018.

[66] A. Conti, M. Guerra, D. Dardari, N. Decarli, and M. Z. Win, "Network experimen-tation for cooperative localization," *IEEE J. Sel. Areas Commun.*, vol. 30, no. 2, pp. 467–475, Feb. 2012.

[67] N. Patwari, J. N. Ash, S. Kyperountas, A. O. Hero, R. L. Moses, and N. S. Correal, "Locating the nodes: Cooperative localization in wireless sensor networks," *IEEE Signal Process. Mag.*, vol. 22, no. 4, pp. 54–69, Jul. 2005.

[68] P. Withington, H. Fluhler, and S. Nag, "Enhancing homeland security with ad-vanced UWB sensors," pp. 51–58, Sep. 2003.

[69] F. Meyer, P. Braca, P. Willett, and F. Hlawatsch, "A scalable algorithm for tracking an unknown number of targets using multiple sensors," *IEEE Trans. Signal Process.*, vol. 65, no. 13, pp. 3478–3493, Jul. 2017.

[70] F. Meyer, T. Kropfreiter, J. L. Williams, R. A. Lau, F. Hlawatsch, P. Braca, and M. Z. Win, "Message passing algorithms for scalable multitarget tracking," *Proc. IEEE*, vol. 106, no. 2, pp. 221–259, Feb. 2018.

[71] S. M. Patole, M. Torlak, D. Wang, and M. Ali, "Automotive radars: A review of signal processing techniques," *IEEE Signal Process. Mag.*, vol. 34, no. 2, pp. 22–35, Mar. 2017.

[72] E. Paolini, A. Giorgetti, M. Chiani, R. Minutolo, and M. Montanari, "Localization capability of cooperative anti-intruder radar systems," *EURASIP J. Adv. Signal Processing*, vol. 2008, pp. 1–14, Apr. 2008.

[73] S. Bartoletti, A. Conti, and A. Giorgetti, "Analysis of UWB radar sensor networks," in *Proc. IEEE Int. Conf. Commun.*, Cape Town, South Africa, May 2010, pp. 1–6.

[74] S. Bartoletti, A. Conti, A. Giorgetti, and M. Z. Win, "Sensor radar networks for indoor tracking," *IEEE Wireless Commun. Lett.*, vol. 3, no. 2, pp. 157–160, Apr. 2014.

[75] J. Palacios, G. Bielsa, P. Casari, and J. Widmer, "Single- and multiple-Access point indoor localization for millimeter-Wave networks," *IEEE Trans. Wireless Commun.*, vol. 18, no. 3, pp. 1927–1942, Mar. 2019.

[76] S. Kianoush, S. Savazzi, F. Vicentini, V. Rampa, and M. Giussani, "Device-free RF human body fall detection and localization in industrial workplaces," *IEEE Internet of Things J.*, vol. 4, no. 2, pp. 351–362, Apr. 2017.

[77] P. Braca, P. Willett, K. LePage, S. Marano, and V. Matta, "Bayesian tracking in underwater wireless sensor networks with port-starboard ambiguity," *IEEE Trans. Signal Process.*, vol. 62, no. 7, pp. 1864–1878, Apr. 2014.

[78] Y. Ruan, P. Willett, A. Marrs, F. Palmieri, and S. Marano, "Practical fusion of quantized measurements via particle filtering," *IEEE Trans. Aerosp. Electron. Syst.*, vol. 44, no. 1, pp. 15–29, Jan. 2008.

[79] X. Quan, J. W. Choi, and S. H. Cho, "In-bound/out-bound detection of people's movements using an IR-UWB radar system," in *Int. Conf. on Electronics, Information and Communications (ICEIC)*, Kota Kinabalu, Malaysia, Jan. 2014, pp. 1–2.

[80] S. Bartoletti, A. Conti, and M. Z. Win, "Device-free counting via OFDM signals of opportunity," in *Proc. IEEE Workshop on Advances in Network Localization and Navigation (ANLN), Int. Conf. Commun.*, Kansas City, MO, May 2018, pp. 1–5.

[81] ——, "Towards counting via passive radar using OFDM waveforms," in *Proc. IEEE Workshop on Advances in Network Localization and Navigation (ANLN), Int. Conf. Commun.*, Paris, France, May 2017, pp. 803–808.

[82] K. W. Forsythe and D. W. Bliss, "MIMO radar waveform constraints for GMTI," *IEEE J. Sel. Topics Signal Process.*, vol. 4, no. 1, pp. 21–32, Feb. 2010.

[83] S. Bartoletti, N. Decarli, D. Dardari, M. Chiani, and A. Conti, "Order-of-arrival of tagged objects," *IEEE J. Radio Freq. Identif.*, vol. 2, no. 4, pp. 185 – 196, Nov. 2018.

[84] M. Franceschetti, S. Marano, and V. Matta, "Chernoff test for strong-or-weak radar models," *IEEE Trans. Signal Process.*, vol. 65, no. 2, pp. 289–302, Jan. 2017.

[85] G. Wang, S. Marano, J. Zhu, and Z. Xu, "Target localization by unlabeled range measurements," *IEEE Trans. Signal Process.*, vol. 68, pp. 6607–6620, 2020.

[86] M. Anisetti, C. A. Ardagna, V. Bellandi, E. Damiani, and S. Reale, "Map-based location and tracking in multipath outdoor mobile networks," *IEEE Trans. Wireless Commun.*, vol. 10, no. 3, pp. 814–824, 2011.

[87] J. Shen and A. F. Molisch, "Estimating multiple target locations in multi-path environments," *IEEE Trans. Wireless Commun.*, vol. 13, no. 8, pp. 4547–4559, Aug. 2014.

[88] S. Bartoletti, Z. Liu, M. Z. Win, and A. Conti, "Device-free localization of multiple targets in cluttered environments," *IEEE Trans. Aerosp. Electron. Syst.*, pp. 1–1, 2021, early access.

[89] M. Z. Win and R. A. Scholtz, "Impulse radio: How it works," *IEEE Commun. Lett.*, vol. 2, no. 2, pp. 36–38, Feb. 1998.

[90] ——, "On the robustness of ultra-wide bandwidth signals in dense multipath environments," *IEEE Commun. Lett.*, vol. 2, no. 2, pp. 51–53, Feb. 1998.

[91] ——, "On the energy capture of ultra-wide bandwidth signals in dense multipath environments," *IEEE Commun. Lett.*, vol. 2, no. 9, pp. 245–247, Sep. 1998.

[92] ——, "Ultra-wide bandwidth time-hopping spread-spectrum impulse radio for wireless multiple-access communications," *IEEE Trans. Commun.*, vol. 48, no. 4, pp. 679–691, Apr. 2000.

[93] M. Z. Win, "Spectral density of random UWB signals," *IEEE Commun. Lett.*, vol. 6, no. 12, pp. 526–528, Dec. 2002.

[94] M. Z. Win, D. Dardari, A. F. Molisch, W. Wiesbeck, and J. Zhang, "History and applications of UWB," *Proc. IEEE*, vol. 97, no. 2, pp. 198–204, Feb. 2009.

[95] S. Gezici, Z. Tian, G. B. Giannakis, H. Kobayashi, A. F. Molisch, H. V. Poor, and Z. Sahinoglu, "Localization via ultra-wideband radios: A look at positioning aspects for future sensor networks," *IEEE Signal Process. Mag.*, vol. 22, pp. 70–84, Jul. 2005.

[96] D. Dardari, A. Conti, U. J. Ferner, A. Giorgetti, and M. Z. Win, "Ranging with ultrawide bandwidth signals in multipath environments," *Proc. IEEE*, vol. 97, no. 2, pp. 404–426, Feb. 2009, special issue on *Ultra-Wide Bandwidth (UWB) Technology & Emerging Applications*.

[97] A. Giorgetti and M. Chiani, "Time-of-arrival estimation based on information theoretic criteria," *IEEE Trans. Signal Process.*, vol. 61, no. 8, pp. 1869–1879, Apr. 2013.

[98] B. Teague, Z. Liu, F. Meyer, A. Conti, and M. Z. Win, "Network localization and navigation with scalable inference and efficient operation," *IEEE Trans. Mobile Comput.*, vol. 21, no. 6, pp. 2072–2087, Jun. 2022.

[99] Q. Liang, "Radar sensor wireless channel modeling in foliage environment: UWB versus narrowband," *IEEE Sensors J.*, vol. 11, no. 6, pp. 1448–1457, Jun. 2011.

[100] M. Chiani, A. Giorgetti, M. Mazzotti, R. Minutolo, and E. Paolini, "Target detection metrics and tracking for UWB radar sensor networks," in *Proc. of the IEEE Int. Conf. on Ultra-Wideband (ICUWB)*, Vancouver, CANADA, Sep. 2009, pp. 469–474.

[101] M. I. Skolnik, *Radar Handbook*, 3rd ed.   New York, NY 10020: McGraw-Hill, 1970.

[102] G. Papa, P. Braca, S. Horn, S. Marano, V. Matta, and P. Willett, "Multisensor adaptive Bayesian tracking under time-varying target detection probability," *IEEE Trans. Aerosp. Electron. Syst.*, vol. 52, no. 5, pp. 2193–2209, Oct. 2016.

[103] A. Aubry, V. Carotenuto, A. De Maio, M. Rosamilia, and S. Marano, "Adaptive radar detection in the presence of missing-data," *IEEE Trans. Aerosp. Electron. Syst.*, pp. 1–1, 2022, early access.

[104] S. Bartoletti, A. Conti, and M. Z. Win, "Device-free counting via wideband signals," *IEEE J. Sel. Areas Commun.*, vol. 35, no. 5, pp. 1163–1174, Mar. 2017.

[105] F. Morselli, S. Bartoletti, S. Mazuelas, M. Z. Win, and A. Conti, "Crowd-centric counting via unsupervised learning," in *Proc. IEEE Workshop on Advances in Network Localization and Navigation (ANLN), Int. Conf. Commun.*, Shanghai, China, May 2019, pp. 1–6.

[106] J. W. Choi, J. H. Kim, and S. H. Cho, "A counting algorithm for multiple objects using an IR-UWB radar system," in *IEEE Int. Conf. on Net. Infrastr. and Digital Content*, Beijing, China, Sep. 2012, pp. 591–595.

[107] J. He and A. Arora, "A regression-based radar-mote system for people counting," in *2014 IEEE Int. Conf. on Pervasive Computing and Communications (PerCom)*, Louis Missouri, USA, Mar. 2014, pp. 95–102.

[108] S. Savazzi, S. Sigg, M. Nicoli, V. Rampa, S. Kianoush, and U. Spagnolini, "Device-free radio vision for assisted living: Leveraging wireless channel quality information for human sensing," *IEEE Signal Process. Mag.*, vol. 33, no. 2, pp. 45–58, Mar. 2016.

[109] ——, "Device-free radio vision for assisted living: Leveraging wireless channel quality information for human sensing," *IEEE Signal Process. Mag.*, vol. 33, no. 2, pp. 45–58, Mar. 2016.

[110] F. Guidi, N. Decarli, S. Bartoletti, A. Conti, and D. Dardari, "Detection of multiple tags based on impulsive backscattered signals," *IEEE Trans. Commun.*, vol. 62, no. 11, pp. 3918–3930, Nov. 2014.

[111] European Union's Horizon 2020 research and innovation programme, "LOCUS (LOCalization and analytics on-demand embedded in the 5G ecosystem, for Ubiquitous vertical applicationS) Project," https://www.locus-project.eu/.

[112] Z. Liu, W. Dai, and M. Z. Win, "Mercury: An infrastructure-free system for network localization and navigation," *IEEE Trans. Mobile Comput.*, vol. 17, no. 5, pp. 1119–1133, May 2018.

[113] L. Chettri and R. Bera, "A comprehensive survey on internet of things (IoT) toward 5G wireless systems," *IEEE Internet of Things J.*, vol. 7, no. 1, pp. 16–32, Jan. 2020.

[114] Y. Shen and M. Z. Win, "Fundamental limits of wideband localization – Part I: A general framework," *IEEE Trans. Inf. Theory*, vol. 56, no. 10, pp. 4956–4980, Oct. 2010.

[115] Y. Bar-Shalom, X. R. Li, and T. Kirubarajan, *Estimation with Applications to Tracking and Navigation: Algorithms and Software for Information Extraction.* Hoboken, NJ: John Wiley and Sons, 2001.

[116] S. Mazuelas, Y. Shen, and M. Z. Win, "Belief condensation filtering," *IEEE Trans. Signal Process.*, vol. 61, no. 18, pp. 4403–4415, Sep. 2013.

[117] A. Huizing, M. Heiligers, B. Dekker, J. de Wit, L. Cifola, and R. Harmanny, "Deep learning for classification of mini-UAVs using micro-Doppler spectrograms in cognitive radar," *IEEE Aerosp. Electron. Syst. Mag.*, vol. 34, no. 11, pp. 46–56, Nov. 2019.

[118] X. Li and K. Pahlavan, "Super-resolution TOA estimation with diversity for indoor geolocation," *IEEE Trans. Wireless Commun.*, vol. 3, no. 1, pp. 224–234, Jan. 2004.

[119] L. Stoica, A. Rabbachin, and I. Oppermann, "A low-complexity noncoherent IR-UWB transceiver architecture with TOA estimation," *IEEE Trans. Microw. Theory Techn.*, vol. 54, no. 4, pp. 1637–1646, Jun. 2006.

[120] L. Cong and W. Zhuang, "Hybrid TDOA/AOA mobile user location for wideband CDMA cellular systems," *IEEE Trans. Wireless Commun.*, vol. 1, no. 3, pp. 439–447, 2002.

[121] X. Li, "RSS-based location estimation with unknown pathloss model," *IEEE Trans. Wireless Commun.*, vol. 5, no. 12, pp. 3626–3633, Dec. 2006.

[122] C. Falsi, D. Dardari, L. Mucchi, and M. Z. Win, "Time of arrival estimation for UWB localizers in realistic environments," *EURASIP J. Appl. Signal Process.*, vol. 2006, pp. 1–13, Article ID 32 082, 2006, special issue on *Wireless Location Technologies and Applications*.

[123] H. Godrich, A. Petropulu, and H. Poor, "Sensor selection in distributed multiple-radar architectures for localization: A knapsack problem formulation," *IEEE Trans. Signal Process.*, vol. 60, no. 1, pp. 247–260, Jan. 2012.

[124] L. Kaplan, "Global node selection for localization in a distributed sensor network," *IEEE Trans. Aerosp. Electron. Syst.*, vol. 42, no. 1, pp. 113–135, Jan. 2006.

[125] ——, "Local node selection for localization in a distributed sensor network," *IEEE Trans. Aerosp. Electron. Syst.*, vol. 42, no. 1, pp. 136–146, Jan. 2006.

[126] S. Mazuelas, A. Bahillo, R. Lorenzo, P. Fernandez, F. A. Lago, E. Garcia, J. Blas, and E. Abril, "Robust indoor positioning provided by real-time RSSI values in unmodified WLAN networks," *IEEE J. Sel. Topics Signal Process.*, vol. 3, no. 5, pp. 821–831, Oct. 2009.

[127] I. Güvenç, C.-C. Chong, F. Watanabe, and H. Inamura, "NLOS identification and weighted least-squares localization for UWB systems using multipath channel statistics," *EURASIP J. Adv. in Signal Process.*, vol. 2008, pp. 1–14, Article ID 271 984, 2008.

[128] J. Khodjaev, Y. Park, and A. S. Malik, "Survey on NLOS identification and error mitigation problems in UWB-based positioning algorithms for dense environments," in *Annals of Telecommunications*, 2009.

[129] H. Wymeersch, S. Maranò, W. M. Gifford, and M. Z. Win, "A machine learning approach to ranging error mitigation for UWB localization," *IEEE Trans. Commun.*, vol. 60, no. 6, pp. 1719–1728, Jun. 2012.

[130] L. Mucchi and P. Marcocci, "A new parameter for UWB indoor channel profile identification," *IEEE Trans. Wireless Commun.*, vol. 8, no. 4, pp. 1597–1602, Apr. 2009.

[131] F. Montorsi, S. Mazuelas, G. M. Vitetta, and M. Z. Win, "On the performance limits of map-aware localization," *IEEE Trans. Inf. Theory*, vol. 59, no. 8, pp. 5023–5038, Aug. 2013.

[132] E. Foxlin, "Pedestrian tracking with shoe-mounted inertial sensors," *IEEE Comput. Graph. Appl.*, vol. 25, no. 6, pp. 38–46, Nov.-Dec. 2005.

[133] J. Prieto, S. Mazuelas, and M. Z. Win, "Context-aided inertial navigation via belief condensation," *IEEE Trans. Signal Process.*, vol. 64, no. 12, pp. 3250–3261, Jun. 2016.

[134] C. M. Bishop, *Pattern Recognition and Machine Learning.*   New York: Springer-Verlag, 2006.

[135] D. MacKay, *Information Theory, Inference and Learning Algorithms.*   Cambridge University Press, 2003.

[136] J. Thomas, J. Welde, G. Loianno, K. Daniilidis, and V. Kumar, "Autonomous flight for detection, localization, and tracking of moving targets with a small quadrotor," *IEEE Robot. Autom. Lett.*, vol. 2, no. 3, pp. 1762–1769, Jul. 2017.

[137] S. Bartoletti, A. Conti, and M. Z. Win, "Device-free counting via wideband signals," *IEEE J. Sel. Areas Commun.*, vol. 35, no. 5, pp. 1163–1174, May 2017.

[138] R. Estrada, R. Mizouni, H. Otrok, A. Ouali, and J. Bentahar, "A crowd-sensing framework for allocation of time-constrained and location-based tasks," *IEEE Trans. Serv. Comput.*, vol. 13, no. 5, pp. 769–785, 2020.

[139] K. Lin, M. Chen, J. Deng, M. M. Hassan, and G. Fortino, "Enhanced fingerprinting and trajectory prediction for IoT localization in smart buildings," vol. 13, no. 3, pp. 1294–1307, Jul. 2016.

[140] G. Cardone, L. Foschini, P. Bellavista, A. Corradi, C. Borcea, M. Talasila, and R. Curtmola, "Fostering participaction in smart cities: a geo-social crowdsensing platform," *IEEE Commun. Mag.*, vol. 51, no. 6, pp. 112–119, Jun. 2013.

[141] D. Zhang, S. Zhao, L. T. Yang, M. Chen, Y. Wang, and H. Liu, "NextMe: Localization using cellular traces in Internet of Things," *IEEE Trans. Ind. Informat.*, vol. 11, no. 2, pp. 302–312, Apr. 2015.

[142] S. G. Nagarajan, P. Zhang, and I. Nevat, "Geo-spatial location estimation for Internet of Things (IoT) networks with one-way time-of-arrival via stochastic censoring," *IEEE Internet of Things J.*, vol. 4, no. 1, pp. 205–214, Feb. 2017.

[143] S. D'oro, L. Galluccio, G. Morabito, and S. Palazzo, "Exploiting object group localization in the Internet of Things: Performance analysis," *IEEE Trans. Veh. Technol.*, vol. 64, no. 8, pp. 3645–3656, Aug. 2015.

[144] *Evolved Universal Terrestrial Radio Access (E-UTRA); Study on minimization of drive-tests in next generation networks*, 3rd Generation Partnership Project 3GPP™ TR 36.805 V9.0.0 (2010-01), Jan. 2010, release 9.

[145] L. Chiaraviglio, S. Rossetti, S. Saida, S. Bartoletti, and N. Blefari-Melazzi, "Pencil beamforming increases human exposure to electromagnetic fields: True or false?" *IEEE Access*, vol. 9, pp. 25 158–25 171, 2021.

[146] *Technical Specification Group Radio Access Network; NR; Physical channels and modulation (Release 16)*, 3GPP™ Std. TS 38.211 V16.6.0 (2021-06), Jun. 2021, release 16.

[147] *Evolved Universal Terrestrial Radio Access (E-UTRA); Physical channels and modulation*, 3rd Generation Partnership Project 3GPP™ TS 36.211 V9.0.0 (2009-12), Dec. 2009, release 9.

[148] *Technical Specification Group Radio Access Network; NR; Physical layer procedures for data (Release 16)*, 3rd Generation Partnership Project 3GPP™ TS 38.214 V16.0.0 (2020-10), Oct. 2020, release 16.

[149] S. Bartoletti, W. Dai, A. Conti, and M. Win, "Threshold profiling for wideband ranging," *IEEE Signal Process. Lett.*, vol. 25, no. 6, pp. 873–877, Jun. 2018.

[150] H. Ryden, A. A. Zaidi, S. M. Razavi, F. Gunnarsson, and I. Siomina, "Enhanced time of arrival estimation and quantization for positioning in LTE networks," in *2016 IEEE 27th An. Int. Symp. Personal, Indoor, and Mobile Radio Communications (PIMRC)*, 2016, pp. 1–6.

[151] *3rd Generation Partnership Project; Technical Specification Group Radio Access Network; Evolved Universal Terrestrial Radio Access (E-UTRA); Requirements for support of radio resource management (Release 16)*, 3GPP™ Std. TS 36.133 V16.7.0 (2020-10), Oct. 2020, release 16.

[152] C. Mensing and S. Plass, "Positioning algorithms for cellular networks using TDOA," in *2006 IEEE Int. Conf. Acoust. Speech and Signal Process. Proc.*, vol. 4, 2006, pp. IV–IV.

[153] P. Yuan, T. Zhang, N. Yang, H. Xu, and Q. Zhang, "Energy efficient network localisation using hybrid TOA/AOA measurements," *IET Communications*, vol. 13, no. 8, pp. 963–971, 2019.

[154] F. Guidi and D. Dardari, "Radio positioning with EM processing of the spherical wavefront," *IEEE Trans. Wireless Commun.*, vol. 20, no. 6, pp. 3571–3586, Jun. 2021.

[155] I. F. Akyildiz, J. M. Jornet, and C. Han, "Terahertz band: Next frontier for wireless communications," *Phys. Commun.*, vol. 12, pp. 16–32, 2014.

[156] E. Mazor, A. Averbuch, Y. Bar-Shalom, and J. Dayan, "Interacting multiple model methods in target tracking: A survey," *IEEE Trans. Aerosp. Electron. Syst.*, vol. 34, no. 1, pp. 103–123, Jan. 1998.

[157] A. T. Ihler, J. W. Fisher III, R. L. Moses, and A. S. Willsky, "Nonparametric belief propagation for self-localization of sensor networks," *IEEE J. Sel. Areas Commun.*, vol. 23, no. 4, pp. 809–819, Apr. 2005.

[158] *Technical Specification Group Radio Access Network; Study on channel model for frequencies from 0.5 to 100 GHz (Release 16)*, 3rd Generation Partnership Project 3GPP™ TR 38.901 V16.1.0 (2020-01), Jan. 2020, release 16.

[159] S. Jaeckel, L. Raschkowski, K. Börner, and L. Thiele, "QuaDRiGa: A 3-D multi-cell channel model with time evolution for enabling virtual field trials," *IEEE Trans. Antennas Propag.*, vol. 62, no. 6, pp. 3242–3256, Jun. 2014.

[160] S. Jaeckel, L. Raschkowski, K. Börner, L. Thiele, F. Burkhardt, and E. Eberlein, "QuaDRiGa - quasi deterministic radio channel generator, user manual and documentation," Fraunhofer Heinrich Hertz Institute, Technical Report, 2017.

[161] *Technical Specification Group Radio Access Network; NR; Base Station (BS) radio transmission and reception (Release 17)*, 3rd Generation Partnership Project 3GPP™ TS 38.104 V17.3.0 (2021-09), Sep. 2021, release 17.

[162] *Technical Specification Group Radio Access Network; Study on new radio access technology Physical layer aspects (Release 16)*, 3rd Generation Partnership Project 3GPP™ TR 38.802 V14.2.0 (2017-09), Mar. 2017, release 14.

[163] *Technical Specification Group Radio Access Network; NR; Physical layer measurements (Release 16)*, 3GPP™ Std. TS 38.215 V16.4.0 (2020-10), Jan. 2021, release 16.

[164] *System Level Performance Evaluation for RAT-Dependent Positioning Techniques*, Ericsson Std. R1-1 903 142 (2019-02), Feb. 2019.

[165] M. Rea, A. Fakhreddine, D. Giustiniano, and V. Lenders, "Filtering noisy 802.11 time-of-flight ranging measurements from commoditized WiFi radios," *IEEE/ACM Transactions on Networking*, vol. 25, no. 4, pp. 2514–2527, Aug. 2017.

[166] S. Arlot and A. Celisse, "A survey of cross-validation procedures for model selection," *Statistics Surveys*, vol. 4, pp. 40–79, 2010.

[167] R. S. Thoma *et al.*, "Cooperative passive coherent location: A promising 5G service to support road safety," *IEEE Commun. Mag.*, vol. 57, no. 9, pp. 86–92, Sep. 2019.

[168] S. Denis, R. Berkvens, and M. Weyn, "A survey on detection, tracking and identification in radio frequency-based device-free localization," *Sensors*, vol. 19, no. 23, p. 5329, Dec. 2019.

[169] L. Zheng, M. Lops, Y. C. Eldar, and X. Wang, "Radar and communication coexistence: An overview: A review of recent methods," *IEEE Signal Process. Mag.*, vol. 36, no. 5, pp. 85–99, Sep. 2019.

[170] C. B. Barneto, T. Riihonen, M. Turunen, L. Anttila, M. Fleischer, K. Stadius, J. Ryynänen, and M. Valkama, "Full-duplex OFDM radar with LTE and 5G NR waveforms: Challenges, solutions, and measurements," *IEEE Trans. Microw. Theory Techn.*, vol. 67, no. 10, pp. 4042–4054, Oct. 2019.

[171] H. Godrich, A. P. Petropulu, and H. V. Poor, "Power allocation strategies for target localization in distributed multiple-radar architectures," *IEEE Trans. Signal Process.*, vol. 59, no. 7, pp. 3226–3240, Jul. 2011.

[172] C. A. Gómez-Vega, F. Morselli, M. Z. Win, and A. Conti, "A statistical range information model with application to UWB localization," in *MILCOM 2021 - 2021 IEEE Military Communications Conference (MILCOM)*, 2021, pp. 538–543.

[173] A. Farina, B. Ristic, and L. Timmoneri, "Cramér-Rao bound for nonlinear filtering with $p_d < 1$ and its application to target tracking," *IEEE Trans. Signal Process.*, vol. 50, no. 8, pp. 1916–1924, Aug. 2002.

[174] N. Decarli, A. Guerra, A. Conti, R. D'Errico, A. Sibille, and D. Dardari, "Non-regenerative relaying for network localization," *IEEE Trans. Wireless Commun.*, vol. 13, no. 1, pp. 174–185, Jan. 2014.

[175] D. Dardari, A. Conti, J. Lien, and M. Z. Win, "The effect of cooperation on localization systems using UWB experimental data," *EURASIP J. Appl. Signal Process.*, vol. 2008, pp. 1–11, Article ID 513 873, 2008, special issue on *Cooperative Localization in Wireless Ad Hoc and Sensor Networks*.

[176] B. Yazici and G. Xie, "Wideband extended range-Doppler imaging and waveform design in the presence of clutter and noise," *IEEE Trans. Inf. Theory*, vol. 52, no. 10, pp. 4563–4580, Oct. 2006.

[177] H. L. V. Trees, *Detection, Estimation, and Modulation Theory*, 1st ed. New York, NY 10158-0012: John Wiley & Sons, Inc., 1968.

[178] A. Lazaro, D. Girbau, and R. Villarino, "Techniques for clutter suppression in the presence of body movements during the detection of respiratory activity through UWB radars," *Sensors*, vol. 14, no. 2, pp. 2595–2618, Feb. 2014.

[179] J. Salmi and A. F. Molisch, "Propagation parameter estimation, modeling and measurements for ultrawideband MIMO radar," *IEEE Trans. Antennas Propag.*, vol. 59, no. 11, pp. 4257–4267, Nov. 2011.

[180] R. Niu, R. S. Blum, P. K. Varshney, and A. L. Drozd, "Target localization and tracking in noncoherent multiple-input multiple-output radar systems," *IEEE Trans. Aerosp. Electron. Syst.*, vol. 48, no. 2, pp. 1466–1489, Apr. 2012.

[181] F. Morselli, S. Bartoletti, S. Mazuelas, M. Z. Win, and A. Conti, "Crowd-centric counting via unsupervised learning," in *2019 IEEE Int. Conf. on Communications Workshops (ICC Workshops)*. IEEE, May 2019.

[182] E. Conte and A. D. Maio, "Mitigation techniques for non-Gaussian sea clutter," *IEEE J. Ocean. Eng.*, vol. 29, no. 2, pp. 284–302, Apr. 2004.

[183] A. Balleri, A. Nehorai, and J. Wang, "Maximum likelihood estimation for compound-Gaussian clutter with inverse gamma texture," *IEEE Trans. Aerosp. Electron. Syst.*, vol. 43, no. 2, pp. 775–779, Apr. 2007.

[184] F. Meyer *et al.*, "Message passing algorithms for scalable multitarget tracking," *Proc. IEEE*, vol. 106, no. 2, pp. 221–259, Feb. 2018.

[185] V. Anastassopoulos, G. Lampropoulos, A. Drosopoulos, and N. Rey, "High resolution radar clutter statistics," *IEEE Trans. Aerosp. Electron. Syst.*, vol. 35, no. 1, pp. 43–60, Jan. 1999.

[186] S. Haykin, R. Bakker, and B. Currie, "Uncovering nonlinear dynamics-the case study of sea clutter," *Proc. IEEE*, vol. 90, no. 5, pp. 860–881, May 2002.

[187] M. Greco, F. Bordoni, and F. Gini, "X-band sea-clutter nonstationarity: Influence of long waves," *IEEE J. Ocean. Eng.*, vol. 29, no. 2, pp. 269–283, Apr. 2004.

[188] F. Gini and A. Farina, "Vector subspace detection in compound-Gaussian clutter. Part I: Survey and new results," *IEEE Trans. Aerosp. Electron. Syst.*, vol. 38, no. 4, pp. 1295–1311, Oct. 2002.

[189] F. Gini, A. Farina, and M. Montanari, "Vector subspace detection in compound-Gaussian clutter. Part II: Performance analysis," *IEEE Trans. Aerosp. Electron. Syst.*, vol. 38, no. 4, pp. 1312–1323, Oct. 2002.

[190] R. B. D'Agostino and M. A. Stephens, *Goodness-of-Fit-Techniques.* Taylor & Francis Inc, 1986.

[191] G. Cardone, L. Foschini, P. Bellavista, A. Corradi, C. Borcea, M. Talasila, and R. Curtmola, "Fostering participaction in smart cities: a geo-social crowdsensing platform," *IEEE Commun. Mag.*, vol. 51, no. 6, pp. 112–119, Jun. 2013.

[192] S. M. George, W. Zhou, H. Chenji, M. Won, Y. O. Lee, A. Pazarloglou, R. Stoleru, and P. Barooah, "Distressnet: A wireless Ad Hoc and sensor network architecture for situation management in disaster response," *IEEE Commun. Mag.*, vol. 48, no. 3, pp. 128–136, Mar. 2010.

[193] N. C. Tang, Y. Y. Lin, M. F. Weng, and H. Y. M. Liao, "Cross-camera knowledge transfer for multiview people counting," *IEEE Trans. Image Process.*, vol. 24, no. 1, pp. 80–93, Jan 2015.

[194] B. K. Dan, Y. S. Kim, Suryanto, J. Y. Jung, and S. J. Ko, "Robust people counting system based on sensor fusion," *IEEE Trans. Consum. Electron.*, vol. 58, no. 3, pp. 1013–1021, August 2012.

[195] A. B. Chan and N. Vasconcelos, "Counting people with low-level features and Bayesian regression," *IEEE Trans. Image Process.*, vol. 21, no. 4, pp. 2160–2177, April 2012.

[196] H. Li, E. C. L. Chan, X. Guo, J. Xiao, K. Wu, and L. M. Ni, "Wi-counter: Smartphone-based people counter using crowdsourced Wi-Fi signal data," *IEEE Trans. Human-Mach. Syst.*, vol. 45, no. 4, pp. 442–452, Aug 2015.

[197] S. Depatla, A. Muralidharan, and Y. Mostofi, "Occupancy estimation using only WiFi power measurements," *IEEE J. Sel. Areas Commun.*, vol. 33, no. 7, pp. 1381–1393, July 2015.

[198] K. K. Mada, H.-C. Wu, and S. S. Iyengar, "Efficient and robust EM algorithm for multiple wideband source localization," *IEEE Trans. Veh. Technol.*, vol. 58, no. 6, pp. 3071–3075, Jul. 2009.

[199] L. Lu, H. Zhang, and H.-C. Wu, "Novel energy-based localization technique for multiple sources," *IEEE Syst. J.*, vol. 8, no. 1, pp. 142–150, Mar. 2014.

[200] M. Z. Win, F. Meyer, Z. Liu, W. Dai, S. Bartoletti, and A. Conti, "Efficient multi-sensor localization for the Internet of Things," *IEEE Signal Process. Mag.*, vol. 35, no. 5, pp. 153–167, Sep. 2018.

[201] R. Niu and P. K. Varshney, "Target location estimation in sensor networks with quantized data," *IEEE Trans. Signal Process.*, vol. 54, no. 12, pp. 4519–4528, Dec. 2006.

[202] I. Jolliffe, *Principal Component Analysis.*   John Wiley & Sons, 2005.

[203] T. Nagler, "A generic approach to nonparametric function estimation with mixed data," *Statistics and Prob. Lett.*, vol. 137, no. C, pp. 326–330, Apr. 2017.

[204] ——, "Asymptotic analysis of the jittering kernel density estimator," *Mathem. Meth. of Statistics*, vol. 27, no. 1, pp. 32–46, Jan. 2018.

[205] J. Klemelä, *Smoothing of Multivariate Data: Density Estimation and Visualization.* John Wiley & Sons, 2009.

[206] V. Vapnik, *Statistical learning theory.* Wiley, New York, 1998, vol. 3.

[207] D. W. Scott, *Multivariate Density Estimation: Theory, Practice, and Visualization.* John Wiley & Sons, 2015.

[208] Novelda, "X4 datasheet," https://www.xethru.com/community/resources/x4-datasheet.106/, [Online].

[209] J. W. Choi, S. S. Nam, and S. H. Cho, "Multi-human detection algorithm based on an impulse radio ultra-wideband radar system," *IEEE Access*, vol. 4, pp. 10 300–10 309, 2016.

Author's Publication List

Journal Papers

(J1) F. Morselli, S. Modarres Razavi, M. Z. Win, and A. Conti, "Soft information based localization for 5G networks and beyond," submitted to *IEEE Trans. Wireless Commun.*, 2022.

(J2) A. Conti, F. Morselli, Z. Liu, S. Bartoletti, S. Mazuelas, W. C. Lindsey, and M. Z. Win, "Location awareness in beyond 5G networks," *IEEE Commun. Mag.*, vol. 59, no. 11, pp. 22-27, Nov. 2021.

Conference Proceedings

(C1) C. A. Gòmez-Vega, F. Morselli, M. Z. Win, and A. Conti, "A statistical range information model with application to UWB localization," in *Proc. MILCOM 2021-2021 IEEE Military Communications Conference (MILCOM)*, 2021, pp. 538-543.

(C2) F. Morselli, S. Bartoletti, M. Z. Win, and A. Conti, "Localization in 5G ecosystem with Wi-Fi," in *Proc. 2021 IEEE 22nd International Workshop on Signal Processing Advances in Wireless Communications (SPAWC)*, 2021, , pp. 441-445.

(C3) N. Blefari-Melazzi, S. Bartoletti, L. Chiaraviglio, F. Morselli, E. Baena, G. Bernini, D. Giustiniano, M. Hunukumbure, G. Solmaz, and K. Tsagkaris, "LOCUS: Localization and analytics on-demand embedded in the 5G ecosystem," in *Proc. 2020 European Conference on Networks and Communications (EuCNC)*, 2020, pp. 170-175.

(C4) F. Morselli, S. Bartoletti, and A. Conti, "Indoor residual clutter characterization for UWB sensor radar networks," in *Proc. IEEE Workshop on Advances in Network Localization and Navigation (ANLN), Int. Conf. Commun. (ICC)*, 2020, pp. 1-6.

(C5) F. Morselli, S. Bartoletti, S. Mazuelas, M. Z. Win, and A. Conti, "Crowd-centric counting via unsupervised learning," in *Proc. IEEE Workshop on Advances in*

Network Localization and Navigation (ANLN), Int. Conf. Commun. (ICC), 2019, pp. 1-6.

(C6) F. Morselli, F. Zabini, and A. Conti, "Environmental monitoring via vehicular crowdsensing," in *Proc. IEEE 29th Annu. Int. Symp. Personal, Indoor, and Mobile Radio Communications (PIMRC),* 2018, pp. 1382-1387.

Abstracts

(A1) A. Giani, P. Borges de Souza, S. Bartoletti, F. Morselli, A. Conti, M. C. Zatelli, "Clustering techniques for thyroid nodules malignancy inference in the era of personalized medicine," *Endocrine Abstracts,* 2020.

Coauthored Book Chapters

(B1) D. Dardari, M. Nicoli, M. Brambilla, F. Guidi, A. Guerra, F. Morselli, and A. Conti, "6G Technologies for Localization, " in CNIT Technical Reports-09: 6G Wireless Systems: Enabling Technologies, 2022, to appear.

Coauthored White Papers

(W1) 5G Infrastructure Public Private Partnership (5G PPP), "AI and ML – Enablers for Beyond 5G Networks," Version 1.0, 2021.

Coauthored Project Deliverables

(D1) LOCUS, "Implementation of the Virtualization Platform for Network Control and Management: final version," D4.4, 2022.

(D2) LOCUS, "5G Based Localization Solutions, Final Version," D3.7, 2022.

(D3) LOCUS, "Integration with Device-Free Localization," intermediate version, D3.8, 2022.

(D4) LOCUS, "Network management, network-assisted self-driving vehicles, people mobility and flow monitoring applications, integrated with geolocation mechanisms," D6.2, 2022.

(D5) LOCUS, ""Design and implementation of virtualization technologies and pattern recognition mechanisms for physical analytics," final version, D5.2, 2022.

(D6) LOCUS, "Detailed requirements from scenarios and application specification," D6.1, 2021.

(D7) LOCUS, "Integration with Device-Free Localization," intermediate version, D3.6, 2021.

(D8) LOCUS, "Integrated localization technologies: final version," D3.4, 2021.

(D9) LOCUS, "5G Based Advanced Localization Solutions ," D3.2, 2021.

(D10) LOCUS, "Integration with Device-Free Localization," D3.5, 2020.

(D11) LOCUS, "Integrated localization technologies: preliminary version," D3.3, 2020.

(D12) LOCUS, "5G Based Preliminary Localization Solutions," D3.1, 2020.

Coauthored Project Reports

(R1) nCOT, "Final Technical Report," 2021.

(R2) nCOT, "Research Performance Progress Report: third year report," 2020.

(R3) nCOT, "Research Performance Progress Report: second year report," 2019.

(R4) nCOT, "Research Performance Progress Report: first year report," 2018.